AN ENHANCED CENTROIDING APPROACH FOR ACCURATE STAR DETECTION UNDER LUNAR SURFACE NOISE CONDITIONS

BY

ANIS HANNANI BINTI RAZAMAN

INTERNATIONAL ISLAMIC UNIVERSITY MALAYSIA

2026

AN ENHANCED CENTROIDING APPROACH FOR ACCURATE STAR DETECTION UNDER LUNAR SURFACE NOISE CONDITIONS

BY

ANIS HANNANI BINTI RAZAMAN

A dissertation submitted in fulfilment of the requirement for the degree of Master of Science in Engineering

Kulliyyah of Engineering
International Islamic University Malaysia

JUNE 2026

ABSTRACT

Star sensors play a crucial role in space navigation, providing reliable attitude determination for spacecraft, which is especially important for future lunar missions such as the International Lunar Research Station (ILRS). Operating on the lunar surface, however, introduces unique challenges. Strong solar reflections from the lunar regolith, together with cosmic and solar radiation generate significant noise that can degrade image quality and disrupt the star detection as well as reducing the centroiding accuracy. This research aims to develop an enhanced centroiding algorithm to overcome the noises in the lunar environment as well as to evaluate the performance of the proposed algorithm. The methodology incorporates several preprocessing stages, including Point Spread Function (PSF) modelling to simulate optical blurring and median filtering for noise suppression. Star regions are then segmented using the global thresholding method, where the threshold value is defined as a function of the maximum image intensity. The centroid of each detected star is computed using an intensity-weighted Centre of Mass (COM) approach. The accuracy of the proposed method is validated by transforming pixel-based centroid coordinates into celestial coordinates through an affine transformation, followed by star identification using the Hipparcos star catalogue. Experimental evaluation was conducted to imitate the lunar surface environment under simulated noise including Poisson-Gaussian noise, salt-and-pepper noise, speckle noise, and sunlight glare. The results show that the proposed algorithm outperforms conventional methods such as COM, Gaussian Fitting, and Sieve Search Algorithm (SSA), achieving the lowest average RMSE of 1.218 pixels and Euclidean distance of 1.143 pixels. It also maintains a low False Detection Rate (FDR) of 6.716% and angular distance errors below 0.05°. These results demonstrate that the algorithm is robust under low SNR conditions, making it suitable for reliable star sensing in long-term lunar missions.

Keywords: Star sensor, lunar surface navigation, centroiding algorithm, image preprocessing, attitude determination.

ملخص البحث

تلعب مستشعرات النجوم دوراً محورياً في الملاحة الفضائية، حيث توفر تحديداً موثوقاً لوضعية المركبات الفضائية، وهو أمر يكتسب أهمية خاصة للمهمات القمرية المستقبلية مثل المحطة الدولية للأبحاث القمرية. ومع ذلك، فإن العمل على سطح القمر يفرض تحديات فريدة؛ إذ تؤدي الانعكاسات الشمسية القوية المنبعثة من التربة القمرية، إلى جانب الإشعاعات الكونية والشمسية، إلى توليد ضوضاء كبيرة يمكن أن تؤدي إلى تدهور جودة الصورة وتعطيل عملية اكتشاف النجوم، فضلاً عن تقليل دقة تحديد المراكز. يهدف هذا البحث إلى تطوير خوارزمية محسنة لتحديد المراكز للتغلب على الضوضاء في البيئة القمرية، بالإضافة إلى تقييم أداء الخوارزمية المقترحة. تتضمن المنهجية عدة مراحل للمعالجة الأولية، بما في ذلك نمذجة دالة انتشار النقطة لمحاكاة التمويه البصري، واستخدام المرشح المتوسط لقمع الضوضاء. بعد ذلك، يتم تقسيم مناطق النجوم باستخدام طريقة العتبة العالمية، حيث يتم تعريف قيمة العتبة كدالة لكثافة الصورة القصوى. ويتم حساب مركز كل نجم مكتشف باستخدام نهج مركز الكتلة المرجح بالكثافة. تم التحقق من دقة الطريقة المقترحة عن طريق تحويل إحداثيات المراكز القائمة على البكسل إلى إحداثيات سماوية من خلال التحويل التآلفي، متبوعاً بتحديد النجوم باستخدام فهرس هيباركوس للنجوم .أُجري التقييم التجريبي لمحاكاة بيئة سطح القمر تحت ظروف ضوضاء مصطنعة، شملت ضوضاء بواسون–جوسيان، وضوضاء الملح والفلفل، والضوضاء النمشية، وتوهج ضوء الشمس. أظهرت النتائج أن الخوارزمية المقترحة تفوقت على الطرق التقليدية مثل طريقة مركز الكتلة، وملاءمة جوسيان، وخوارزمية البحث الغربالي، محققةً أدنى متوسط لجذر متوسط مربع الخطأ قدره 1.218 بكسل، ومسافة إقليدية قدرها 1.143 بكسل. كما حافظت على معدل اكتشاف كاذب منخفض بنسبة 6.716%، وأخطاء في المسافة الزاوية أقل من 0.05 درجة. تثبت هذه النتائج متانة الخوارزمية في ظروف نسبة الإشارة إلى الضوضاء المنخفضة، مما يجعلها مناسبة للاستشعار الموثوق للنجوم في المهمات القمرية طويلة الأمد.

APPROVAL PAGE

I certify that I have supervised and read this study and that in my opinion, it conforms to acceptable standards of scholarly presentation and is fully adequate, in scope and quality, as a dissertation for the degree of Master of Science in Engineering

……………………………….
Yasser Asrul Ahmad
Supervisor

……………………………….
Teddy Surya Gunawan
Co-Supervisor

……………………………….
Othman Omran Khalifa
Co-Supervisor

I certify that I have read this study and that in my opinion it conforms to acceptable standards of scholarly presentation and is fully adequate, in scope and quality, as a dissertation for the degree of Master of Science in Engineering

……………………………….
Norazlina binti Saidin
Examiner

……………………………….
Bahbibi binti Rahmatullah
External Examiner

This dissertation was submitted to the Department of Electrical and Computer and is accepted as a fulfilment of the requirement for the degree of Master of Science in Engineering

……………………………….
Othman Omran Khalifa
Head, Department of Electrical and Computer

This dissertation was submitted to the Kulliyyah of Engineering and is accepted as a fulfilment of the requirement for the degree of Master of Science in Engineering

……………………………….
Khairul Azami Sidek Dean, Kulliyyah of Engineering

DECLARATION

I hereby declare that this dissertation is the result of my own investigations, except where otherwise stated. I also declare that it has not been previously or concurrently submitted as a whole for any other degrees at IIUM or other institutions.

Anis Hannani binti Razaman

Signature…………………………… Date..29/5/2026………….

INTERNATIONAL ISLAMIC UNIVERSITY MALAYSIA

DECLARATION OF COPYRIGHT AND AFFIRMATION OF FAIR USE OF UNPUBLISHED RESEARCH

AN ENHANCED CENTROIDING APPROACH FOR ACCURATE STAR DETECTION UNDER LUNAR SURFACE NOISE CONDITIONS

I declare that the copyright holder of this thesis/dissertation are jointly owned by the student and IIUM.

No part of this unpublished research may be reproduced, stored in a retrieval system, or transmitted, in any form or by any means, electronic, mechanical, photocopying, recording or otherwise without prior written permission of the copyright holder except as provided below

1. Any material contained in or derived from this unpublished research may only be used by others in their writing with due acknowledgement.

2. IIUM or its library will have the right to make and transmit copies (print or electronic) for institutional and academic purpose.

3. The IIUM library will have the right to make, store in a retrieval system and supply copies of this unpublished research if requested by other universities and research libraries.

By signing this form, I acknowledged that I have read and understand the IIUM Intellectual Property Right and Commercialization policy.

Affirmed by Anis Hannani binti Razaman

……………………………… 29/5/2026 …………………..

Signature Date

This thesis is dedicated to both my parents for laying the foundation of what I turned out to be in life.

ACKNOWLEDGMENT

All glory is due to Allah, the Almighty, whose Grace and Mercies have been with me throughout the duration of my program. Although, it has been tasking, His Mercies and Blessings on me ease the herculean task of completing this thesis.

I would like to express my sincere gratitude to my supervisor, Dr. Yasser Asrul Ahmad, for his invaluable guidance, continuous support, and constructive feedback throughout the course of this research. His insight and patience greatly contributed to the completion of this thesis. I am also deeply thankful to my co-supervisors, Prof. Teddy Surya Gunawan and Prof. Othman Omran Khalifa, for their encouragement, expertise, and thoughtful suggestions, which helped strengthen the quality of this work.

I am especially grateful to my parents for their unwavering support, constant encouragement, and heartfelt dua, which have been a source of strength and motivation throughout my academic journey. I would also like to express my deepest appreciation to my husband, Tuan Muhammad Aidiel, for always being there throughout my journey no matter the circumstances. His endless support, patience, understanding, and encouragement have been a constant source of comfort and strength during the completion of this thesis.

Finally, I would like to thank my friends and extended family for their understanding, moral support, and encouragement during the challenging stages of this research. Their kindness and support are sincerely appreciated.

Once again, we glorify Allah for His endless mercy on us one of which isenabling us to successfully round off the efforts of writing this thesis. Alhamdulillah.

TABLE OF CONTENTS

LIST OF TABLES

LIST OF FIGURES

LIST OF ABBREVIATIONS

1D CNN	One-dimensional Convolutional Neural Network
APS	Active Pixel Sensor
CCD	Charge-Coupled Device
CMOS	Complementary Metal-Oxide Semiconductor
CoG	Centre of Gravity
COM	Centre of Mass
CTIA	Capacitive Transimpedance Amplifier
Dec	Declination
FDR	False Detection Rate
FGF	Fast Gaussian Fitting
FIR	False Identification Rate
FOV	Field of View
FSIM	Feature Similarity Index
GF	Gaussian Fitting
GPS	Global Positioning System
HIP	Hipparcos Star Number
ILRS	International Lunar Research Station
LIS	Lost in Space
LRO	Lunar Reconnaissance Orbiter
MGOA	Modified Grasshopper Optimization Algorithm
PSF	Point Spread Function
PSNR	Peak Signal to Noise Ratio
RA	Right Ascension
RMSE	Root Mean Squared Error
SAR	Synthetic Aperture Radar
SNR	Signal to Noise Ration
SSA	Sieve Search Algorithm

CHAPTER 1

INTRODUCTION

1.1 RESEARCH BACKGROUND

For centuries, stars and constellations have been used as reference points for navigation by fishermen and sailors. The unique arrangements of stars can indicate directions, dates and even the seasonal changes. With the advancement of the technologies such as the Global Positioning Systems (GPS), digital charts and radar, stars have found new applications, particularly in space navigation. In space, astronomers and aerospace engineers use star sensors to detect star patterns, recognize positions, and determine the attitude of spacecraft and satellites. Unlike other celestial references such as Earth, the Sun, or the moon, stars provide a more stable and accurate basis for orientation calculations and have abundance of reference points (Wu et al., 2023). In space missions, attitude determination is a fundamental aspect of spacecraft navigation, with star cameras, serving as vital instruments for this purpose. Star sensors, a core component of star trackers, further enhance navigation precision through their lightweight design, low power consumption, and high accuracy (Feng et al., 2019). A crucial technique employed in star trackers is centroiding, which is used to determine the precise positions of stars within an image. This process involves two main steps: image segmentation, which removes background noise to isolate star information, and centroid extraction, which identifies star points and determines their precise locations (Fan et al., 2019). These extracted positions are then utilized to estimate the orientation (attitude) of a spacecraft or satellite, enabling precise navigation.

The absence of day-night cycles and atmospheric interference on the lunar surface makes star centroiding an effective method for navigation in lunar missions. However, lunar navigation presents several challenges, such as bright solar reflections from the lunar regolith interfering with star detection and cosmic and solar radiation introducing noise into the imaging process. The lunar regolith, composed of fine, reflective dust, exacerbates these challenges by increasing interference during star detection (Dai et al., 2014). The recent surge in lunar exploration has underscored the importance of developing robust navigation systems for long-term missions. For instance, the International Lunar Research Station (ILRS), a collaboration between China and Russia also open for international collaboration that formally agreed upon in 2021 and approved in 2023 (Anqi Fan, 2023), highlights the growing demand for precise and reliable navigation solutions. Developing advanced centroiding algorithms tailored to star trackers is critical to overcoming the challenges of lunar surface navigation and ensuring the success of future space missions.

1.1 PROBLEM STATEMENTS

As mentioned previously, star-based navigation systems are increasingly considered for future lunar surface missions, such as those envisioned under the International Lunar Research Station (ILRS) and Turkish Lunar Mission (Anqi Fan, 2023; İnaltekin et al., 2023; Yağlioğlu et al., 2023). Unlike Earth-orbital operations, the lunar environment introduces several challenges for optical navigation systems. Intense solar reflections from the lunar regolith, combined with radiation-induced disturbances, introduce complex noise characteristics that alter star image intensity distributions. These environmental effects can degrade star detection reliability and centroiding accuracy, yet their impact under realistic lunar conditions has not been thoroughly examined.

Most existing star centroiding algorithms are developed and evaluated using idealized imaging conditions or spaceborne scenarios with relatively stable SNR (Mahi et al., 2024; Mahi & Karoui, 2019; S et al., 2024). When these methods are applied to low SNR, uneven illumination and increased noise level, performance often degrades (Mahi et al., 2024). This indicates a need for a centroiding approach that is specifically tuned to lunar conditions, with appropriate parameter selection and preprocessing steps to ensure reliable star position estimation.

In addition, many reported centroiding methods focus primarily on accuracy and computational efficiency, with limited attention given to verifying whether detected features are actual stars or false detections caused by noise (Fan et al., 2019; Karaparambil et al., 2023; Mahi et al., 2022). For navigation purposes, this uncertainty can lead to unreliable attitude estimation if false positives are included in the process. Therefore, validating detected star positions against established star catalogues and comparing performance with existing centroiding methods is essential to demonstrate the robustness and practical reliability of a centroiding algorithm for lunar navigation applications.

1.2 RESEARCH OBJECTIVES

This research aims to develop and optimize the centroiding algorithm for moon surface navigation using star sensor and evaluate the algorithm performance. The main objectives of this research include:

1. To investigate the influence of lunar environmental factors and noise characteristics on star detection and centroiding accuracy by implementing simulated noises into the star images.
2. To develop an enhanced centroiding algorithm by implementing image segmentation techniques and centroiding computation to improve star position estimation.
3. To evaluate the performance of the proposed centroiding algorithm by benchmarking the algorithm against established centroiding methods.

1.2 RESEARCH SCOPE

This research focuses on the development and evaluation of a star sensor image processing pipeline for lunar surface navigation. The scope includes the design of the image segmentation and filtering for noise suppression. Next, the formulation of mathematical model for accurate star centroid estimation. Subsequently, the implementation of identification algorithm for star position matching with a reference star catalogue. Star images are generated using the Stellarium software and displayed on a monitor, which are then captured using a prototype system integrating a Raspberry Pi 5 processor with an ArduCAM OV2311 global shutter camera. Stellarium was selected as the image source because it provides real-time sky simulations containing stars, satellites, and other celestial objects. The performance of the proposed centroiding algorithm is evaluated by comparison with established centroiding methods in terms of detection rate, positional error, and root mean squared error (RMSE).

Due to practical limitations in the observation environment, this study does not involve direct acquisition of real night-sky star images. In Malaysia, high atmospheric humidity, frequent cloud cover, light pollution, and weather variability significantly limit consistent night-sky visibility. Accurate star imaging would require access to specific remote locations with minimal light pollution and stable atmospheric conditions, which were not practically available within the scope of this research. Instead, controlled star images from Stellarium are used to ensure repeatability and consistency in performance evaluation. Furthermore, as the primary focus of this research is on image extraction and centroiding accuracy, full Lost-in-Space (LIS) star identification is beyond the scope of this work. Star identification is therefore conducted using a limited set of reference stars obtained from Stellarium, sufficient for validating the centroiding performance under simulated lunar conditions.

1.3 THESIS ORGANISATION

This thesis is organized into five chapters. Chapter 1 introduces the research, including the research background, problem statements, objectives, and scope of the study, which set the foundation for the work. Chapter 2 reviews existing literature on star detection, centroiding algorithms, and the challenges associated with lunar navigation. This includes an analysis of current techniques and their limitations. Chapter 3 outlines the methodology, describing the proposed approach to develop and validate the centroiding algorithm. Chapter 4 presents the results and outcomes of the experiment, offering insights into the effectiveness of the proposed algorithm. Finally, Chapter 5 concludes the thesis by summarizing the key findings and discussing potential improvements and directions for future work.

CHAPTER 2

LITERATURE REVIEW

2.1 OVERVIEW

This chapter surveys existing research on star camera systems, with particular attention given to the performance of CMOS and CCD sensors in radiation-intensive space environments. It further examines the characteristics of the lunar surface, explaining how regolith reflectance and abrupt lighting transitions contribute to a reduced signal-to-noise ratio. Common noise models, such as Gaussian and Poisson noise, are reviewed as tools for simulating these challenging conditions. The chapter also analyses established centroiding and star identification algorithms, including the Pyramid and Sieve Search methods, in order to identify their strengths and limitations within lunar navigation contexts.

2.2 STAR CAMERA FOR SPACE AND LUNAR EXPLORATION

Star cameras are the most crucial components used in a star tracker for modern space missions. These sensors are the optical sensors designed to determine a spacecraft's attitude by observing the positions of stars in the field of view. Figure 2.1 illustrates the block diagram of a star sensor system.

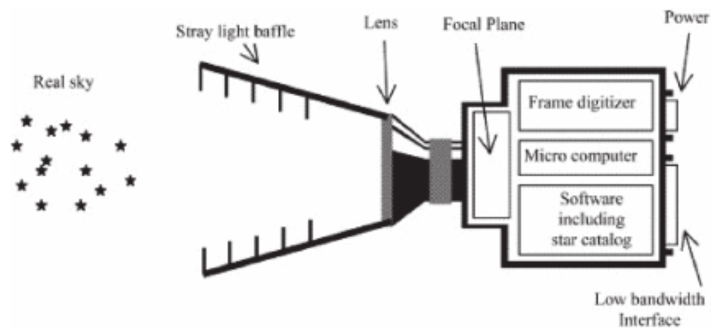

Figure 2.1: Example of star sensor block diagram (Hailong et al., 2015)

Star trackers provide greater accuracy than other attitude sensors like magnetometers, gyroscopes, sun sensors, and earth horizon sensors (Qian et al., 2016). Two main types of imaging sensors are typically considered for star trackers: complementary metal-oxide semiconductor (CMOS) and charge-coupled device (CCD) (Fossum & Hondongwa, 2014). Active Pixel Sensor (APS) CMOS technology is especially suited for space missions, as it offers high integration, better resistance to radiation, lower power use, and lower cost compared to CCDs, making it ideal for power-constrained lunar missions (Xing et al., 2006). Research by Feng et al. studies on the radiation effect on the CCD and CMOS image sensor (Feng et al., 2019). In this experiment, a CCD image sensor used in star sensors is subjected to proton radiation to assess its performance under radiation exposure. The methodology involves irradiating the sensor with 3.0 MeV protons across a range of fluences, up to 7.36 x 10^10 p/cm², simulating cumulative space radiation damage. The experiment has also been done with a CMOS image sensor. As radiation fluence increases, the clarity of star images declines, with stars appearing progressively blurred and dark noise becoming more prominent. Both experiments brought to the conclusion that although CCD sensor can output images, the increasing of the noise caused the dark signal increases dramatically. Therefore, the accuracy of parameter calculation also decreases. For CMOS image sensor proton radiation experiment, the imaging performance is decreased but the mean square error of the star centroid has no obvious dependence on the proton radiation. This comparison of CMOS and CCD shows CMOS as the better choice, especially given the power and durability demands on the moon's surface.

Additionally, Figure 2.2 shows two types of star tracker used for smaller spacecraft. The first one, Figure 2.2(a) is the KU Leuven from CubeSat Pointing, a star tracker with low-cost space access for technology testing, scientific research and communications. Figure 2.2(b) is the ST-16RT2 from Rocket Lab, designed for operations in small spacecraft and has been part of several missions such as GHGSat-C3, Lemur, and Mandrake-1 (SATNow, 2023).

(a) (b)

Figure 2.2: (a) KU Leuven from CubeSat Pointing, (b) ST-16RT2 from Rocket Lab (SATNow, 2023)

Historically, star trackers were implemented in early missions such as Apollo, where the Command Module and Lunar Module relied on optical star sightings for trajectory corrections and lunar descent navigation (Trageser & Hoag, 1965). With technological advancement, modern digital star cameras have been deployed on numerous interplanetary spacecraft, including NASA's Cassini, Dawn, and New Horizons missions, all of which utilised star trackers as their primary attitude reference during cruise phases and scientific operations (Rayman et al., 2006). For lunar exploration, the Lunar Reconnaissance Orbiter (LRO) employs high-performance star trackers to maintain stable pointing for imaging and altimetry instruments (Chin et al., 2007).

China's Chang'e lunar missions also incorporate star sensors for spacecraft stabilization. Chang'e 5-T1 is an experimental robotic lunar mission launched by China in 2014 and it acted as a test flight for the Chang'e 5 mission. The Chang'e-3 and Chang'e-4 landers used star trackers during transfer orbit and lunar orbit insertion phases, while the Queqiao relay satellite for Chang'e-4 utilised them to maintain Earth-Moon L2 halo orbit operations (Li et al., 2021; Wang & Liu, 2016). The Artemis program, including the Orion spacecraft, applies advanced star trackers integrated with optical navigation to enhance redundancy and resilience during deep-space flight (NASA, 2022).

(a) (b)

Figure 2.3: (a) Chang'e 5-T1 re-entry capsule after landing, (b) Chang'e 3 lander on lunar surface (China Space Record, 2016; China Space Report, 2016)

In recent years, the increasing interest in autonomous navigation for lunar landers, rovers, and orbiters has led researchers to adapt star sensors specifically for the Moon's illumination and surface conditions (Ceresoli et al., 2025; Chen et al., 2024). Optical disturbances such as glare from the lunar horizon, stray sunlight, and low signal to noise ratio (SNR) conditions affect the visibility of faint stars. These factors make accurate centroiding more difficult, requiring algorithms that are more resistant to noise, saturated pixels, and varying levels of image degradation. As missions move toward autonomous, onboard localization systems, the reliability of centroiding and star identification becomes increasingly critical, especially when GPS and Earth-based tracking are unavailable.

2.3 UNDERSTANDING THE MOON SURFACE

The Moon's surface environment presents a unique combination of physical and optical challenges that directly influence star detection and centroiding performance for lunar-based observation and navigation systems. Structurally, the lunar surface consists of the highlands, which are ancient and heavily cratered with high albedo anorthosite, and the maria, darker basaltic plains formed by volcanic activity (Wilhelms et al., 1987).

The top layer, known as lunar regolith, is composed of fine dust, rock fragments, and glass particles produced by continuous micrometeoroid bombardment (H. Lin et al., 2020a). This regolith creates strong reflection variations that contribute to background brightness and can interfere with the imaging performance of star sensors. The lunar regolith presents at the crust of the lunar layers, as shown in Figure 2.4, and the detailed sample of granular material that resembles dark, fine-grained sand or dirt shown in Figure 2.5 (R. Li et al., 2023; NASA, 2025).

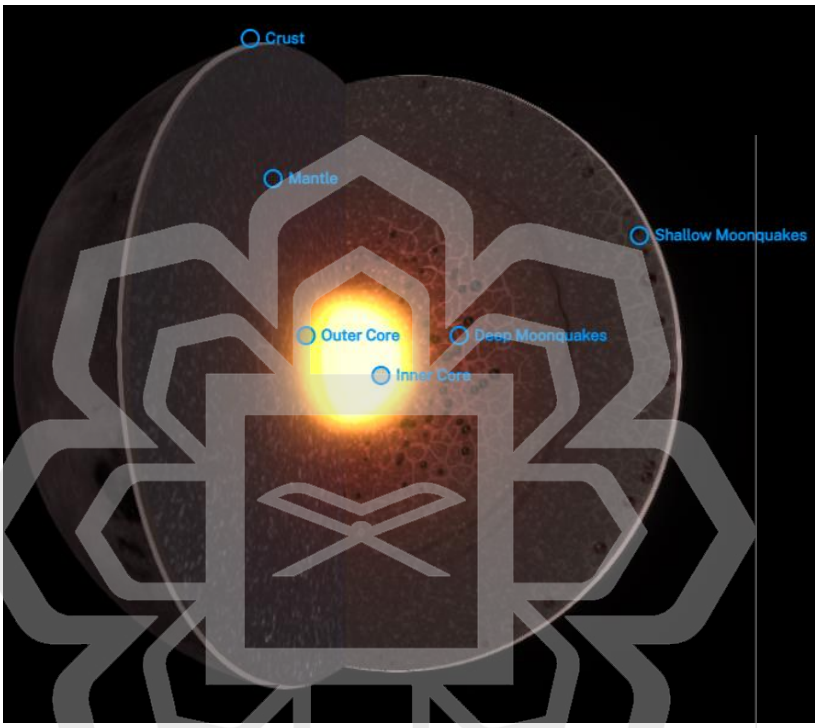

Figure 2.4: The regolith that considered to be the uppermost layer of the lunar crust (NASA, 2025)

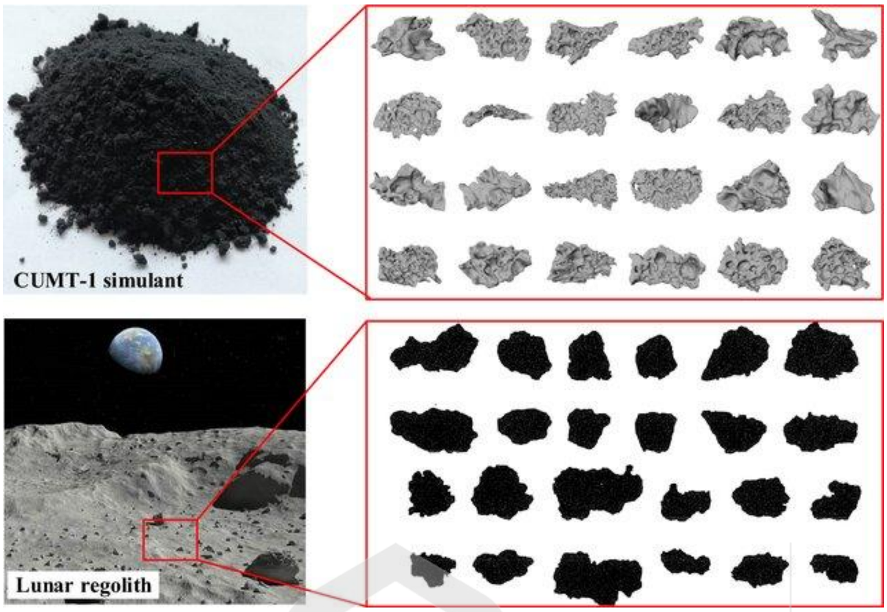

Figure 2.5: Detailed visualization of a lunar regolith simulant of CUMT-1 (China University of Mining and Technology-1) (R. Li et al., 2023)

A defining characteristic of the lunar environment is the absence of a substantial atmosphere where the sky remains completely black even during daytime without the atmospheric scattering. However, this condition also introduces several noise challenges. The most dominant factor is direct solar illumination, which produces extreme contrast between illuminated and shadowed regions, with brightness ratios often exceeding $10^6:1$ (Frazor & Geisler, 2006). Sunlight reflecting off the regolith can generate glare, veiling luminance, and bright background gradients, all of which reduce the effective SNR for faint stars (Zou et al., 2004). Additionally, electrostatic charging of lunar dust can lift particles above the surface, creating horizon glow and forward-scattering effects that introduce (Horányi et al., 2024; Rennilson & Criswell, 1974).

Thermal variations further complicate imaging. Lunar surface temperatures range from approximately $+120°C$ during the day to $-170°C$ at night, affecting detector sensitivity and increasing thermal noise and dark current, especially in CMOS or CCD sensors used in star cameras (Holst & Lomheim, 2011; Paige et al., 2010). These extreme conditions make it challenging for star sensors to maintain consistent performance throughout a full lunar day-night cycle. A study presents an illumination condition analysis for the lunar polar region using multi-temporal high-resolution orbital imagery, with the pre-selected Chang'E-7 landing site serving as the evaluation area (Zhang et al., 2023). Figure 2.6 presents an analysis of this study located at the South Pole of the Moon.

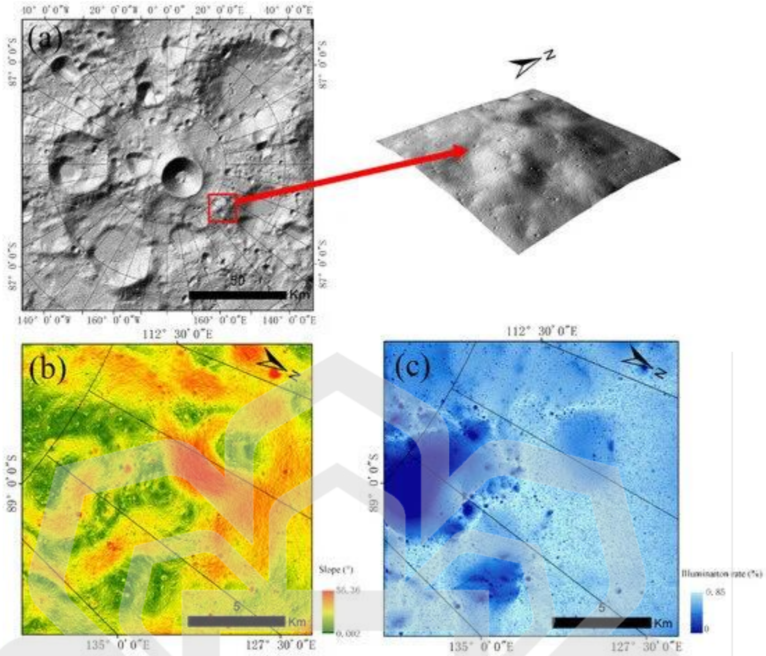

Figure 2.6: The slope and average illumination of the study area (Zhang et al., 2023)

In the context of star detection, these environmental conditions contribute to several noise models typically observed in lunar-based imaging systems. High illumination and photon variability often lead to Poisson noise, while electronic readout processes generate Gaussian noise and dark current noise (Chukhovskii et al., 2023). These noise models will be discussed in detail in the next section.

2.4 DIFFERENT TYPES OF NOISE

The lunar environment introduces several challenges that can interfere with reliable star detection and centroiding. Due to the Moon's lack of atmosphere, there is no scattering medium to diffuse sunlight, resulting in extremely harsh illumination contrasts. Additionally, the naturally low brightness of stars observed from the lunar surface, these factors significantly degrade the SNR, making accurate star extraction much more difficult. NASA's Diviner and Apollo mission studies confirm that the Moon exhibits extreme lighting transitions and strong solar reflections, which can heavily affect optical imaging systems (NASA, n.d.-b; Rafael Alanis, 2010). A low SNR directly affects centroiding performance by reducing star visibility, increasing false detections, and degrading positional accuracy (Liebe, 2002).

Table 2.1: Noise and representations in Lunar environment

Simulated Noises	**Representations**
Gaussian noise	Represents sensor electronic noise, such as thermal fluctuations in readout circuits, electronic sensor noise, and photon measurement randomness at low light level (Y. Li et al., 2019).
Poisson noise	Simulates photon shot noise caused by the random nature of photon arrivals, which is amplified by the Moon's lack of atmosphere and the extreme contrast between illuminated and shadowed regions (Pan et al., 2025).
Salt and pepper noise	Replicates impulse noise or high-contrast disruptions, specifically representing hardware/software failures, camera sensor defects, faulty pixels, or cosmic ray strikes (Feng et al., 2019).
Speckle noise	Simulates multiplicative disturbances where noise scales with intensity, representing sensor gain fluctuations, optical imperfections, or rapid brightness changes caused by reflections from lunar dust or spacecraft surfaces (Wong et al., 2014).
Light glare	Models intense solar reflections from the lunar regolith and direct solar illumination, which produce bright background gradients, veiling luminance, and structured light artifacts (Zhang et al., 2023).

To recreate these lunar imaging challenges during algorithm development, several noise models are commonly adopted to simulate degraded star fields. The primary noise types relevant to lunar surface star detection include Gaussian noise, Poisson noise, salt and pepper noise, and speckle noise (Chukhovskii et al., 2023; Painam & Suchetha, 2022; Parhad et al., 2023; Xu et al., 2020). These models allow realistic assessment of algorithm robustness under photon-limited, illumination-disturbed, and sensor-corrupted conditions. Noise in digital images can generally be described as undesired variations in brightness or colour information, often visible as grainy texture or random intensity fluctuations (Othman Omran Khalifa, 2021). Each noise type arises from different physical or electronic mechanisms, and understanding their properties is essential for selecting appropriate mitigation strategies. The summary of the noises can be viewed in Table 2.1.

2.4.1 Gaussian Noise

The Gaussian distribution is a statistical probability distribution defined by a mean (μ) and a standard deviation (σ), describing how values are spread around the mean. Gaussian noise, on the other hand, is an image noise model generated based on this distribution. In contrast, Gaussian noise refers to random intensity variations added to an image, where these variations are drawn from a Gaussian (normal) distribution (Wan et al., 2018). Gaussian noise is commonly used to simulate sensor noise in optical devices and is mathematically characterised by its probability density function (Othman Omran Khalifa, 2021):

$$p(x) = \frac{1}{\sqrt{2\pi\sigma^2}} exp\left(-\frac{(x-\mu)^2}{2\sigma^2}\right) \tag{2.1}$$

where approximately 70% of pixel variations lie within $(\mu - \sigma, \mu + \sigma)$ and 95% lie within $(\mu - 2\sigma, \mu + 2\sigma)$. The parameters μ defines the central tendency or 'average' noise level, while σ defines the intensity or 'strength' of the noise. A higher σ indicates a noisier image with more significant pixel variations. The difference of the Gaussian distribution bell shape shown in Figure 2.7.

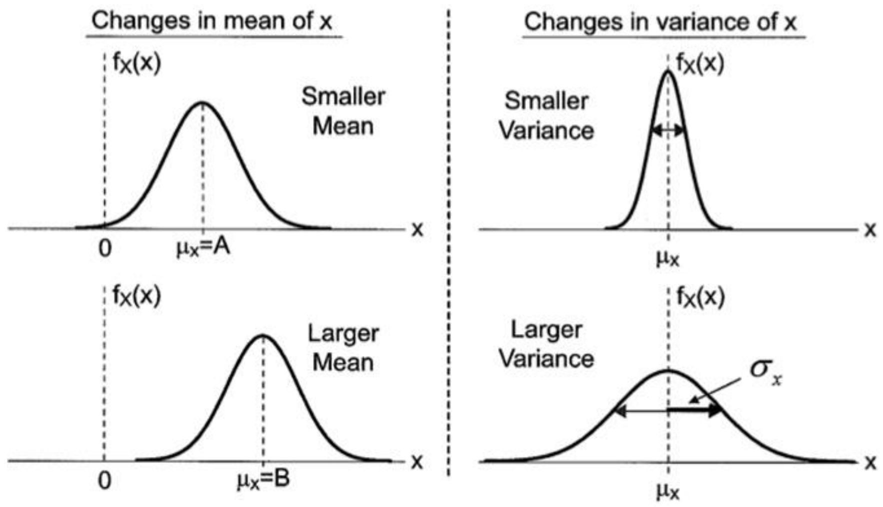

Figure 2.7: Illustration of Gaussian distributions with varying parameters (Hari Balakrishnan et al., 2010).

From the illustration in Figure 2.7, adjusting the mean of a Gaussian distribution simply shifts the position of its peak, effectively moving the entire distribution along the intensity axis. In contrast, modifying the variance changes the spread of the distribution, causing the curve to become wider or narrower (Moo K. Chung, 2007; Xu et al., 2020). Additionally, Gaussian noise typically arises from thermal fluctuations in the sensor electronics, readout circuits, or photon measurement randomness at low light levels (Li et al., 2019). The noise function follows:

$$n(x, y) \sim N(\mu, \sigma^2) \tag{2.2}$$

Where μ is the mean and $\sigma$is the standard deviation of the noise. Gaussian noise smooths fine details and reduces the contrast between stars and background sky, creating difficulty in distinguishing faint stars, particularly problematic under the low-SNR conditions expected on the Moon.

(a) (b)

Figure 2.8: Different image quality (a) original quality, (b) gaussian noise added (Barbu, 2013)

In Figure 2.8(a), the original image is shown with clean intensity distribution and well-defined edges. After Gaussian noise is applied, as shown in Figure 2.8(b), the image becomes grainier due to the random fluctuations introduced around each pixel value based on the Gaussian distribution.

2.4.2 Salt and Pepper Noise

Salt and pepper noise is found only in grayscale images (black and white image). As the name suggests salt (white) in pepper (black) white spots in the dark regions or pepper (black) in salt (white) black spots in the white regions (Azzeh et al., 2018; Chan et al., 2005; Erkan & Kilicman, 2016). This type of noise, also known as impulse noise, degrades image quality, resulting in information loss and unsatisfying visual effects. It is generally caused by defects of the camera sensor, software failure, or hardware failure during image capturing or transmission (W.-T. Chen et al., 2019; W. Wang et al., 2025). A pixel corrupted by salt and pepper noise takes either the minimum value (0) or the maximum value (255). The typical intensity value for pepper noise is close to 0 and the typical intensity value for salt noise is close to 255.

Salt and pepper noise is defined using a probability model. For an image x (Azzeh et al., 2018):

$$x' = \begin{cases} 0, & p_{black} \\ 255, & p_{white} \\ x, 1 - (p_{black} + p_{white}) \end{cases} \tag{2.3}$$

Where:

- x' = Noisy pixel value
- x = Original pixel value
- p_{black} = Probability that a pixel becomes black (pepper)
- p_{white} = Probability that a pixel becomes white (salt)

Total noise density, $d = p_{black} + p_{white}$. Often, salt and pepper noise is assumed to occur in equal proportions; $p_{black} = p_{white} = \frac{d}{2}$. For example, the noise density is 0.5, hence, $p_{black} = p_{white} = 0.25$.

Meaning 25% pixels become 0 and 25% become 255. Figure 2.9 illustrates the visual impact of salt and pepper noise on image quality:

(a) (b)

Figure 2.9: The cameraman different image quality, (a) original quality, (b) 50% noise added (Erkan & Kilicman, 2016)

As shown in Figure 2.9(a), the original cameraman image appears clean and detailed, whereas Figure 2.9(b) shows the same image after 50% noise density is applied, resulting in heavy black-and-white speckling that obscures most structural information. This comparison highlights how impulse noise can severely degrade image clarity, making feature detection and centroid extraction significantly more challenging.

2.4.3 Poisson Noise

Poisson noise, also known as photon shot noise, is a noise model that arises from the discrete and random nature of photon arrivals at the image sensor (Jisha J U & Sureshkumar V, 2014; Rodrigues et al., 2008; Xiang et al., 2023). Unlike additive Gaussian noise, Poisson noise is signal-dependent, meaning the noise variance increases with the signal intensity (Ghazdali et al., 2024). This makes Poisson noise particularly relevant for astronomical imaging, where light from stars is extremely faint, and the limited number of incoming photons causes fluctuations in pixel brightness. In low-light environments such as the Moon's surface where the absence of an atmosphere amplifies the stark contrast between illuminated and shadowed regions, Poisson noise becomes more pronounced due to low photon counts. Poisson noise follows a Poisson probability distribution (Chukhovskii et al., 2023):

$$P(k;\lambda) = \frac{\lambda^k e^{-\lambda}}{k!} \tag{2.4}$$

Where λ represents the expected number of photons (mean intensity), and k is the observed pixel value. Since the mean and variance of a Poisson process are equal, images with lower intensity inherently exhibit lower SNRs. This directly affects star detection because faint stars may appear indistinguishable from background fluctuations.

Figure 2.10 illustrate the noisy with the denoised image and the authors' aim to recover such degraded images by developing a self-supervised denoising model specifically designed to handle a Poisson-Gaussian noise (Khademi et al., 2020). As shown, the noisy image exhibits noticeable intensity fluctuations and graininess caused by the random nature of photon arrival.

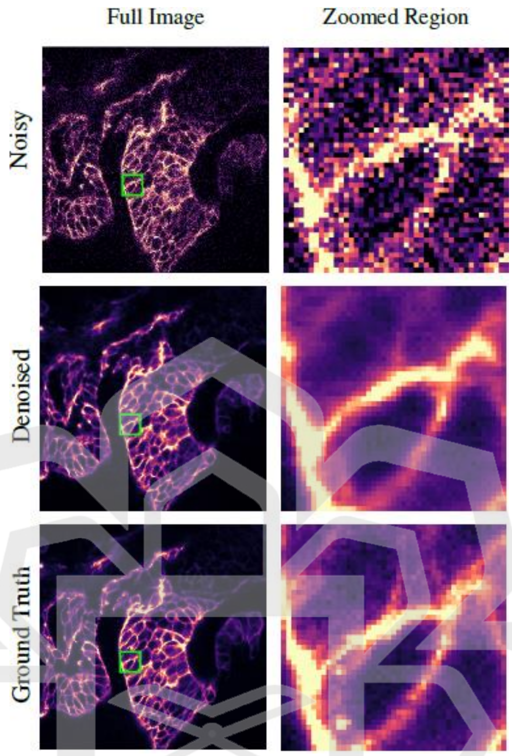

Figure 2.10: Example of denoising result (Khademi et al., 2020)

In image simulation, Poisson noise is commonly used to replicate low-photon astronomical conditions, such as lunar night imaging or deep-space star observations (Heiken et al., 1991). Adding Poisson noise in testing allows evaluation of how robust a centroiding algorithm is under realistic photon-limited environments.

2.4.4 Speckle Noise

Speckle noise is a multiplicative noise model that commonly appears in images obtained from coherent imaging systems such as radar, ultrasound, and laser-based sensors (Painam & Suchetha, 2022; Prabhishek Singh & Raj Shree, 2016). Although star cameras are not coherent imaging systems, speckle noise is still used in simulation studies to represent multiplicative disturbances that scale with image intensity. In a research, the authors study on the speckle noise reduction in Synthetic Aperture Radar (SAR) images (Parhad et al., 2023). The SAR images are commonly used in remote sensing to capture geological and biophysical features of the Earth's surface. According to Painam R et. al., due to the coherent imaging process, SAR data experience pixel-to-pixel intensity fluctuations that form a granular pattern known as speckle noise. Although speckle is primarily associated with coherent systems, it is also used in optical imaging studies as a simplified multiplicative noise model to simulate intensity-dependent disturbances. Figure 2.11 shows the quality of the satellite image is reduced by the speckle noise in a SAR image.

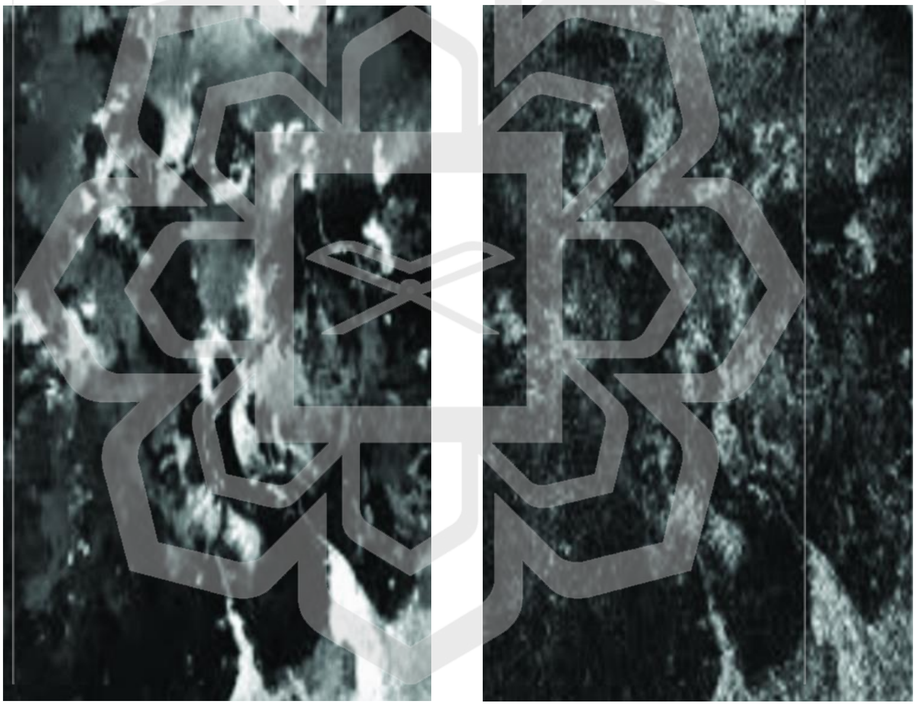

(a) (b)

Figure 2.11: SAR image degradation (a) original quality, (b) speckle noise (Kumar & Jebarani, 2019)

In the context of lunar imaging, speckle-like variance may arise due to sensor gain fluctuations, optical imperfections, or rapid brightness changes caused by reflections from lunar dust or spacecraft surfaces. Speckle noise can be mathematically described as (Prabhishek Singh & Raj Shree, 2016):

$$I_{noisy} = I \cdot n \tag{2.5}$$

Where I is the original pixel intensity and n is a noise factor drawn from a gamma distribution (Intajag & Sukkasem, 2009; R. Wang et al., 2020):

$$p(n) = \frac{n^{k-1}e^{-n/\theta}}{\theta^k \Gamma(\mathrm{k})} \tag{2.6}$$

The multiplicative nature of speckle noise causes bright regions to exhibit larger fluctuations, making centroid estimation more difficult, especially for bright star blobs with extended point-spread functions. Speckle noise can distort blob intensity profiles, causing shifts in centroid locations and irregular blob shapes.

Including speckle noise in simulation helps evaluate how centroiding algorithms behave when the noise amplitude depends on the signal itself, rather than being constant across the image. This contributes to a more comprehensive assessment of algorithm robustness under varying imaging conditions.

2.5 RELATED WORKS

In recent years, various techniques have been proposed to enhance star detection and centroiding accuracy for star trackers under noisy and challenging space conditions (W.-C. Chen & Jan, 2023; Feng et al., 2019; Mahi & Karoui, 2019). However, low SNR in star field images captured by image sensor in star tracker significantly affects the detection and centroid accuracy, as noise may distort the intensity distribution of star blobs, making it difficult to differentiate genuine stars from false detections. Hence, evaluating the detection and centroid performance under these noisy conditions allows the algorithm's robustness and reliability to be demonstrated for future lunar navigation applications (Chen et al., 2025; Chen et al., 2024).

2.5.1 Image Segmentation and Thresholding

Two fundamental techniques used in image-based star detection are segmentation and centroiding. Segmentation technique removes background noise to isolate star information, and centroiding technique is used to determine the precise positions of stars within an image (Fan et al., 2019; Mahi et al., 2024; Mahi & Karoui, 2019). These extracted positions are then utilized to estimate the orientation (attitude) of a spacecraft or satellite, enabling precise navigation (Ceresoli et al., 2025; Xing et al., 2006).

Thresholding is the simplest and most widely used technique, representing the first generation of low-level segmentation methods that rely on minimal prior information. Pixels with intensities above this threshold are classified as part of a star, while those below are treated as background noise. This approach is simple and computationally efficient, but its effectiveness is highly dependent on selecting an appropriate threshold value (Cai et al., 2014; Liang et al., 2019a; Gonzalez & Woods, 2018). According to Khalifa (2021), image segmentation involves grouping image regions that share similar characteristics to isolate relevant objects. A recent study in medical imaging by Raman et al. (2024) introduced a mixed-thresholding and edge-preservation method to effectively denoise MRI brain images while maintaining critical structural details. The thresholding dynamically responds to the noise characteristics, enabling strong noise reduction without compromising important image features. Figure 2.12(a) and (b) shows the effect of global thresholding on MRI brain images.

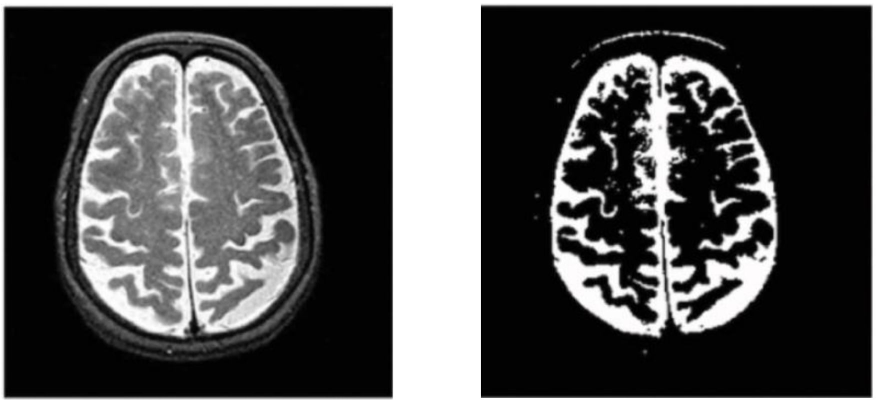

Figure 2.12: (a) input greyscale image, (b) result of global thresholding with T=150 (Raman et al., 2024)

As observed in Figure 2.12(b), this process is necessary to isolate high-intensity brain tissues from the rest of the image, creating a clear separation between the object of interest and the background.

Another research by Liang et al. (2019b), introduces a modified Grasshopper Optimization Algorithm (MGOA) for multilevel thresholding in colour image segmentation, using Tsallis entropy as the primary objective function to identify optimal thresholds efficiently. Thresholds are optimized separately for RGB channels using Tsallis entropy ($q = 0.8$), with comparisons to Otsu (between-class variance) and Renyi entropy. As the result, MGOA achieves superior segmentation accuracy, fewer iterations, higher PSNR/FSIM scores and robustness on complex colour images, validated qualitatively and statistically. Figure 2.13 shows the summary of the whole result of this research.

Figure 2.13: Boxplot representing the PSNR and FSIM for all methods (a) PSNR under Tsallis (b) FSIM under Tsallis (c) PSNR under Otsu (d) FSIM under Otsu (e) PSNR under Renyi (f) FSIM under Renyi. (Liang et al., 2019b)

The MGOA algorithm shows the best performance in term of Peak Signal to Noise Ratio (PSNR) and Feature Similarity Index (FSIM), where the PSNR value of the proposed algorithm reaches approximately 28.7 dB, 29.5 dB, and 30.5 dB under Tsallis, Otsu and Renyi respectively. The corresponding FSIM values of the proposed algorithm reach approximately 0.96, 0.97, and 0.97 under Tsallis, Otsu, and Renyi objective functions, respectively.

While both research by Raman et al. (2024) and Liang et al. (2019b), leverage thresholding for segmentation, the first one is critically defined by its hybrid methodology designed for detail fidelity and specialized medical application, whereas the second is focused on increasing the computational efficiency and accuracy of optimal multi-level threshold determination in complex images through bio-inspired algorithms, a necessity when dealing with the increased complexity of multiple segmentation levels.

2.5.2 Centroid Calculation

Following detection, the centroiding mechanism is applied to determine the precise location of each star. This involves computing the intensity-weighted average of pixel positions within a star region, resulting in a sub-pixel level estimate of the star's centre (Chen et al., 2018; Janesick, 2001). Accurate centroiding is crucial for applications such as spacecraft attitude determination, as even small errors can lead to significant orientation inaccuracies. Liebe (2002) emphasizes that star tracker accuracy is largely determined by the precision of its centroiding algorithm, which must account for image noise, pixel quantization, and optical distortions.

Research by Wan et al. (2018), develops a fast Gaussian fitting (FGF) algorithm for star centroiding in star sensors to enable real-time processing while matching the accuracy of traditional Gaussian fitting (GF) (Wan et al., 2018). FGF refines the centroid on these high-SNR pixels by transforming the nonlinear GF objective, into a linear least-squares problem via log approximation with SNR weights $r_i \approx 1$, solved in closed form without iterations. The conventional Gaussian fitting equation by Wan et al. (2018):

$$min \sum_i (I_i - S_i)^2 \tag{2.7}$$

Taking the natural logarithm of both sides of I_i and S_i, the objective function becomes:

$$min \sum_i I_i(\ln I_i - \ln S_i)^2 \tag{2.8}$$

Where I_i is measured pixel intensity and S_i is modelled Gaussian intensity. The results summary of this research can be observed in Figure 2.14 and 2.15.

Figure 2.14(a) illustrates the positions of all stars, where red asterisks represent the proposed algorithm performs better than that of the Centre of Gravity (CG). The comparison shows the proposed method is most effective near the centre of the image plane, where star spot intensity conforms most accurately to the Gaussian function. The data also reveals that the CG method can perform slightly better at the extreme edges of the field of view, where optical distortions prevent star spots from strictly following a Gaussian distribution.

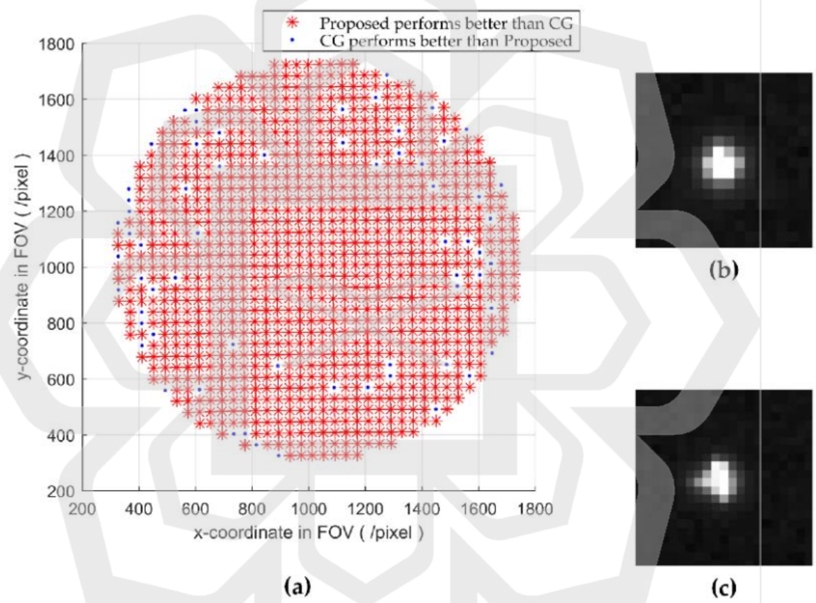

Figure 2.14: The centroiding result of the two algorithms (a) positions of all stars (b) star spot captured in (1048,847) (c) star spot captured in (493,559) (Wan et al., 2018)

Figure 2.15 demonstrates that the proposed algorithm achieves a centroiding error nearly identical to the GF method across all tested radii, which is considered the theoretical accuracy limit. While the CG and weighted methods suffer from significant S-curve errors at small Gaussian radii (around 0.5), the proposed method remains stable and accurate. It highlights that the proposed approach outperforms the Gaussian Analytic (GA) method, particularly when the star spot radius exceeds 1.4 pixels, where the GA's error begins to increase.

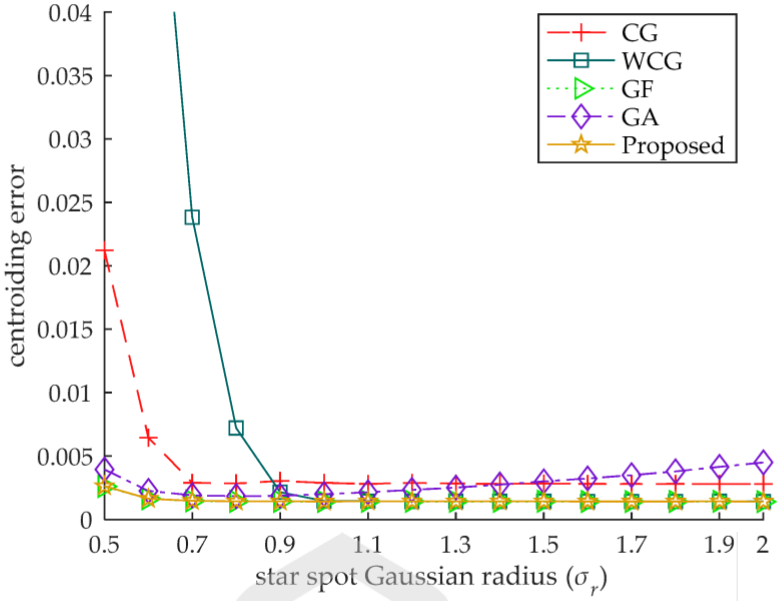

Figure 2.15: Centroiding error under different spot radius (Wan et al., 2018)

Another novel technique, the Sieve Search Centroiding Algorithm (SSA) by Karaparambil et al. (2023), improves accuracy by dividing images into smaller sub-regions and analysing intensity distributions to compute the COM. The common COM formula:

$$x_c = \frac{\sum_{x,y} x \cdot I(x,y) \cdot w(x,y)}{\sum_{x,y} I(x,y) \cdot w(x,y)}, y_c = \frac{\sum_{x,y} y \cdot I(x,y) \cdot w(x,y)}{\sum_{x,y} I(x,y) \cdot w(x,y)} \tag{2.9}$$

While it offers speed advantages over complex fitting algorithms, its sensitivity to noise and parameter variations remains a challenge.

Figure 2.16 illustrates how centroiding accuracy varies as the brightness barycentre shifts between the primary and secondary stars. When the secondary star is fainter than 4 VM (visual magnitude), most methods including COM, Gaussian best fit (GBF), Gaussian three-point centroiding (G3P), FGF, and SSA, estimate the centroid accurately, while iterative weighted centre of gravity (IWCOG) and Gaussian Analytic Centroiding (GAC) show noticeable errors due to sensor noise and photo-electron spillover. As the secondary brightens, only SSA continues to follow the true centroid, maintaining an error below 0.2 pixels across the full operational range. SSA suffers from accuracy limitations when dealing with star spots having a small Gaussian radius, making it susceptible to S-curve errors similar to other grey-scale methods, though less severely than COM or IWCOG. Furthermore, while SSA is much faster than fitting methods, it is still inherently slower than the simplest grey-scale algorithms like COM or Gaussian Analytic Centroiding (GAC).

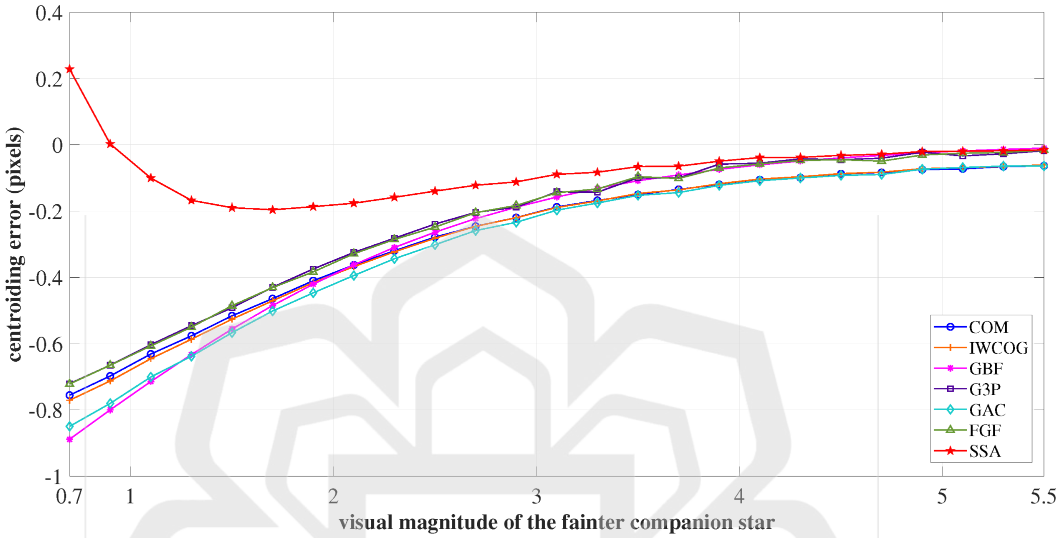

Figure 2.16: Centroiding error in estimating the brightness barycentre of an optical double-star pair (Karaparambil et al., 2023)

A study introduced a dual-stage algorithm combining object segmentation and centroid extraction to eliminate non-stellar bright objects (Mahi et al., 2024). The primary contribution of this research is the effective pre-processing workflow designed specifically to mitigate the challenge of non-stellar big bright objects appearing in the star tracker's field of view. The centroiding technique proposed relies either on Centre of Gravity (CoG) or locating the pixel of maximum intensity.

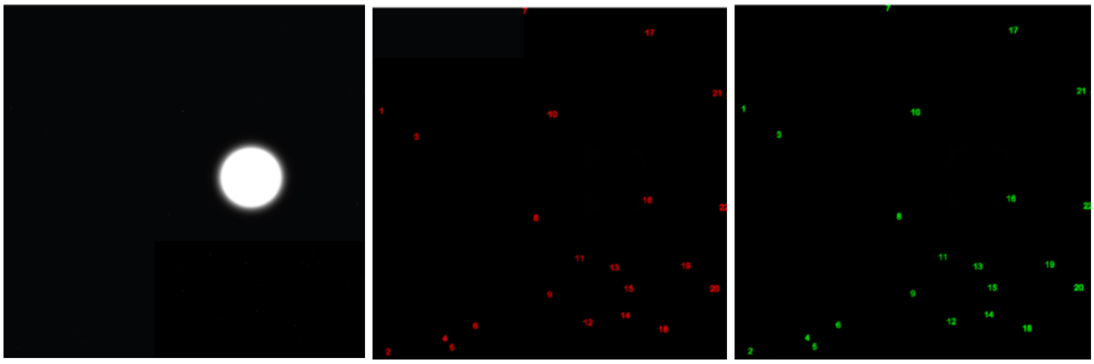

(a) (b) (c)

Figure 2.17: Centroiding results (a) star image with big non-stellar big bright object (b) star position extraction by the first process (c) star position extraction by the second process (Mahi et al., 2024)

Figure 2.17 provides a visual comparison of the results achieved by Mahi's star centroiding algorithm, which includes steps for non-stellar big bright object elimination and star position extraction. In Figure 2.17(b), the first process involves star detection, elimination of non-stellar large bright objects, and star position extraction using the CoG algorithm. The second process involves star detection, non-stellar large bright object elimination, and star position extraction using the proposed star centroid method. However, Mahi et al., (2024) explicitly states that both proposed algorithms are limited in their ability to detect stars that are heavily affected by sunlight. Although the algorithm aims to remove the illumination effect introduced by non-stellar bright objects that are close to the field of view, intense sunlight still hinders the detection capability.

Additionally, advancements in sensor technology, such as the global-shutter centroiding measurement Complementary Metal-Oxide-Semiconductor (CMOS) image sensor with Capacitive Transimpedance Amplifier (CTIA) pixels, have shown improved centroiding performance by over 1% relative to commercial sensors (Qian et al., 2016). Figure 2.18 illustrates the graph of the averaged relative distance error of the algorithm by Qian et al. (2016).

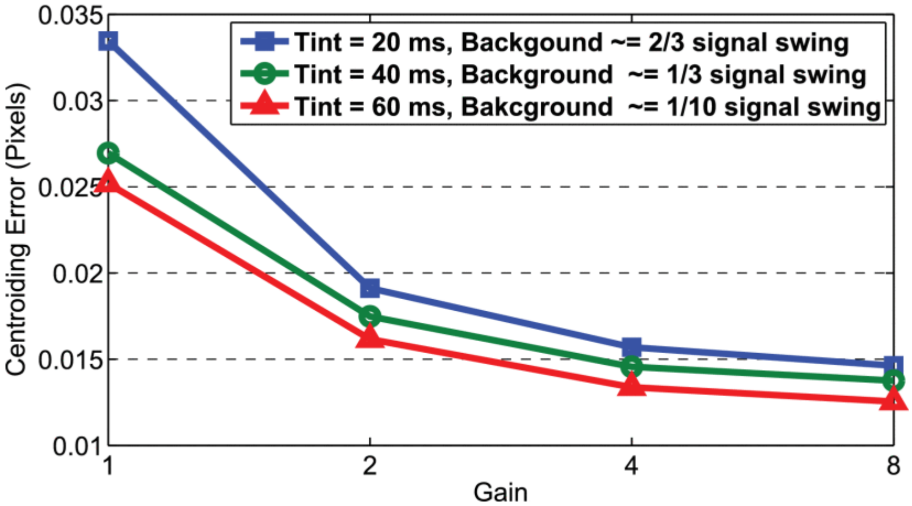

Figure 2.18: Measured relative distance error (Qian et al., 2016)

From the figure, the centroiding accuracy improves as the centroiding gain increases, indicating that a higher gain produces a higher SNR in the star region, which subsequently enhances centroiding performance. Several scenarios were evaluated with varying background levels for the proposed sensor, and even under high background conditions (up to two-thirds of the signal swing), the system still achieves reliable centroiding accuracy at higher centroiding gains. However, this hardware-centric approach faces issues related to internal noise sources like operational transconductance amplifier (OTA) noise, readout noise, and reset noise.

As centroid precision directly affects the success of subsequent star identification, the following section discusses the identification algorithms that rely on these centroid estimates to match observed stars with entries in the onboard catalogue.

2.5.3 Star Identification

Star identification is a fundamental process in attitude determination, as it enables a star tracker to match detected stars within its field of view to the corresponding entries in an onboard star catalogue. The primary challenge arises under LIS conditions, where the system must identify stars without any prior attitude information (Nabi et al., 2021; Samaan, 2003; B. Wang et al., 2021). Once the initial orientation is determined, the tracker typically transitions into a recursive identification mode, which uses previous attitude estimates to substantially reduce both the search region and computation time.

A wide range of LIS identification algorithms has been developed, which can generally be categorized into pattern-recognition approaches and artificial intelligence techniques. Classical triangle-based algorithms are simple and attractive for low-cost trackers, although they become prone to ambiguous matches under noise (Nabi et al., 2021). More advanced formulations such as the Pyramid Algorithm improve robustness by incorporating four or more stars, achieving extremely low mismatch rates even in the presence of false stars (Mortari et al., 2004; Samaan, 2003). Alternatively, the planar triangle method introduces additional geometric descriptors, such as area and polar moment, enabling faster processing and higher success rates, albeit with the trade-off of significantly larger catalogue memory (Cole & Crassidis, 2006).

Research by Nabi et al. is dedicated to developing an improved triangular-based star pattern recognition algorithm specifically designed for low-cost star trackers, focusing on enhancing the efficiency and robustness of star identification (Nabi et al., 2021). The research is based on modifying the well-known triangular-based algorithm developed by Liebe (Liebe, 1993; Liebe & Joergensen, 1996). Figure 2.19 shows block diagram for the proposed method' prototype.

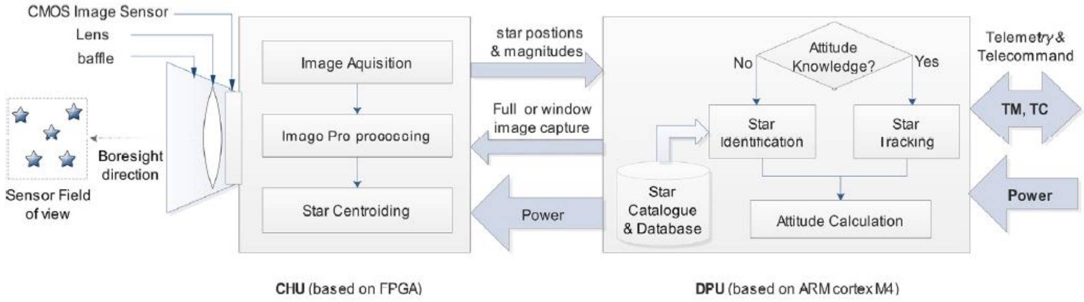

Figure 2.19: Block diagram of the star tracker prototype (Nabi et al., 2021)

The methods started with selecting the closest bright star to the centre of the FOV as the reference star (S1). This choice enhances robustness by making the reference star less susceptible to magnitude error and helps reduce the database size. The two closest stars to S1 (S2, S3) are selected without relying on magnitude information to increase the probability of them being in the FOV, especially when star density is low. Then, the algorithm uses a linear search technique to find a match between the observed star triplet and the guide star triplets in the database. This selection is illustrated in Figure 2.20.

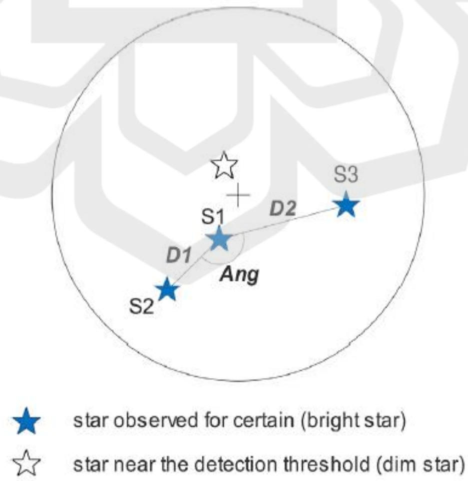

Figure 2.20: Feature extraction of a star triplet

The modifications resulted in an improvement in the overall identification rate compared to the original Liebe algorithm which is an improvement of 4% in ideal conditions and about 10% for the case of one missing star. However, the presence of a single false star on the triangular pattern can cause an identification failure, resulting in an identification rate of 87.9% when one false star is present in the FOV, which is comparable to the original Liebe algorithm (85.2%).

Another method to be discussed is the Pyramid Algorithm, focuses on developing faster and more accurate star sensors for spacecraft attitude determination through novel software and algorithmic techniques (Mortari et al., 2004; Samaan, 2003). Both Samaan (2003) and Mortari et al. (2004) address the problem of improving the speed and reliability of autonomous star sensors, although their focus and depth differ. Samaan's doctoral work adopts a system-level perspective, covering the full processing chain from sensor calibration and predictive centroiding to attitude acquisition and tracking. This comprehensive approach is important for practical implementation, particularly when dealing with hardware limitations and uncertainties in camera calibration. Meanwhile, Mortari et al. focus specifically on the LIS star identification problem and provide a rigorous analytical treatment of the Pyramid algorithm. In terms of efficiency, the two studies employ different strategies where Samaan improves computational performance by restricting centroid calculations to a small, predicted region of interest, while Mortari et al. rely on the k-vector technique to enable fast and searchless access to the star catalogue during identification. Additionally, in terms of limitations, Samaan notes difficulties in distinguishing between astigmatism tagging and image smear at high angular rates, and the analytical validation for higher-order star configurations was not fully established. Meanwhile, the Pyramid algorithm becomes less reliable when fewer than four stars are available, requiring additional consistency checks to avoid misidentification. Furthermore, both studies assume a uniform star distribution in their analytical models, which may not fully reflect real sky conditions. Overall, Samaan provides a practical system framework, while Mortari et al. contribute a mathematically robust identification method.

A method proposed a lost-in-space star identification algorithm utilizing a one-dimensional Convolutional Neural Network (1D CNN) (Wang et al., 2021). This algorithm converts star fields into rotation-invariant star patterns using a modified log-Polar mapping. The 1D CNN employs a global average pooling layer to substantially reduce the number of parameters, minimizing overfitting and allowing implementation on embedded systems. Figure 2.21(a) illustrates the result of the proposed algorithm in real image star detection and Figure 2.21(b) illustrates the identification rate.

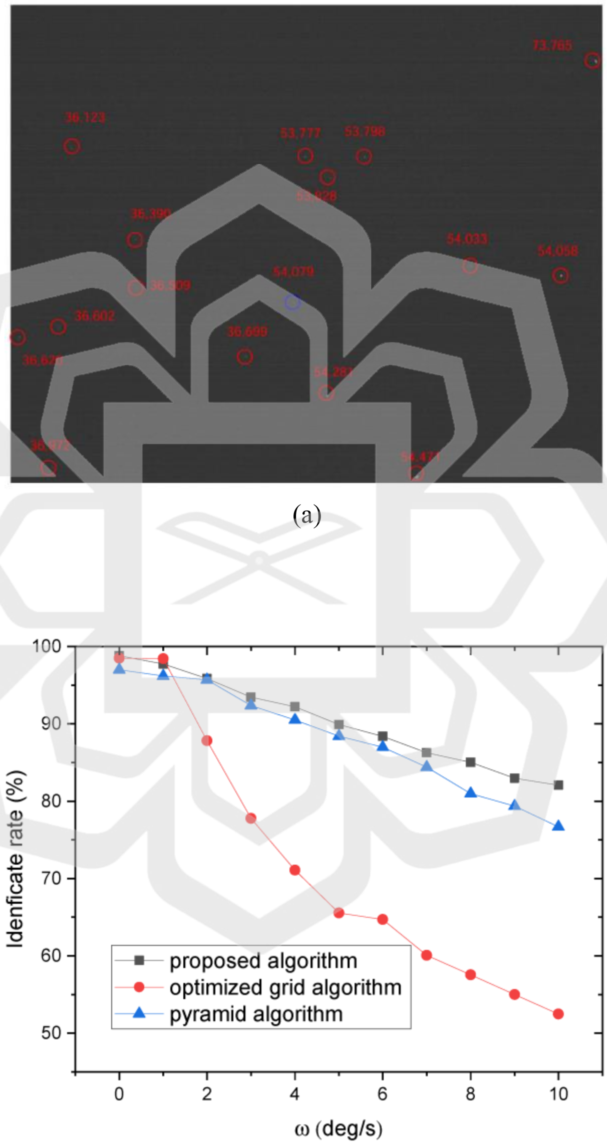

(a)

(b)

Figure 2.21: Result of the 1D CNN-based algorithm (a) in star image (b) graph of identification rate (Wang et al., 2021)

Experiments demonstrated high robustness across various noise conditions, achieving 98.1% accuracy with 5 pixels of position noise, and able to identify 1458 images correctly out of the 1472 images. Star 54,079 is selected as the reference star, and its identified neighbouring stars are highlighted in the figure.

To conclude, research on Pyramid Algorithm by Mortari et al. (2004) and Samaan (2003) offer strong analytical reliability but are vulnerable when fewer than four valid stars are available, while the triangular-based method exhibits limited tolerance to false stars due to its reliance on minimal star patterns. According to Wang et al., the neural network-based star identification algorithm demonstrates the highest overall robustness across diverse noise conditions (Wang et al., 2021). However, this robustness is empirical rather than analytical and depends strongly on training data quality and coverage. From a performance standpoint, Pyramid-based methods remain the most reliable when sufficient stars are detected and analytical guarantees are required, whereas the triangular-based method is best suited for low-cost or resource-constrained missions but is less appropriate for environments with high spike or radiation-induced noise. Research by Wang et al. can be considered the most robust identification approach under severe noise and dynamic conditions, although this algorithm achieves superior robustness, our research prioritizes a simpler yet stable and interpretable approach, focusing on robust image processing and centroiding rather than adopting a complex deep learning-based identification framework.

2.5.4 Celestial Coordinates

Celestial coordinates specifically Right Ascension (RA) and Declination (Dec) are angular measurements that locate stars on the celestial sphere, typically expressed in degrees or arcminutes, and they provide the reference framework used in star catalogues (NASA, n.d.-a; “The Hipparcos and Tycho Catalogues,” 2008). These coordinates allow star trackers to match the stars detected in an image with their true positions in the catalogue during attitude determination. Once a match is made, the spacecraft’s orientation is usually represented using quaternions, a four-element rotation model known for its numerical stability and freedom from gimbal lock, which is important for real-time space applications. Combined, celestial coordinates and quaternion representation form the basis of star-tracking systems by linking observed star vectors to catalogue data for accurate spacecraft orientation estimation (Wang et al., 2024).

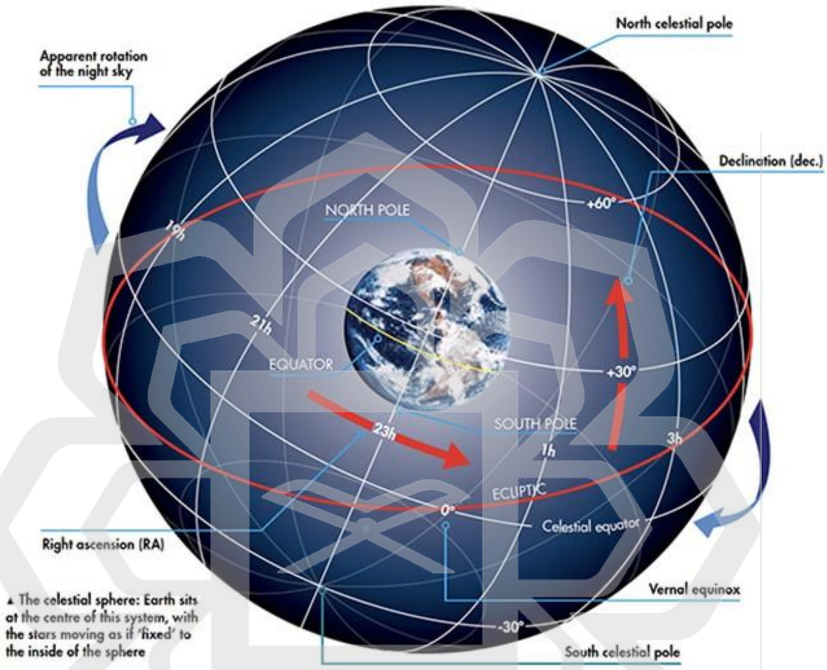

Figure 2.22: The celestial sphere and coordinate system (Paul Money, 2018)

Figure 2.22 shows the celestial sphere which is an imaginary construct used in astronomy to map the positions of stars as if they were projected around Earth. It illustrates the equatorial coordinate system, RA and Dec which functions similarly to longitude and latitude on Earth. The key reference points such as the North and South Celestial Poles, the Celestial Equator, and the Ecliptic, which traces the apparent path of the Sun across the sky also can be seen in the figure. For lunar surface navigation, the same RA/Dec coordinate system is used, as it is defined relative to distant stars and remains consistent regardless of whether the observer is on Earth or the Moon.

This study introduces a novel approach to enhance the robustness of the centroiding algorithm for implementation in lunar missions. The focus lies in improving both the thresholding method and the centroiding computation. The testing will be conducted using synthetic star images subjected to various noise models to determine the most suitable thresholding strategy. This approach supports the research objective of investigating the impact of lunar environmental conditions by evaluating how different noise types affect the accuracy and reliability of the centroiding algorithm.

Table 2.2: Summary of related works on star detection

Authors	Method	Approach	Contributions	Limitations
Karaparambil et al. (2023)	Sieve Search Algorithm (SSA)	Divides images into smaller sub-regions to analyse intensity distributions for Centre of Mass (COM)	Successfully follows the true centroid of double-star pairs even as they brighten. Offers better noise suppression	Susceptible to S-curve errors when dealing with small star spots. Inherently slower than simple COM
Wan et al. (2018)	Fast Gaussian Fitting (FGF)	Transforms nonlinear Gaussian fitting into a linear least-squares problem using log approximation	Achieves high accuracy levels while running 15x faster than traditional fitting methods. Eliminates S-curve errors	Performance refinement is dependent on the selection of SNR weights
Mortari et al. (2004)	Pyramid Algorithm	Utilizes the k-vector technique for fast and searchless access to the star catalogue	Provides mathematically robust identification with extremely low mismatch rates when four or more stars are present	Becomes unreliable and requires additional checks if fewer than four valid stars are available
Wang et al. (2021)	Neural Network (1D CNN)	Employs a 1D Convolutional Neural Network with modified log-Polar mapping for rotation-invariant patterns	Demonstrates the highest overall robustness across diverse noise conditions, reaching 98.1% accuracy under positional noise	Robustness is empirical rather than analytical and depends heavily on training data coverage
Nabi et al. (2021)	Improved Triangular Algorithm	Modifies Liebe's algorithm by selecting the closest bright star to the centre as the reference point	Improves identification rates by 10% when a star is missing compared to the original method	Highly vulnerable to identification failure if even a single false star is present in the pattern.
Mahi et al. (2024)	Dual-stage Algorithm	Uses object segmentation and centroid extraction to filter out non-stellar artifacts	Effectively eliminates large bright objects that interfere with the star tracker's field of view	Limited ability to detect stars that are heavily obscured by intense direct sunlight

2.6 SUMMARY

This chapter presents a detailed review of star camera technologies alongside the environmental constraints specific to the lunar surface. Active Pixel Sensor (APS) CMOS sensors are identified as the most suitable option for lunar missions due to their high level of integration, low power requirements, and improved resistance to radiation when compared to CCD sensors. The chapter also discusses optical challenges unique to the Moon, including strong regolith reflectance and rapid transitions between extreme illumination conditions, both of which contribute to a reduced SNR. Although the Sieve Search Algorithm (SSA) provides effective noise suppression, it suffers from higher computational cost and is prone to S-curve errors. Pyramid and Triangular algorithms show acceptable performance under ideal conditions but become unreliable when fewer than four stars are visible or when false star detections occur. Deep learning-based methods, such as one-dimensional CNNs, demonstrate robustness in noisy environments; however, their lack of transparency limits analytical interpretation. In contrast, the proposed method combines Point Spread Function (PSF) blurring with dynamic thresholding, allowing it to adapt to extreme lighting variations. As a result, it maintains stable star detection and achieves lower position errors in low SNR lunar conditions where conventional algorithms typically experience significant performance degradation.

CHAPTER 3

METHODOLOGY

3.1 OVERVIEW

In this chapter, a complete methodology for image preprocessing, thresholding, star centroid extraction and identification is presented. The primary objective is to develop an accurate and robust centroiding algorithm capable of detecting and localizing stars under different noise and illumination conditions. The proposed method is then evaluated using real star field images subjected to various simulated noise environments to assess its accuracy, reliability, and adaptability under low signal-to-noise ratio (SNR) conditions.

3.2 METHODOLOGY FRAMEWORK AND FLOWCHART

Figure 3.1 illustrates the overall flow of the proposed methodology implemented in this study. The process begins with investigation on lunar environment by implementing simulated noises, which is conducted to achieve Objective 1. In this stage, different types of noise and SNR conditions are introduced to emulate realistic space-based and lunar imaging disturbances affecting star sensor observations. Then the collection of star field images using the image sensor of a star camera is done followed by organizing the images into three separate datasets, each subjected to different testing conditions. Following this, the study proceeds with experiments on Dataset 1 and Dataset 2, which are designed to achieve Objective 2. Dataset 1 was used to test the centroiding performance of the proposed method under different types of noise and SNR conditions, which were designed to simulate realistic space-based imaging. Dataset 2 was used to assess the identification capability of the algorithm, focusing on how accurately it can detect and match real stars with their corresponding entries in the star catalogue under low-noise conditions. Meanwhile, Dataset 3 is used to achieve Objective 3, where a comparative analysis is carried out against existing centroiding methods. The performance is evaluated in terms of RMSE, Euclidean distance, FIR, and FDR. Using three separate datasets for different testing purposes helps ensure that each performance aspect such as centroiding accuracy, identification reliability, and comparative evaluation are assessed independently. Finally, the outcomes are recorded and summarized to conclude the methodology.

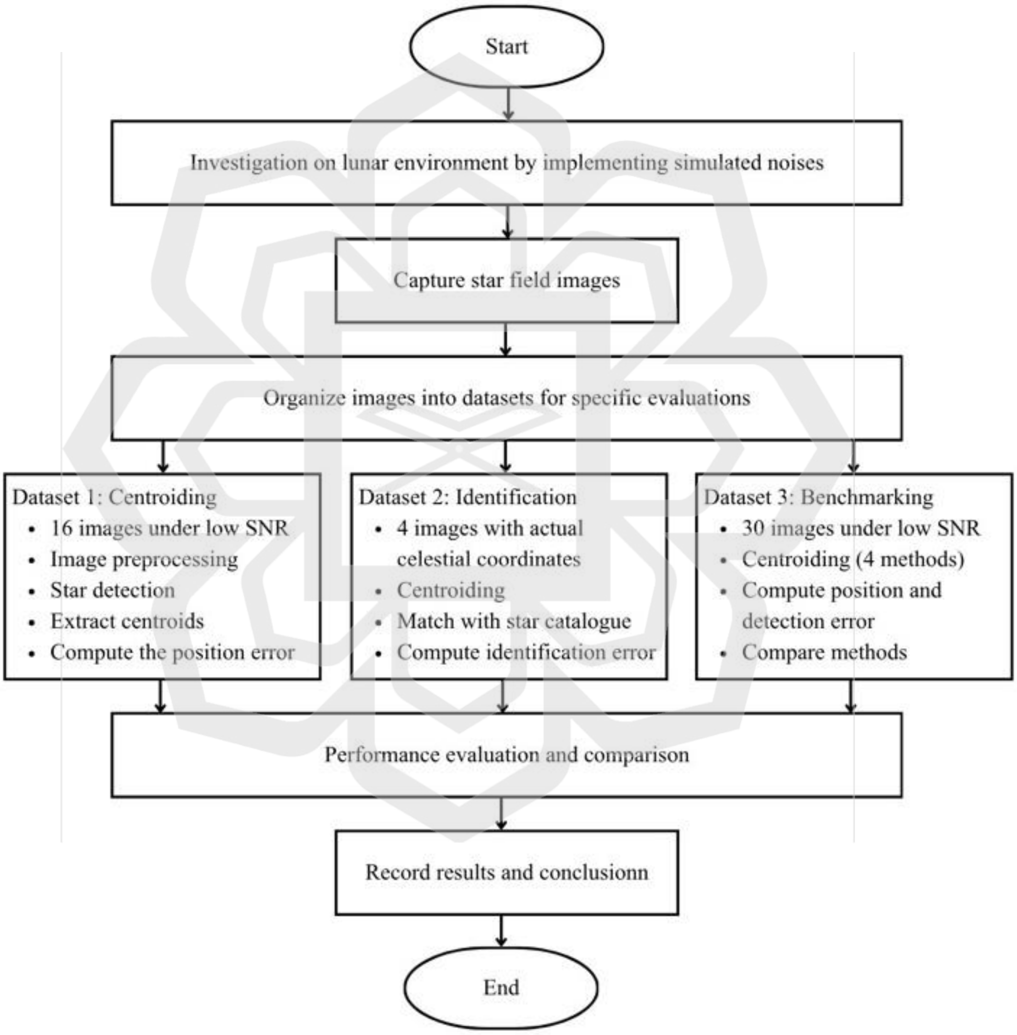

Figure 3.1: Overall flow of the proposed methodology

The proposed algorithm is divided into three main parts, which are the image preprocessing, centroid extraction and star identification. The overall proposed algorithm can be seen in Figure 3.2.

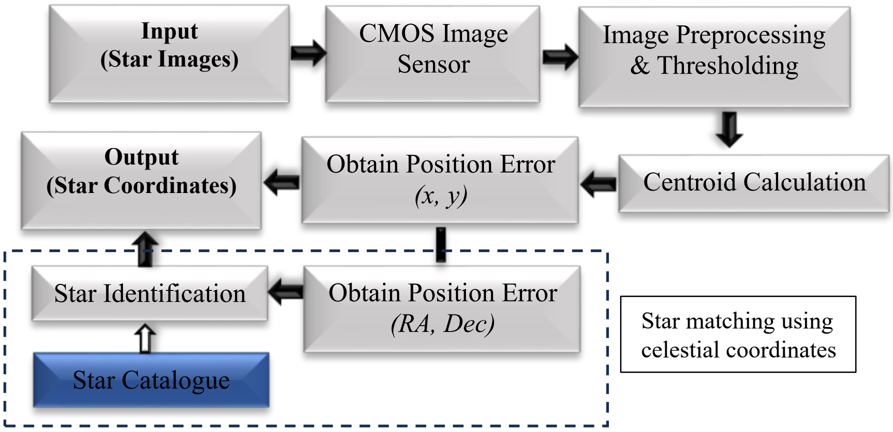

Figure 3.2: Block diagram of the overall proposed algorithm

The proposed methodology begins with the input of a star field image into the system, where a CMOS image sensor captures the image for further processing. The captured image is then processed to separate the bright star blobs from the dark background, allowing the system to isolate potential star regions. Once the star blobs are obtained, the centroid of each blob is computed to obtain its precise pixel coordinates. These coordinates are subsequently transformed into celestial coordinates for comparison with an established star catalogue. By matching the detected coordinates with the catalogue, the system determines the corresponding star identities.

3.3 REAL STAR IMAGES UNDER DIFFERENT NOISE ENVIRONMENT

The star images were processed under four different noise conditions: Poisson, Gaussian, salt-and-pepper, speckle, as well as an additional solar reflection model for realism. Poisson noise and Gaussian noise were applied to represent random fluctuations that are commonly observed in space-based imaging systems. Salt and pepper noise was introduced to simulate sparse but high-contrast disruptions, resembling faulty pixels or cosmic ray strikes. Speckle noise was used to replicate multiplicative noise, typically arising from interference or scattering effects in imaging sensors. Figure 3.3(a)-(e) illustrates the types of noise added to the images.

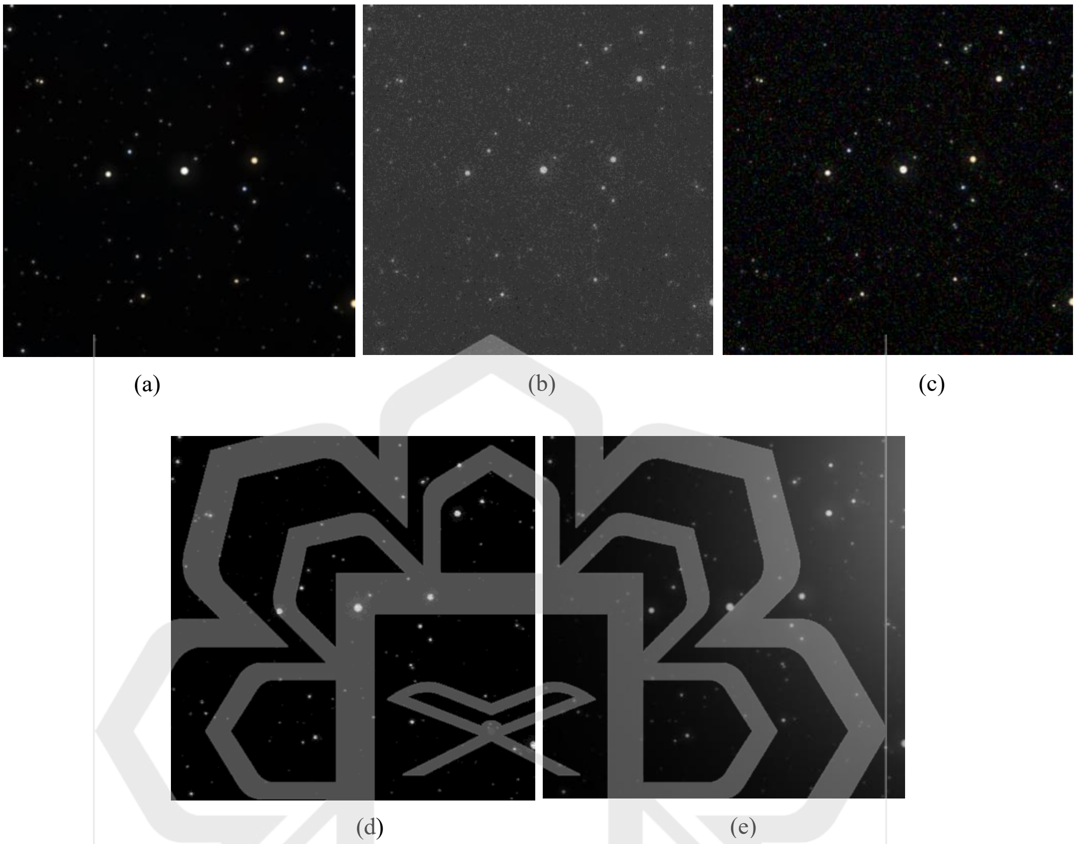

Figure 3.3: Noise samples (a) clean image, (b) Gaussian and Poisson noise, (c) salt-and-pepper noise, (d) speckle noise, and (e) sunlight glare

The inclusion of various noise models in the star images is detailed in the next sections.

3.3.1 Gaussian and Poisson Noise

In a work, the authors present a new solution for handling Gaussian-Poisson noise mixture (Ghazdali et al., 2024). Hence, the combination of Gaussian noise and Poisson will be added in the star images. Gaussian noise models electronic sensor noise such as thermal noise and read noise. The parameters used are the mean, $\mu = 0$, variance, $\sigma^2 = 0.15$. For each pixel $I(x, y)$:

$$I_{gaussian}(x, y) = I(x, y) + n_{gaussian}(x, y) \tag{3.1}$$

Where the noise term is drawn from Gaussian (normal) distribution:

$$n_{gaussian}(x, y) \sim N(\mu, \sigma^2) \tag{3.2}$$

So the noise spreads around zero, with strength controlled by the variance.

Next is combining Poisson noise into Gaussian noise image. Poisson noise simulates photon counts. For each pixel:

$$I_{poisson}(x, y) \sim Poisson(I_{gaussian}(x, y)) \tag{3.3}$$

Meaning that if a pixel is bright, the higher expected photon count and the more noise. If a pixel is dark, the fewer photons and the less noise.

3.3.2 Salt and Pepper Noise

Salt and pepper noise is added after converting the input image to grayscale. A set number of pixel locations is then randomly selected within the image dimensions using a random number generator. The chosen pixels are assigned intensity values of either 0 (pepper) or 255 (salt), producing the characteristic black-and-white impulse noise. The resulting noisy image is then saved. The parameters used for this noise model is the probability of a pixel being corrupted which called as noise density, $d = 0.05$. Meaning that the value 0.05 is 5% of the pixels in the image will have their original values replaced by either the maximum or minimum intensity value. The summary of the substitution is shown in Table 3.1.

Table 3.1: Salt and pepper noise substitution

Pixel Type	Action	New Pixel Value	Effect on Image
Original (95%)	Retains original value.	Original intensity	No change.
Salt (2.5%)	Replaced with **1.0**.	Maximum intensity (White)	Create bright, isolated spots.
Pepper (2.5%)	Replaced with **0.0**.	Minimum intensity (Black)	Create dark, isolated spots.

Since the images are black and white, which ranges from 0.0 (black) to 1.0 (white), the corrupted pixels are set to these limits.

3.3.3 Speckle Noise

A speckle noise matrix generated where the pixel values are centred around mean, $\mu = 1.0$, and spread out by a variance, $\sigma^2 = 0.15$. Unlike Gaussian noise (which is added), speckle noise is generated by multiplying the clean image I_{clean} by a noise mask M_{noise}:

$$I_{speckle}(x, y) = I_{clean}(x, y) \times M_{noise}(x, y) \tag{3.4}$$

Where $I_{speckle}$ is the final corrupted image, $I(x, y)$ is the original clean image and M_{noise} is the noise mask, where each pixel is an independent random variable drawn from a specific distribution.

3.3.4 Sunlight Glare

The simulation of solar reflection (glare) is achieved not through the introduction of random noise, but by the deterministic addition of a large, high-intensity, structured artifact onto the clean image. This glare is mathematically modelled using a two-dimensional Gaussian profile, often referred to as a Gaussian function or bell curve in 2D, which defines a smooth, circular patch of light:

$$glare = \exp\left(-\frac{(X - X_{centre})^2 + (Y - Y_{centre})^2}{2 \times r^2}\right) \tag{3.5}$$

The term $(X - X_{centre})^2 + (Y - Y_{centre})^2$ calculates the squared distance of every pixel from the defined centre point. The result is then used as the exponent of e. This creates a peak at the centre (where distance is zero, $e^0 = 1$) that smoothly and rapidly decays as the distance increases. This shape mimics the soft, circular fall-off of actual lens flare or solar reflection. The $radius, r = 200{\sim}600$ parameter controls the spread of this patch. A large radius value, like 600, makes the glare very broad and diffuse across the image.

3.4 IMAGE PREPROCESSING AND CENTROID EXTRACTION

Preprocessing the star images is a crucial step in the centroiding process. It ensures that the system can accurately detect actual stars including faint ones, while minimizing noise and other distortions. This section not only presents the centroid extraction steps but also introduces the simulated noise models that will be applied during testing to replicate the lunar environment.

3.4.1 Point-Spread-Function Model for Image Blurring

In this research, the Point Spread Function (PSF) is used to simulate the optical blur introduced by a star camera system (Liaudat et al., 2023; B. Lin et al., 2024). Since real star images inherently contain some degree of blurring due to the optical and sensor characteristics of the camera, a Gaussian PSF is applied to synthetic star images to replicate this behaviour. The Gaussian PSF approximates the way a point light source is spread out over several pixels on a detector. The Gaussian PSF model is defined as:

$$G(x,y) = \frac{1}{2\pi\sigma^2} exp\left(-\frac{x^2+y^2}{2\sigma^2}\right) \tag{3.6}$$

where σ is the standard deviation of the Gaussian function, which controls the amount of blur. The Gaussian PSF determines the area over which the function is applied. The PSF is applied to the image, $I(x,y)$, through convolution to simulate the blurred appearance of a star:

$$I_{blurred}(x,y) = I(x,y) * G(x,y) \tag{3.7}$$

The kernel size of the Gaussian PSF should be sufficient to encompass the majority of the Gaussian's energy (Moo K. Chung, 2007). For $\sigma = 1.5$ testing, a standard deviation of $\sigma = 1.5$ is used with 7×7. However, for a more realistic simulation, especially for star tracker applications where stars may appear larger and more diffused, higher values of $\sigma = 2.0$ to 2.5 can be used as well. These larger kernels such as 11×11 or 13×13 to properly represent the PSF.

Figure 3.4 illustrates the 2D Gaussian kernel as a bell-shaped surface. The graph shows the smooth, symmetrical decay of intensity from the centre outward, which is characteristic of the Gaussian function. This profile mimics how light from a distant star would spread when captured by a real optical system.

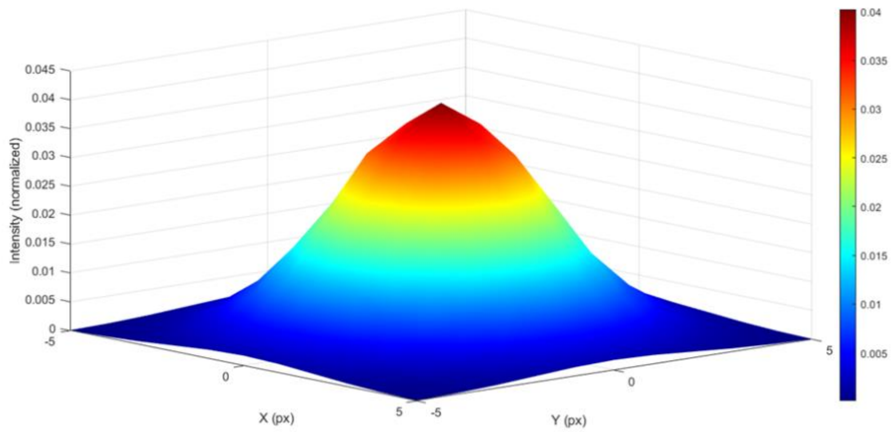

Figure 3.4: 2D Gaussian kernel as a bell-shaped surface with $\sigma = 2.0$, $kernel\ size = 11 \times 11$

The shape of the bell curve is directly influenced by the value of the standard deviation σ; a smaller σ results in a sharper and narrower peak, concentrating most of the intensity at the centre, while a larger σ produces a broader and flatter peak, spreading the intensity over a wider area. In the case of a standard deviation $\sigma = 2.0$, the kernel captures a wide enough region to realistically approximate the PSF of most moderate-resolution star trackers.

3.4.2 Median Filtering for Background Removal

To enhance the quality of star images prior to centroid detection, a median filter model is applied to reduce background noise and isolate potential star regions (Hung et al., 2014). The median filter operates by sliding a window across the image and, at each position, replacing the central pixel with the median value of the pixel and its surrounding neighbours within the window (Patrice, 2016).

As an example, consider 3×3 pixel:

$$\begin{bmatrix} 34 & 36 & 40 \\ 38 & 255 & 41 \\ 35 & 39 & 37 \end{bmatrix}$$

The sorted values in this window are:

$$\{34, 35, 36, 37, 38, 39, 40, 41, 255\}$$

The median value is 38, which replaces the centre pixel. The converted image becomes:

$$\begin{bmatrix} 34 & 36 & 40 \\ 38 & 38 & 41 \\ 35 & 39 & 37 \end{bmatrix}$$

This process is repeated across the entire image, providing effective suppression of impulse noise and preserving edges, making it suitable for star field images with scattered bright blobs.

3.4.3 Binary Segmentation with Thresholding Method

After denoising, the filtered image is binarized using global thresholding T to segment potential star regions from the background. The threshold factor is a multiplier that determines the final cutoff value (T):

$$T = \alpha \cdot \max(I) \tag{3.8}$$

I is the intensity and α is a threshold factor, typically between 0 to 1, which determines the sensitivity of the segmentation. This factor dictates that the cutoff value T for distinguishing foreground from background will be set around 20% - 40% (0.2 – 0.4) of the absolute brightest intensity found in the image.

Several threshold factors ranging from 0.2 to 0.4 were evaluated experimentally to determine the most suitable value for star segmentation under simulated low SNR conditions. The testing was performed by comparing the resulting star detection performance in terms of centroid accuracy, false detections, and segmentation quality.

Based on the evaluation, a threshold factor of 30% (0.3) is selected, which means, any pixel with an intensity greater than 30% of the image's maximum intensity is classified as foreground (set to 1, white). All other pixels with an intensity less than or equal to 30% of the maximum are classified as background (set to 0, black). The maximum intensity value, $\max(I)$, in the filtered image represents the brightest pixel. Multiplying it by α sets a dynamic threshold that scales with image brightness.

$$B(x,y) = \begin{cases} 1, & if\ I(x,y) > T \\ 0, & otherwise \end{cases} \tag{3.9}$$

$I(x,y)$ is the intensity of the pixel at position (x,y) in the filtered grayscale image. $B(x,y)$ is the resulting binary image, where a value of 1 indicates potential star pixel (foreground) and a value of 0 indicates background. This method produces a binary image that highlights high-intensity regions that presumed to be star blobs while suppressing the lower-intensity background. The use of a dynamic threshold based on $\max(I)$ helps the algorithm adapt to different lighting conditions or brightness levels in the star images.

3.4.4 Star Centroid Extraction

For each labelled star blob, the centroid is calculated to estimate its centre. In real star images, the brightness of a star is not uniformly distributed, it typically forms a peak at the centre and gradually decreases outward. To account for this brightness variation and achieve higher centroiding accuracy, the centroid can be calculated using an intensity-weighted approach also known as the centre of mass method. This method utilizes the original grayscale (or denoised) image, where each pixel's contribution to the centroid is proportional to its intensity, rather than treating all foreground pixels equally (Qian et al., 2016). The intensity-weighted centroid is given by:

$$x_c = \frac{\sum_{x,y} x \cdot I(x,y) \cdot w(x,y)}{\sum_{x,y} I(x,y) \cdot w(x,y)}, y_c = \frac{\sum_{x,y} y \cdot I(x,y) \cdot w(x,y)}{\sum_{x,y} I(x,y) \cdot w(x,y)} \tag{3.10}$$

$I(x, y)$ is the pixel intensity (brightness) at location (x, y), and the summation is performed over all pixels in the labelled region.

Algorithm 1 describes the preprocessing and centroid extraction process of the proposed method.

Algorithm 1 Star Detection and Centroid Extraction

Input: Grayscale star image $\boldsymbol{I}$

Output: Star centroid coordinates $\{(x_j, y_j)\}_{i=1}^{N}$

1. Preprocessing

  Apply Gaussian blur using PSF model

  Apply median filter to suppress background noise

2. Thresholding

  Compute maximum intensity I_{max}

  Set dynamic threshold $T = \alpha \cdot I_{max}$

  for all pixels (x, y) in I **do**

    if $I(x, y) \geq T$ then

      $B(x, y) \leftarrow \mathbf{1}$ ▷ Foreground

    else

      $B(x, y) \leftarrow \mathbf{0}$ ▷ Background

    end **if**

  end **for**

3. Centroid Extraction (Proposed)

  Label star blobs in binary image $B(x, y)$

  for all blobs i **do**

    Extract pixel set $\{(x_j, y_j)\}$ and intensities $I(x_j, y_j)$

    Compute intensity-weighted centroid:

$$x_c = \frac{\sum_{x,y} x \cdot I(x,y) \cdot w(x,y)}{\sum_{x,y} I(x,y) \cdot w(x,y)}, \qquad y_c = \frac{\sum_{x,y} y \cdot I(x,y) \cdot w(x,y)}{\sum_{x,y} I(x,y) \cdot w(x,y)},$$

  end **for**

4. Error Computation (Per Image)

for each detected star i do
    Compute Euclidean distance, $d = \sqrt{(x_i - x_i^{GT})^2 + (y_i - y_i^{GT})^2}$
end for
Compute average Euclidean distance, $\bar{d} = \frac{1}{N}\sum_{i=1}^{N} d_i$
Compute RMSE, $RMSE = \sqrt{\frac{1}{N}\sum_{i=1}^{N} {d_i}^2}$
return $\{(x_j, y_j)\}_{i=1}^{N}$, $\bar{d}$, RMSE

3.5 STAR IDENTIFICATION

To validate the accuracy of star detection and centroiding, the detected stars are cross-referenced with a known star catalogue. The validation process begins by referencing the existing star catalogue, which contains precise Right Ascension (RA) and Declination (Dec) values for a wide range of stars (NASA, n.d.-a). A subset of this catalogue is loaded into the system, providing known positions for comparison. To establish a geometric relationship between the detected star positions in the image and their actual coordinates, at least three reference stars are manually selected from the processed image. Their corresponding pixel coordinates are paired with known RA/Dec values obtained from the catalogue.

An affine transformation is computed using these reference pairs (House & C. Keyser, 2020). This transformation accounts for translation, rotation, and scaling between the image and the celestial sphere, allowing the mapping of all detected centroids from pixel coordinates to sky coordinates. Equation (6) represent the transformation using homogeneous coordinates:

$$\vec{p}' = M\vec{p}$$

$$\begin{pmatrix} x' \\ y' \\ 1 \end{pmatrix} = \begin{pmatrix} a & b & c \\ d & e & f \\ 0 & 0 & 1 \end{pmatrix} \begin{pmatrix} x \\ y \\ 1 \end{pmatrix} \tag{3.11}$$

$\vec{p}$ is point in the homogeneous coordinates, M is the affine transformation matrix and $\vec{p}'$ is the transformed point.

After the transformation, the RA/Dec of all stars detected in the image are determined. These coordinates are then compared with the Hipparcos catalogue to identify and validate the stars ("The Hipparcos and Tycho Catalogues," 2008). The nearest Hipparcos star number (HIP) in the catalogue is then assigned as the matching star for each detected object. This approach provides a one-to-one mapping and enables verification of detection accuracy. By matching observed star centroids with known catalogue entries, this method not only confirms the identity of stars in the image but also facilitates attitude determination, as the known positions of matched stars can be used to compute the orientation of the imaging platform. Algorithm 2 outlines the star identification stage, where the extracted centroids are matched with the reference star catalogue.

Algorithm 2 Star Identification Using Hipparcos Catalogue

Input: Centroid coordinates (x_j, y_j)
Input: Star catalogue in celestial coordinate
Input: At least three reference stars with pixel coordinates (x_r, y_r) and celestial coordinates (α_r, δ_r)
Output: Identified star IDs and matched celestial coordinates

Load C from hipparcos-voidmain.csv
Read pixel coordinates and corresponding RA/Dec values for reference stars
Compute affine transformation

$$T = fitgeotrans\big((x_r, y_r), (\alpha_r, \delta_r), 'affine'\big)$$

Apply transformation: $(\alpha_i, \delta_i) = T(x_i, y_i)$ for all detected centroids
Set matching tolerance $\epsilon = 0.1°$
for each star i in detected centroids **do**
    Compute distance $d_j = \sqrt{\left(C_{RA_j} - \alpha_i\right)^2 + \left(C_{Dec_j} - \delta_i\right)^2}$ for all catalogue stars j
    Find minimum distance $d_{min} = \min(d_j)$ and corresponding index $j*$
    if $d_{min} \leq \epsilon$ **then**
        Assign matched ID: Assign $HIP_i = C_{HIP}(j*)$
        Store angular distance error d_{min}
        Increment $N_{match} = N_{match} + 1$
    else
        No valid match: $HIP_i = 0$

Increment $N_{false} = N_{false} + 1$
end if
end for
Compute FIR

$$FIR = \frac{N_{false}}{N_{match} + N_{false}} \times 100\%$$

return identified star IDs, matched coordinates, angular distance error and FIR

3.6 PERFORMANCE VALIDATION

To assess the effectiveness of the proposed approach, a comparative study is carried out using Dataset 3, which contains 30 star field images acquired under different low SNR conditions. The aim of this evaluation is to compare the proposed method with three commonly used centroiding techniques: COM, Gaussian Fitting, and the Sieve Search Algorithm (SSA). All algorithms are applied to the same set of degraded images to ensure a fair comparison and to provide a reliable indication of each method's ability to accurately locate true stars while rejecting noise and false detections. The overall procedure for this comparative analysis is summarized in Algorithm 3.

Algorithm 3 Performance Validation Through Benchmarking

Input: 30 star field images, I_k
Input: Ground truth star centroid positions
Output: Comparative performance metrics (RMSE, Euclidean Distance, FDR)

Initialize error storage arrays for all methods: Proposed, COM, Gaussian Fitting, SSA
for each image I_k in Dataset 3 **do**
    Run Proposed Method on I_k
    Run Centre of Mass (COM) algorithm on I_k
    Run Gaussian Fitting algorithm on I_k
    Run Sieve Search Algorithm (SSA) on I_k
    for each method $m \in \{Proposed, COM, Gaussian\ Fitting, SSA\}$ **do**
        for each detected star i in method m **do**
            Compute Euclidean distance, $d = \sqrt{(x_i - x_i^{GT})^2 + (y_i - y_i^{GT})^2}$
            Store centroid error d_i
            if detected star has no corresponding ground truth then

Count as false detection

end if

end for

Compute RMSE for image I_k using $RMSE_k = \sqrt{\frac{1}{N}\sum_{i=1}^{N} {d_i}^2}$

end for

end for

Compute average RMSE, mean Euclidean distance, and false detection rate for each method

return comparative summary table

3.7 EVALUATION METRICS FOR CENTROIDING ACCURACY

In order to evaluate the accuracy and reliability of the proposed star detection and identification methods, a positional error analysis was conducted. This analysis considers two types of errors: Euclidean distance in the image plane (pixel space) and angular distance in the celestial coordinate system (sky space). Both metrics are crucial to assess the quality of detection and identification under simulated and real space conditions.

3.7.1 Euclidean Distance Error (for Pixel Coordinates)

In the image plane, the ground truth pixel coordinates of each star are known. Therefore, the position error of each star will be measured (Ma et al., 2024). The accuracy of the centroiding method is evaluated using Euclidean distance error, which calculates the straight-line distance between the detected centroid and the true position in pixel space (Danielsson, 1980). The formula used is:

$$d = \sqrt{\left(x_i - x_i^{GT}\right)^2 + \left(y_i - y_i^{GT}\right)^2} \tag{3.12}$$

Figure 3.5 visualizes the position errors in pixels, shown in three different conditions. In real star observations, an error of 1-5 pixels is usually insignificant and does not affect star detection, centroiding, or identification, as the stars' brightness and light spread around the centre often mask small deviations.

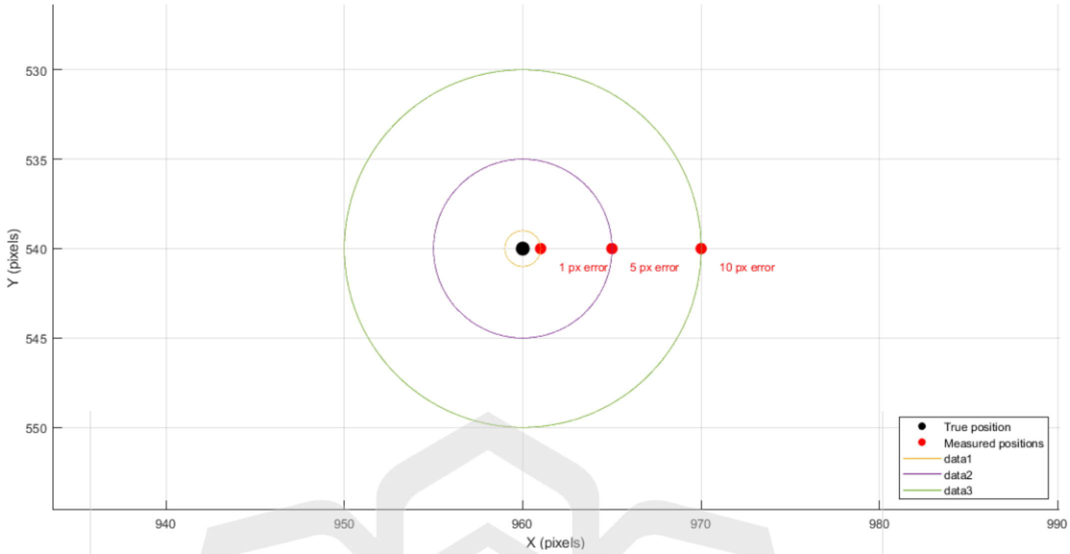

Figure 3.5: Pixel error visualisation: 1, 5 and 10 pixels

3.7.2 Angular Distance Error (for Celestial Coordinates)

In the case of real sky images, the pixel coordinates of detected stars are transformed into celestial coordinates (RA/Dec) using affine transformations. To validate the accuracy of these transformed positions, the angular distance error is calculated by comparing the estimated celestial coordinates to reference data from Hipparcos star catalogue ("The Hipparcos and Tycho Catalogues," 2008). The angular distance between two stars on the celestial sphere is computed using the following formula:

$$\cos\theta = \sin(\delta_1)\sin(\delta_2) + \cos(\delta_1)\cos(\delta_2)\cos(\alpha_1 - \alpha_2) \tag{3.13}$$

$$\theta = \cos^{-1}(\cos(\theta))$$

where α and δ denote RA and Dec. The resulting angle θ indicates the separation in degrees (angular distance).

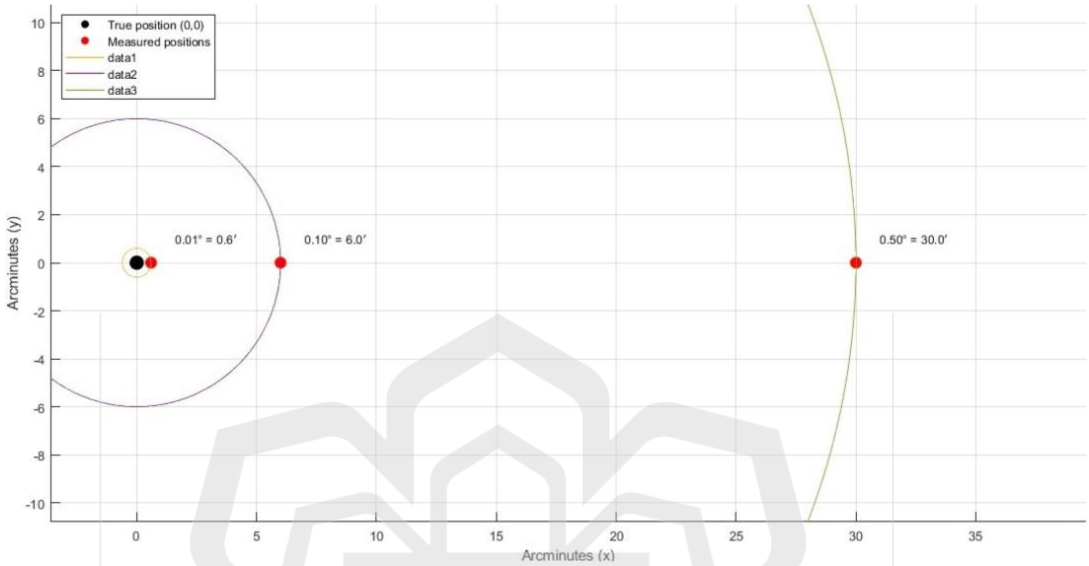

Figure 3.6: Angular distance error visualisation: 0.01°, 0.1° and 0.5°

Figure 3.6 visualizes the angular distance error in arcminutes. As shown, smaller angular deviations such as 0.01° (0.6′) and 0.1° (6.0′) correspond to relatively minimal position errors, while larger deviations like 0.5° (30.0′) indicate significant misalignment from the true position. Therefore, in this study, an angular error threshold of 0.01° is considered acceptable for identifying a specific star from the Hipparcos catalogue. The corresponding validation and testing process are detailed in Section 4.2.

3.7.3 Mean Squared Error (MSE) and Root Mean Squared Error (RMSE)

To summarize the overall error performance for the synthetic star images, MSE and RMSE are used. These metrics offer a statistical overview of error magnitude across all detected stars (Akshita Chugh, 2020):

$$MSE = \frac{1}{N}\sum_{i=1}^{N}(y_i - \hat{y})^2 \tag{3.14}$$

$$RMSE = \sqrt{MSE} = \sqrt{\frac{1}{N}\sum_{i=1}^{N}(y_i - \hat{y})^2} \tag{3.15}$$

Where e_i is either the Euclidean error (for synthetic images) or angular error (for real sky images), and N is the number of stars. RMSE provides an interpretable value in the same unit as the original data (pixels or degrees) and is widely used to compare centroiding performance across methods.

3.7.4 Identification and Detection Rate

In evaluating the performance of a centroiding and star identification algorithm, it is essential to consider not only the precision of the centroid estimation but also the reliability of the detection and recognition stages. Two commonly used performance indicators are the False Detection Rate (FDR) and the False Identification Rate (FIR).

The False Detection Rate (FDR) quantifies the proportion of incorrectly detected stars, instances where non-stellar objects such as noise, hot pixels, or image artefacts are mistakenly classified as stars (Mahi & Karoui, 2019). A higher FDR indicates that the algorithm is overly sensitive to noise, while a lower FDR suggests a more reliable detection process. The FDR can be expressed as:

$$FDR = \frac{N_{false}}{N_{detected}} \times 100\% \tag{3.16}$$

where N_{false} represents the number of false detections and $N_{detected}$ denotes the total number of detected stars.

On the other hand, the False Identification Rate (FIR) measures the percentage of stars that have been detected but incorrectly matched to the reference catalogue (Y. Li et al., 2022). In other words, FIR reflects the accuracy of the star matching or identification stage rather than the detection stage. This metric is particularly important in star tracker applications, where accurate identification directly affects attitude determination. The FIR is defined as:

$$FIR = \frac{N_{false}}{N_{match} + N_{false}} \times 100\% \tag{3.17}$$

where $N_{misidentified}$ is the number of stars assigned incorrect identities and $N_{matched}$ is the total number of successfully matched stars.

While both FDR and FIR relate to detection performance, they assess different aspects of the algorithm's reliability. FDR focuses on the validity of detected stars, whereas FIR evaluates the accuracy of star identification. These metrics provide a comprehensive assessment of the algorithm's effectiveness in distinguishing true celestial objects from noise and correctly associating them with catalogue entries (Liu et al., 2021; Yuan et al., 2025).

3.8 SUMMARY

This chapter details the development of a robust image processing pipeline for star detection, which begins with preprocessing using a Gaussian Point Spread Function (PSF) to simulate optical blur and a median filter for background noise removal. A global thresholding method, typically set at 30% of the image's maximum intensity, is used for binary segmentation to adapt to varying brightness levels. The median filter suppresses impulse noise by applying a sliding window across the image and replacing each central pixel with the median of its neighbouring values. This approach is effective at cleaning background noise while preserving the edges of star blobs. For sub-pixel accuracy, the algorithm utilizes an intensity-weighted COM approach to compute star centroids. To validate these results, the detected stars are transformed into celestial coordinates via affine transformations and matched against the Hipparcos star catalogue. Accuracy is measured using statistical metrics such as position error which is the Euclidean distance between the detected stars and the ground truth for both pixel coordinates and celestial coordinates, RMSE and identification rate.

CHAPTER 4

RESULT AND DISCUSSION

4.1 OVERVIEW

This chapter presents the experimental results and performance evaluation of the proposed centroiding algorithm. The experiments were conducted using three different datasets as described in Figure 3.1, each serving a distinct testing objective: to evaluate centroiding accuracy, assess celestial coordinate matching ability, and compare performance with existing methods. The analysis begins with the visualization of the detected stars and centroid outputs to demonstrate the algorithm's precision in identifying stellar positions. Quantitative assessments were then carried out using performance metrics such as RMSE, Euclidean distance, and false detection rate. The comparative results between the Centre of Mass (COM), Gaussian Fitting and Sieve Search Algorithm (SSA) verify the proposed method's effectiveness in enhancing the star centroiding performance.

4.2 EXPERIMENTAL SETUP

This section describes the experimental setup used to evaluate the proposed centroiding algorithm, including the hardware configuration and characteristics of the captured star field images.

4.2.1 Camera Baseline

As for the camera setup, we selected ArduCAM 2 MP OV2311 global shutter monochrome camera module, a MIPI CSI-2 compatible camera designed for Raspberry

Pi platforms. This module operates in monochrome (NoIR) mode, which is advantageous for star sensor applications as it avoids colour array and improves sensitivity under low-light conditions. Additionally, this module was selected as the imaging device for the setup because of its compact design, reduce the system power requirements and which make it practical for controlled indoor data collection. The module specifications are summarised in Table 4.1.

Table 4.1: Camera module specifications

Product	Global Shutter OV2311 Mono Camera Modules Pivariety (NoIR)
Sensor	Monochrome Global Shutter OV2311
Pixel Size	3 µm x 3 µm
Active Array Size	1600 × 1300
Optical Size	1/2.9 inch
Frame Rates	1600 × 1300@30fps, 1600 × 1080@30fps, 1280 × 720@60fps
Input clock frequency	6~27 MHz
Max S/N ratio	37.4 dB
Dynamic range	68 dB
IR Sensitive	No IR filter, sensitive to IR
FOV on 1/4” RPi Camera	83° (H)
Lens Mount	M12
Output interface	2-lane MIPI
Output formats	RAW 8/10 bit
Minimum exposure time	1 row period (11.3us at the resolution of 1600x1300 on Raspberry Pi)

The camera module was interfaced with a Raspberry Pi 5 single-board computer, which served as the host processing unit. The Raspberry Pi 5 was connected to a display monitor, USB keyboard, and mouse to facilitate system setup, software configuration, and image capture control. Physically, the OV2311 camera module was connected to the CSI-2 camera port on the Raspberry Pi 5 using the supplied MIPI ribbon cable, ensuring correct orientation and firm seating of the connector to maintain signal integrity. The integration of Raspberry Pi 5 and ArduCAM diagram is shown in Figure 4.1.

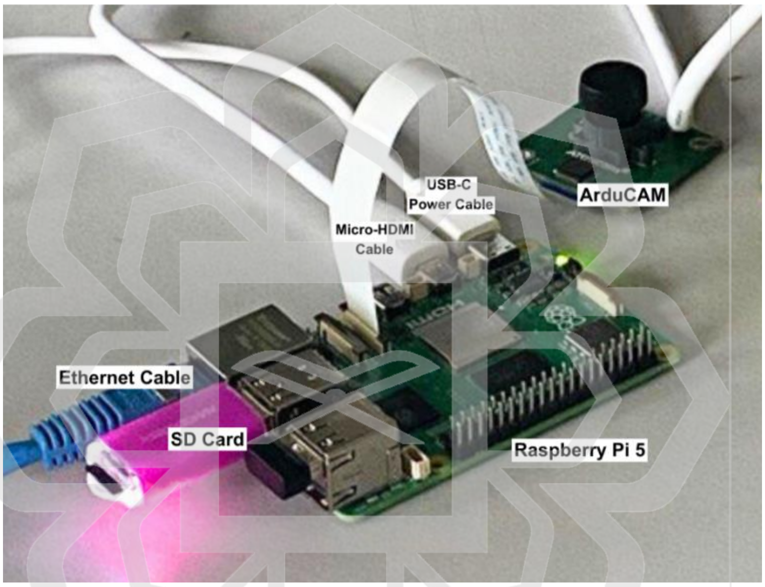

Figure 4.1: Prototype camera diagram

The Raspberry Pi was initially flashed with the Raspberry Pi OS (Bookworm) to activate the ArduCAM PiVariety driver interface, allowing the operating system to recognize and communicate with the OV2311 sensor. To simulate an orbital environment, a custom-made aluminium profile jig was constructed to provide a rigid, light-shielded framework for the hardware. Within this setup, the camera is positioned facing a monitor, which serves as the primary visual source by displaying the Stellarium star field images. This setup allows the system to capture realistic star patterns while maintaining full control of the ground-testing environment.

(a) (b)

Figure 4.2: Prototype camera experimental setup

Once captured, the raw or processed images were transferred and logged for subsequent preprocessing and centroiding algorithm evaluation. The image will then be added with noise and visual disturbances to degrade the image quality and imitate the actual space and lunar environment, as mentioned in Section 3.3. This ensures that the proposed method is evaluated under different levels of distortion similar to real-world conditions. These images then distributed into different datasets for the evaluation of the proposed algorithm. Each dataset corresponds to a different testing objective, allowing the assessment of centroiding performance across various noise models and illumination conditions.

4.2.2 Star Field Images Characterisation

As mentioned in Section 3.2, the experiment makes use of three datasets, each designed to evaluate a different aspect of the proposed method. Dataset 1 consists of 16 images and is used to assess the detection and centroiding accuracy of the algorithm. The analysis for this dataset will be presented in Section 4.3. Dataset 2 consists of 4 images with known celestial coordinates and is used to evaluate the actual star identification capability, which will be discussed in Section 4.4. Dataset 3 contains 20 images and is dedicated to comparing the detection and centroiding performance of the proposed algorithm with other existing methods; the results from this part will be explained in Section 4.5.

All images in the three datasets were assigned different noise environments, and their corresponding SNR values were recorded to characterise the severity of image degradation. This allows the evaluation to cover a range of realistic imaging conditions, from mild noise to heavily degraded scenarios. The clean star image used as the baseline for all simulations is shown in Figure 4.3.

Figure 4.3: Sample of star image

The image has a 16:9 landscape layout and is an HD image with a resolution of 1920×1080 pixels at 300 dpi. This consistent image specification is maintained across all evaluations to ensure fair comparison and to obtain clearer, more reliable results.

4.3 THE PROPOSED ALGORITHM UNDER NOISY ENVIRONMENT

This section presents the accuracy analysis of the proposed star centroiding algorithm under varying noise conditions and SNR levels. The evaluation is conducted by comparing the detected star centroids with the ground truth data extracted from clean star images. The purpose of this analysis is to demonstrate the reliability and robustness of the proposed method in challenging environments that resemble the lunar mission scenario.

4.3.1 Noisy and Low SNR Environment of Dataset 1

A star field test set was constructed to evaluate the performance of the proposed centroiding method under different noise conditions. The dataset, Dataset 1, consists of 4 base star field images (Image 1-1, Image 1-2, Image 1-3 and Image 1-4), each processed in five variants: one clean image and four noisy versions generated using different noise models. Refer Section 3.3 for parameters used in the noise simulation. This results in a total of 16 images, covering a range of SNR levels to simulate varying noise interference commonly encountered in space-based imaging.

Figures 4.4-4.7 present the star field of Dataset 1. For clarity, each figure has been cropped and zoomed from the original test images to allow detailed visual inspection of the star blobs and their distortions under the different noise conditions. The actual size of the images can refer Figure 4.3.

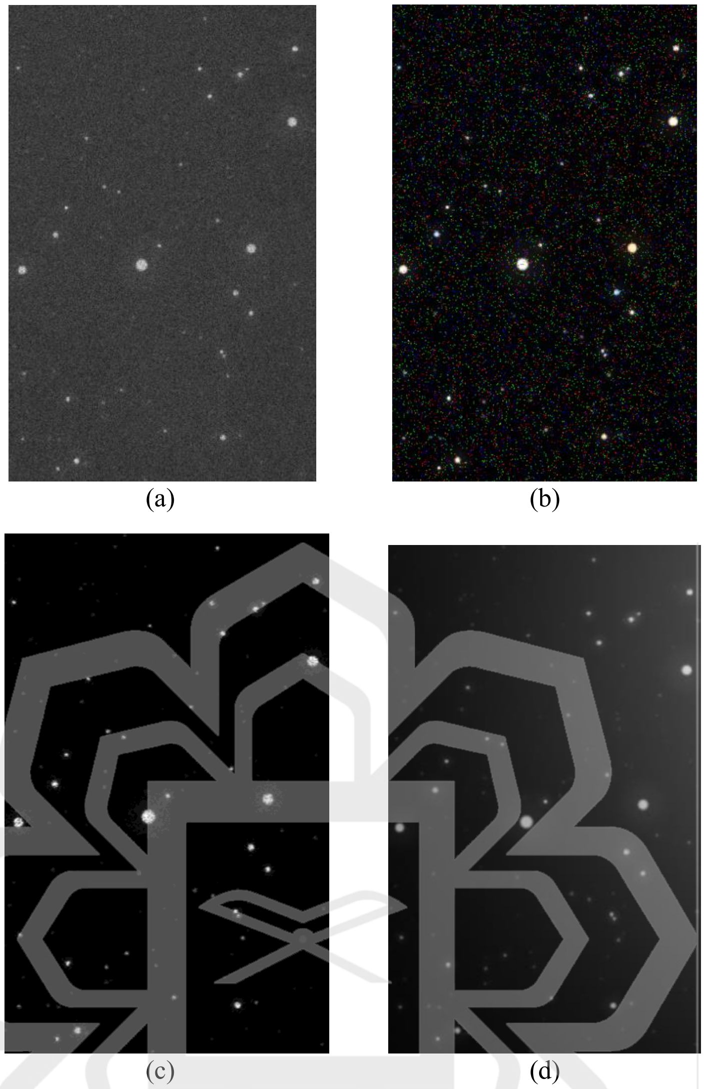

Figure 4.4: Star Image 1-1 under four noise environments, (a) Gaussian and Poisson noise, (b) salt and pepper noise, (c) speckle noise, and (d) sunlight reflection

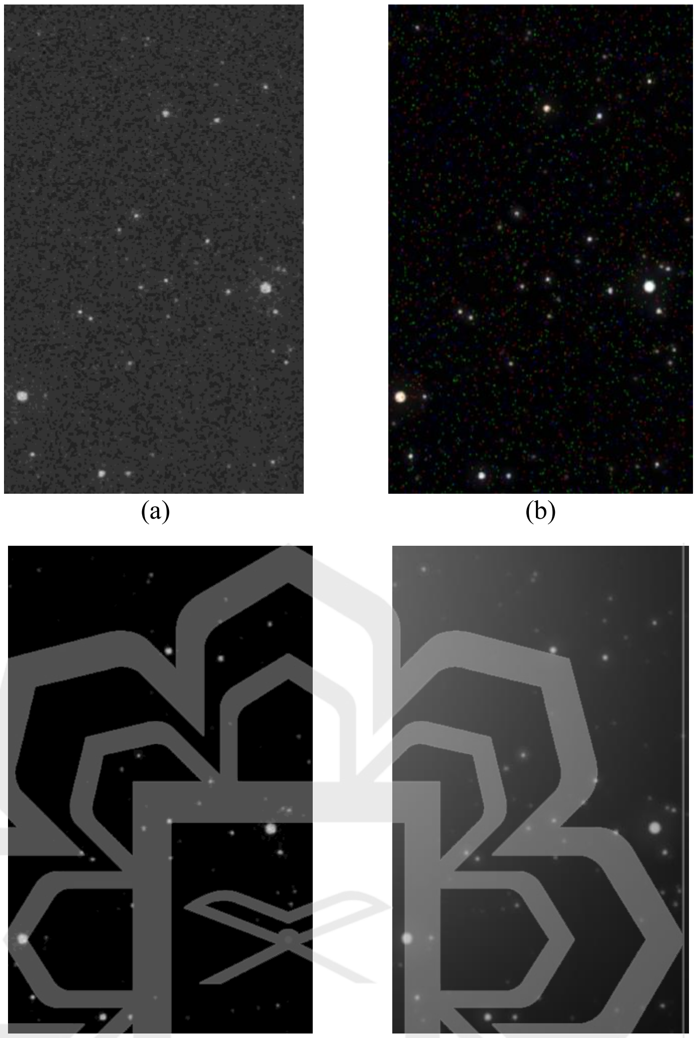

(a) (b) (c) (d)

Figure 4.5: Star Image 1-2 under four noise environments, (a) Gaussian and Poisson noise, (b) salt and pepper noise, (c) speckle noise, and (d) sunlight reflection

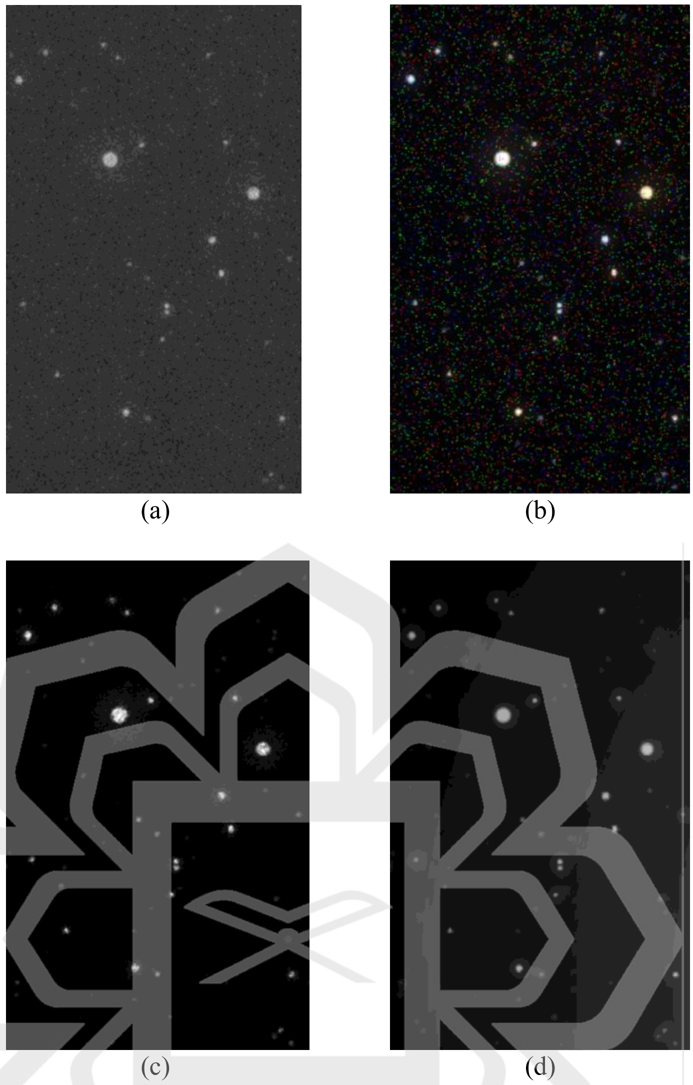

Figure 4.6: Star Image 1-3 under four noise environments, (a) Gaussian and Poisson noise, (b) salt and pepper noise, (c) speckle noise, and (d) sunlight reflection

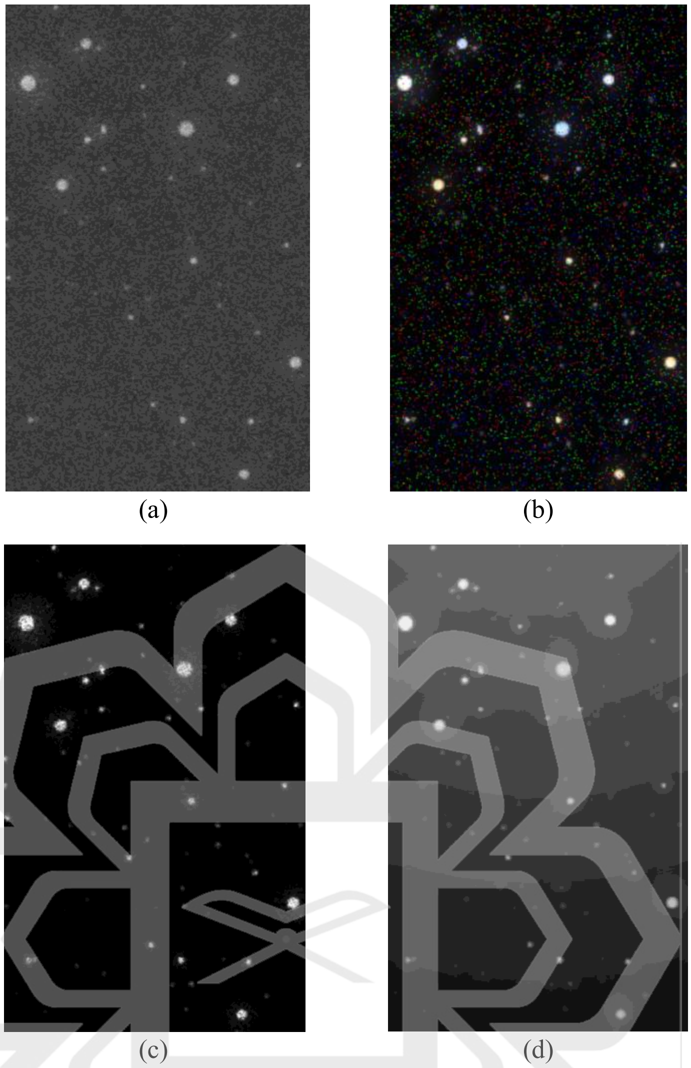

Figure 4.7: Star Image 1-4 under four noise environments, (a) Gaussian and Poisson noise, (b) salt and pepper noise, (c) speckle noise, and (d) sunlight reflection

Table 4.2 presents the SNR levels assigned to Dataset 1, which were used to simulate varying noise conditions for testing in Section 4.3.2. These SNR values were designed to represent different levels of signal degradation, allowing evaluation of the algorithm's robustness under realistic conditions.

Table 4.2: SNR of Star Field in Dataset 1

Noise Models	*Images*			
	1	2	3	4
Poisson+Gaussian	2.89 dB	1.60 dB	-2.96 dB	0.11 dB
Salt Pepper	-2.73 dB	-3.47 dB	-1.29 dB	-2.52 dB
Speckle	2.94 dB	-1.00 dB	-3.16 dB	-0.56 dB
Glare	0.74 dB	0.82 dB	1.07 dB	-0.37 dB

4.3.2 Star Centroid Evaluation

The performance of the proposed algorithm was evaluated using four representative star images, each subjected to the four different noise models. Using the ground truth centroids as a reference, the accuracy of the algorithm was evaluated by calculating the Euclidean distance between the detected and actual centroid positions. For each star, the centroid error was computed, and the RMSE was obtained to provide a statistical measure of detection accuracy under each noise condition. Figure 4.8(a)-(d) presents the centroid detection results for each noise environment, where the ground truth centroids are compared against the detected centroids.

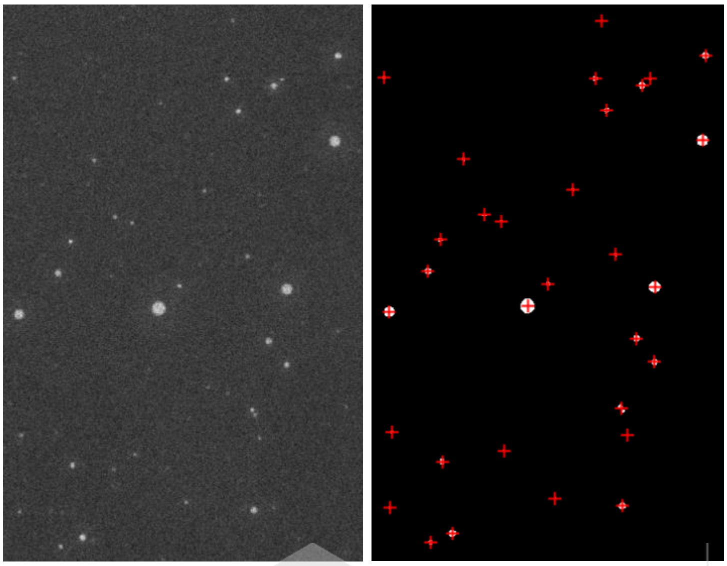
(a)
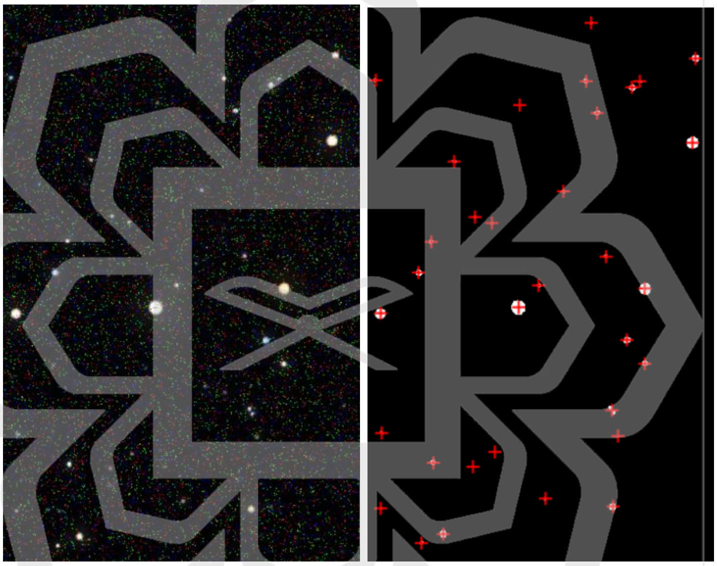
(b)

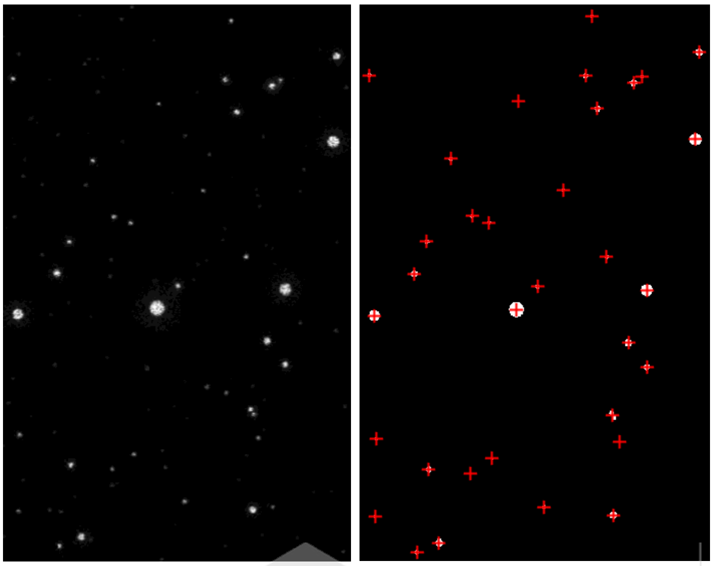

(c)

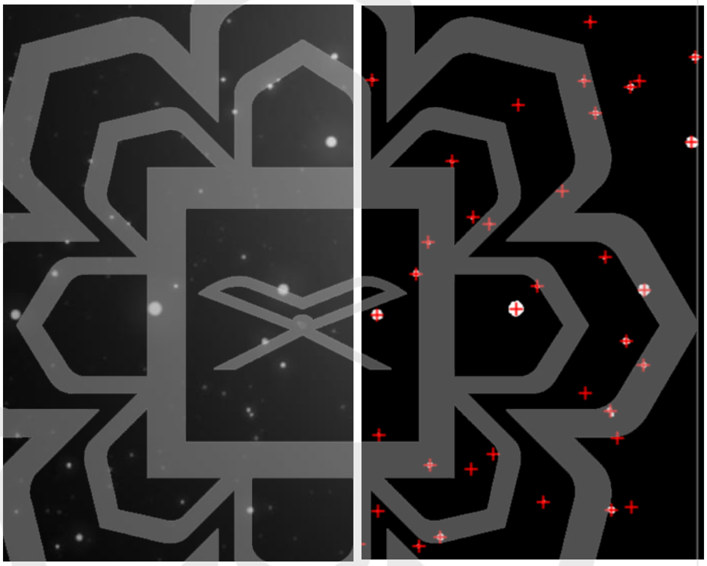

(d)

Figure 4.8: Centroid detection results for Image 1-1 under different noise environments (zoomed view). The red asterisk represents the centre of the star: (a) Gaussian noise with centroid overlay, (b) Salt-and-Pepper with centroid overlay, (c) Speckle noise with centroid overlay, and (d) Sunlight glare with centroid overlay.

The values of the position error are recorded in Figure 4.9. From the graph, it can be observed that as SNR increases, both Euclidean distance and RMSE decrease consistently, indicating that the star centroiding accuracy improves significantly under higher signal quality and lower noise conditions in Dataset 1. RMSE remains slightly higher than Euclidean distance across all SNR levels, with a noticeable improvement (sharp error reduction) around 1 dB SNR, suggesting that the proposed centroiding performance becomes more stable once the noise level drops below a certain threshold.

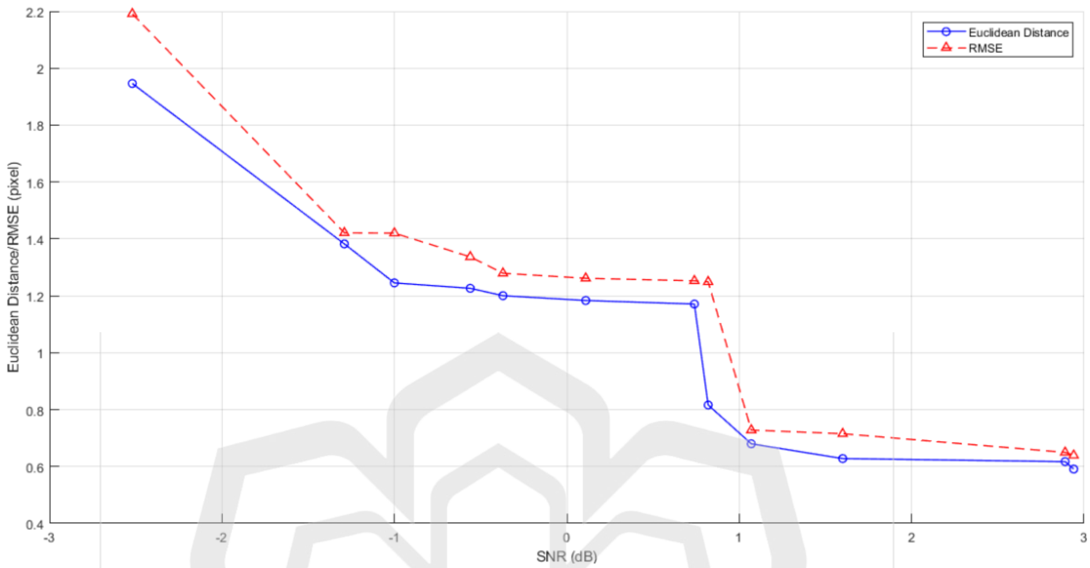

Figure 4.9: Performance evaluation for Dataset 1

The same evaluation process was then extended to the other 12 star fields, subjected to the same noise conditions. These images, which contained a different number of star blobs, allowed for a more comprehensive assessment of the proposed algorithm's performance across varying star field densities and SNR levels. To summarize the findings, the average Euclidean distance errors and RMSE across all stars for each image were recorded. The results are tabulated in Table 4.3 and Table 4.4 respectively.

Table 4.3: Accuracy analysis based on Average Euclidean Distance error (in pixel)

Noise	**Image**				**Average**
	1	**2**	**3**	**4**	
Poisson+Gaussian	0.617	0.628	2.768	1.184	1.299
Salt and Pepper	2.493	4.870	1.383	1.946	2.673
Speckle	0.591	1.245	3.257	1.226	1.580
Glare	1.171	0.816	0.680	1.200	0.967

Among all noise types, sunlight glare reflection gave the smallest average error (0.967 pixels), which means the algorithm was able to locate the star positions quite accurately. On the other hand, images with salt and pepper noise showed the largest error (2.673 pixels), since the strong disruption made some stars harder to detect. The errors under Poisson + Gaussian noise and speckle noise were in between, with averages of 1.299 pixels and 1.580 pixels, respectively.

Table 4.4: Accuracy analysis based on RMSE (in pixel)

Noise	**Image**				**Average**
	1	**2**	**3**	**4**	
Poisson+Gaussian	0.650	0.715	3.047	1.262	1.419
Salt and Pepper	2.501	5.406	1.421	2.191	2.880
Speckle	0.639	1.420	3.567	1.337	1.741
Glare	1.253	1.249	0.728	1.279	1.127

Similar to the Euclidean distance results, sunlight glare again gave the lowest average error (1.127 pixels). The highest RMSE was found in the images with salt and pepper (2.880 pixels), showing the strong effect of corrupted white and black pixels on centroid accuracy. Poisson + Gaussian noise and speckle noise produced moderate RMSE values of 1.419 pixels and 1.741 pixels, respectively. For next testing, the algorithm will be applied to match the detected stars with existing star catalogue in the next section.

4.4 STAR IDENTIFICATION PERFORMANCE

In addition to the noisy test set, a second dataset consisting of 4 low-noise star field images (Image 2-1, Image 2-2, Image 2-3 and Image 2-4) was employed. This dataset, referred to as Dataset 2, was designed to test the algorithm's ability to accurately detect and identify real stars under conditions with minimal noise interference. The main goal was to validate the centroiding accuracy and confirm that the detected stars correspond to actual celestial objects listed in the reference star catalogue.

Each image in this dataset was captured at different times, as summarized in Figures 4.10-4.13. Three reference stars were marked in each frame (1, 2 and 3) to serve as identification anchors during catalogue matching. These reference stars were selected based on their brightness stability and consistent appearance across all captured images. Figure 4.10(a) shows the star field of Image 2-1 with an SNR of 0.22 dB. Despite the relatively low SNR, the stars remain visible enough for centroid extraction. Figure 4.10(b) presents the centroid positions of all detected stars, illustrating how the proposed method localises each star within the image. The coordinate of the designated reference star used for transformation and matching is listed in Table 4.5.

(a)

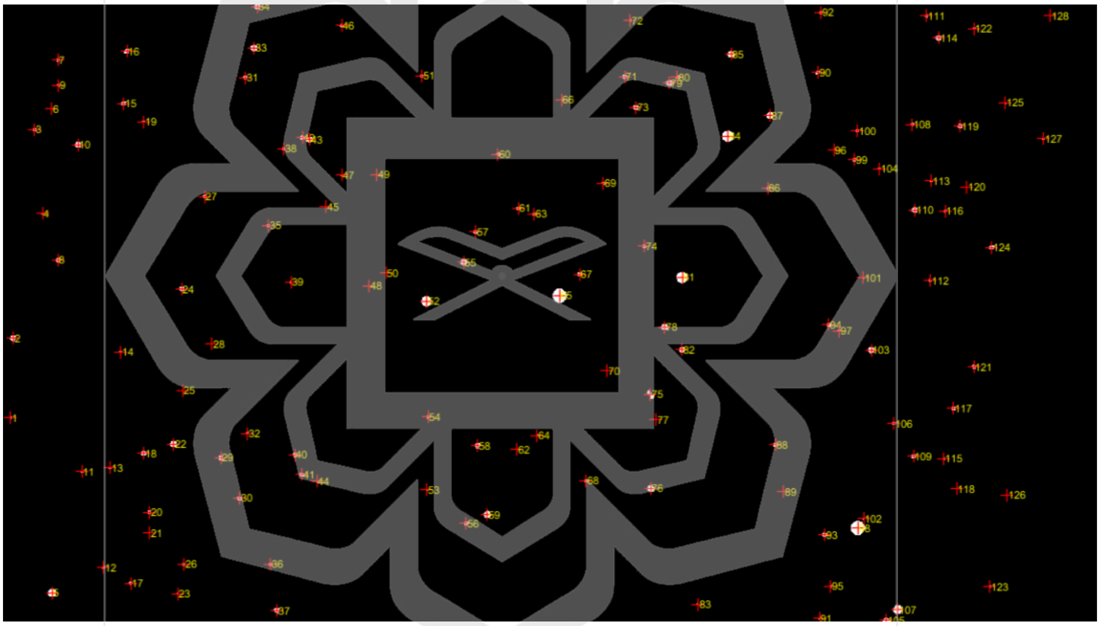

(b)

Figure 4.10: (a) Star field of Image 2-1 with an SNR of 0.22 dB. (b) Centroid positions of all detected stars.

Table 4.5: Reference Star Coordinate of Image 2-1

Star #	*Pixel Coordinate* (x, y)	*RA-coordinate (°)*	*Dec-coordinate (°)*	*HIP*
1	952, 497	309.5845	-1.1051	101847
2	1162, 466	309.1818	-2.5499	101692
3	1239, 225	307.4124	-2.8855	101101

Figure 4.11(a) displays the star field of Image 2-2, has an SNR of 0.14 dB, the lowest among the four images. This low SNR indicates a more challenging detection scenario with fainter stars and higher noise interference. Figure 4.11(b) shows the computed centroid positions of the detected stars. The reference star used for identification in this image is listed in Table 4.6.

(a)

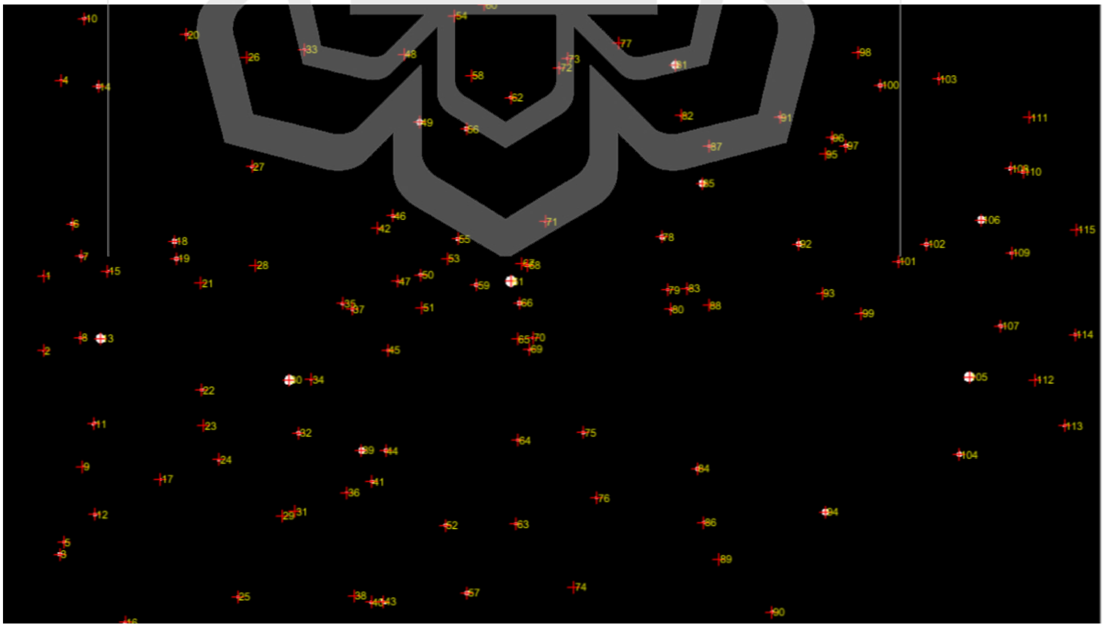

(b)

Figure 4.11: (a) Star field of Image 2-2 with an SNR of 0.14 dB. (b) Centroid positions of all detected stars.

Table 4.6. Reference Star Coordinate of Image 2-2

Star #	*Pixel Coordinate* (x, y)	*RA-coordinate (°)*	*Dec-coordinate (°)*	*HIP*
1	212, 275	213.2249	-10.2689	69427
2	264, 327	211.6917	-9.3149	68940
3	374, 203	214.0043	-6.0074	69701

Figure 4.12(a) presents the star field of Image 2-3, with an SNR of 0.29 dB. This image has one of the highest star counts in the dataset, making it suitable for observing the algorithm's performance on denser star patterns. Figure 4.12(b) shows the resulting centroid locations of all detected stars. The coordinates of the reference star associated with this image are provided in Table 4.7.

(a)

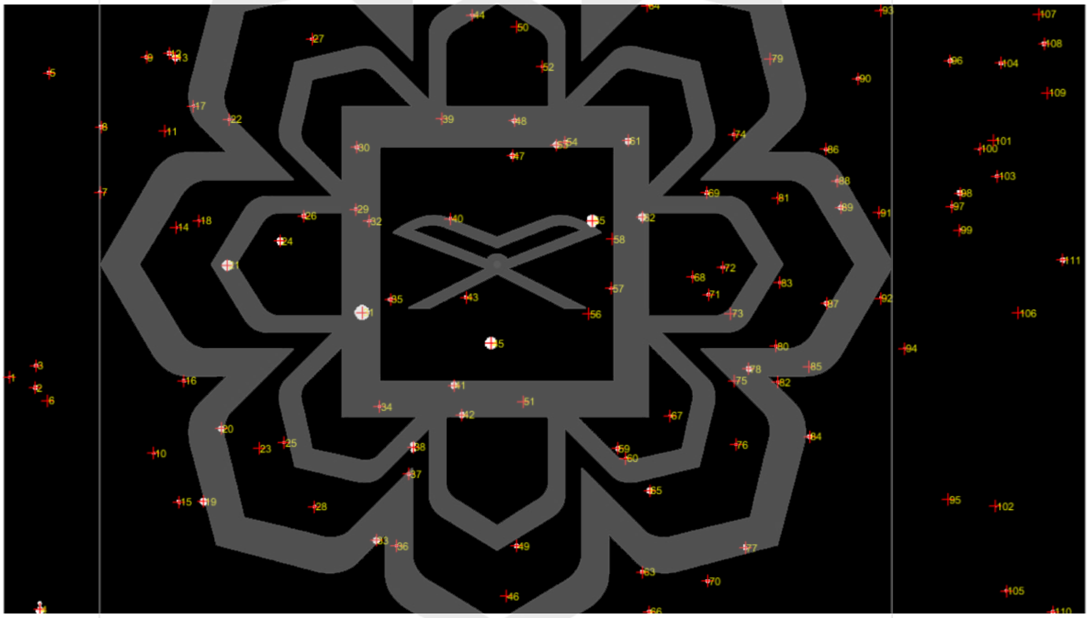

(b)

Figure 4.12: (a) Star field of Image 2-3 with an SNR of 0.29 dB. (b) Centroid positions of all detected stars.

Table 4.7: Reference Star Coordinate of Image 2-3

Star #	*Pixel Coordinate* (x, y)	*RA-coordinate (°)*	*Dec-coordinate (°)*	*HIP*
1	398, 463	309.8536	0.4867	101936
2	491, 420	309.3265	0.0969	101746
3	637, 547	309.5842	-1.1053	101847

Figure 4.13(a) shows the star field of Image 2-4, an SNR of 0.27 dB. The higher star density places additional demand on blob separation and centroid detection. Figure 4.13(b) displays the detected centroid positions, demonstrating that the algorithm can still isolate and extract each star's position even in crowded fields. The reference star used for identification in this image is listed in Table 4.8.

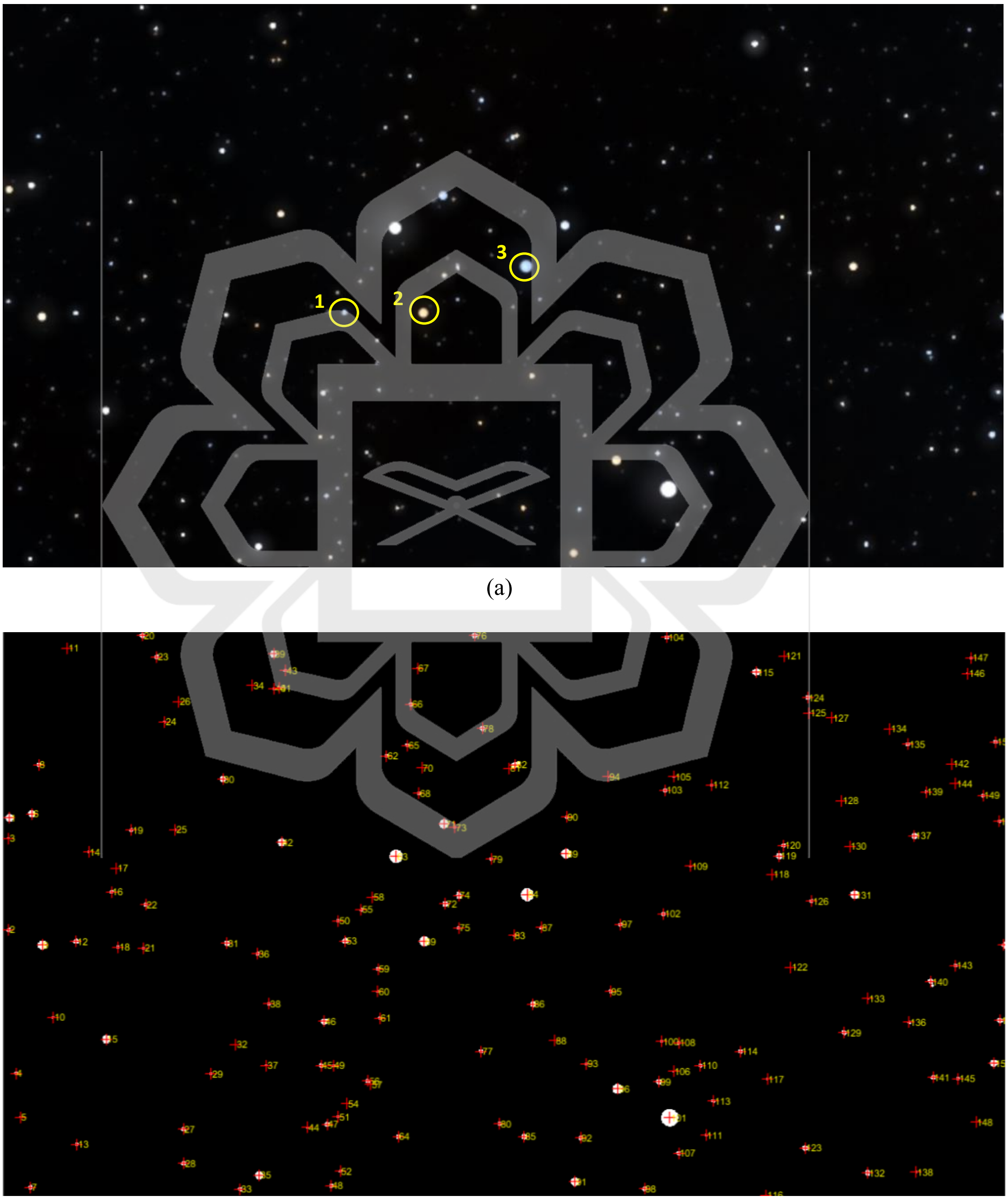

(a)

(b)

Figure 4.13: (a) Star field of Image 2-4 with an SNR of 0.27 dB. (b) Centroid positions of all detected stars.

Table 4.8. Reference Star Coordinate of Image 2-4

Star #	*Pixel Coordinate* (x, y)	*RA-coordinate (°)*	*Dec-coordinate (°)*	*HIP*
1	656,592	270.6257	22.9232	88346
2	807, 593	271.508	22.2189	88657
3	1005, 503	272.1895	20.8146	88886

The identification results for Dataset 2 are summarized in Table 4.9, which presents the number of detected stars, matched stars, false identification rate (FIR), and the corresponding angular distance error for each image.

Table 4.9. Summary of star identification evaluation

Image	**Number of Detected Star**	**Number of Matched Star**	**FIR (%)**	**Angular Distance Error (°)**
2-1	128	109	14.8	0.0049
2-2	70	68	2.9	0.0234
2-3	131	108	17.6	0.0094
2-4	176	103	41.5	0.0331

From the results, it can be observed that the proposed algorithm performed well across all four images, achieving high identification accuracy and low angular distance error. The FIR remained below 20% for most cases, except for Image 2-4, which recorded a higher FIR of 41.5%. Despite these variations, the overall angular distance error for all images remained below 0.05°, indicating strong consistency in the centroid localization and star matching process.

Figure 4.14 illustrates the evaluation metrics of the proposed algorithm for all four images in Dataset 2. The graph visualizes the number of detected stars (blue bars), FIR (orange bar), and angular distance error (red bar) for each image.

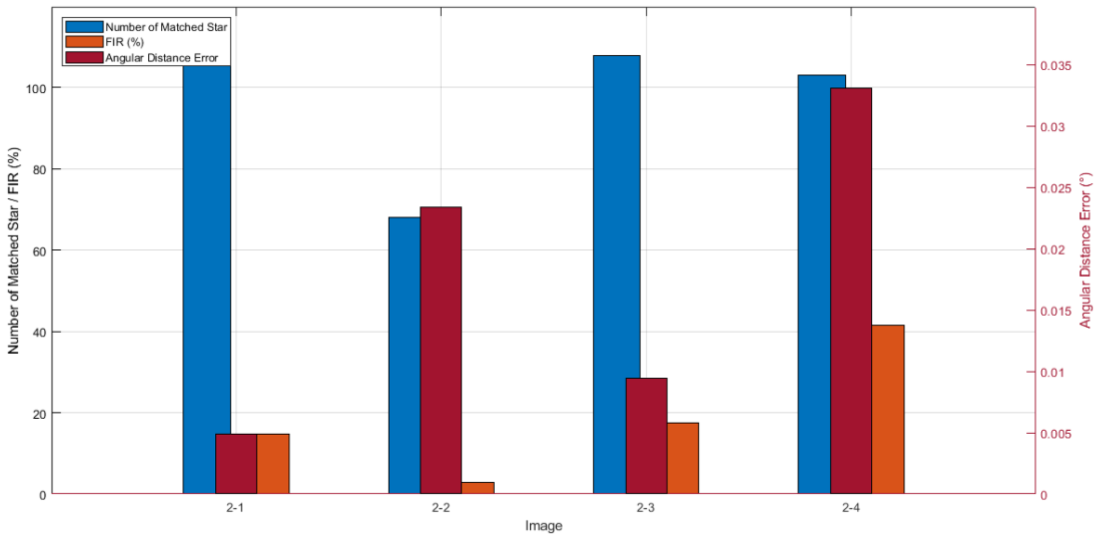

Figure 4.14: Performance evaluation for Dataset 2

From the figure, it can be seen that Images 2-1 and 2-3 achieved the highest number of detected stars, corresponding to a lower angular distance error of less than 0.01°, indicating highly accurate centroid localization and identification. Image 2-2, despite having fewer detected stars due to a smaller star field region, achieved the lowest FIR of 2.9%, reflecting the algorithm's robustness when fewer but clearer stars are present. In contrast, Image 2-4 shows a higher FIR, consistent with the higher density of stars (176 total), which increases the chance of centroid overlap and misidentification. This rise in FIR also corresponds to a higher angular distance error of 0.033°, confirming that dense star fields can slightly degrade identification accuracy.

4.5 COMPARATIVE EVALUATION WITH EXISTING METHODS

To further assess the performance of the proposed centroiding algorithm, an additional dataset, Dataset 3, consisting of 30 star images with varying SNR, was employed. Unlike the previous testing in Section 4.4, which emphasized star identification through catalogue matching in celestial coordinates, this evaluation focuses on star detection and centroid estimation in pixel coordinates.

The aim of this comparative study is to benchmark the proposed method against several existing approaches under different noise conditions. The performance of each method was evaluated using three quantitative metrics: RMSE, Euclidean distance and FDR.

4.5.1 Centroid Extraction Under Low SNR Images

Figure 4.15(a)-(d) are the selected data of 4 images and Table 4.9 presents the SNR values for each image. The full data of 30 star images in Dataset 3 is attached in Appendix A.

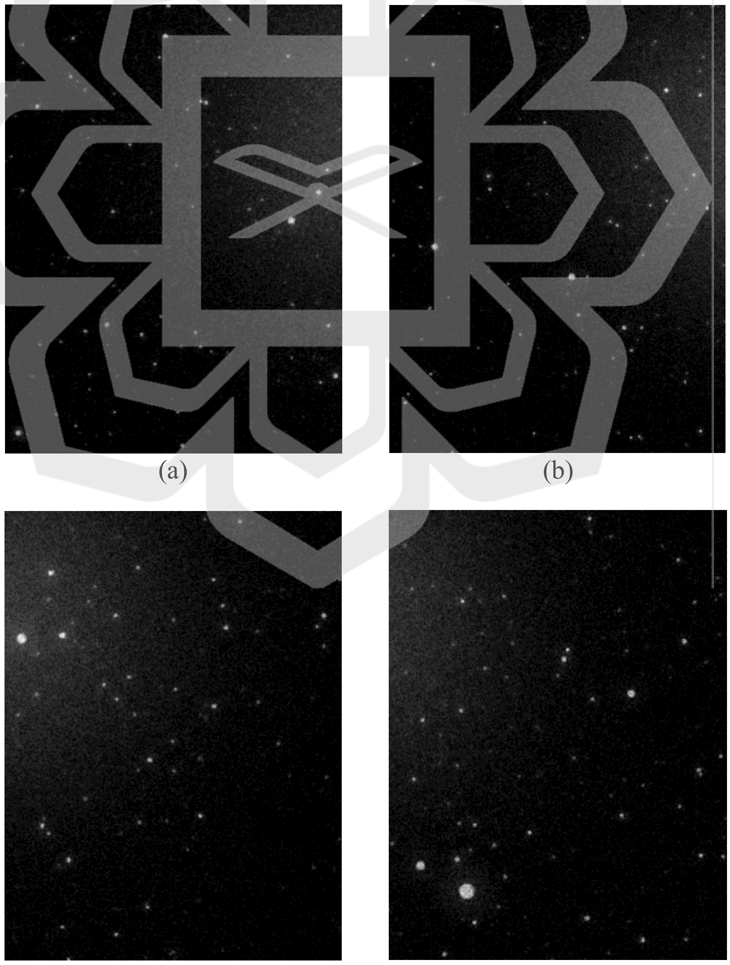

(a) (b) (c) (d)

Figure 4.15: Selected star images in Dataset 3. (a) Image 3-1, (b) Image 3-2, (c) Image 3-3, and (d) Image 3-4.

As shown in Figure 4.15, the images exhibit varying levels of background noise and star visibility. Table 4.10 provides the specific SNR values for these images, illustrating the low-signal conditions, reaching as low as -4.71 dB under which the centroid extraction algorithm was tested.

Table 4.10: SNR of selected star images in Dataset 3

Image	*3-1*	*3-2*	*3-3*	*3-4*
SNR (dB)	-4.71	-2.09	0.72	0.53

In such conditions, the reflected starlight captured by a star sensor is often weak due to the absence of an atmosphere, harsh illumination contrast, and scattered light from the lunar regolith (H. Lin et al., 2020b; Marshal et al., 2023; Velichko et al., 2022). Therefore, testing under these SNR levels provides a realistic performance evaluation of the centroiding algorithm.

4.5.2 Accuracy Analysis and Comparison

To further evaluate the algorithm's robustness, a comparative analysis was conducted using Dataset 3 under the same low-SNR conditions. The proposed centroiding method was compared with existing centroid extraction algorithms, including the Centre of Mass (COM) algorithm, Gaussian fitting, and Sieve Search Algorithm (SSA). The algorithms were implemented manually based on their mathematical formulations and procedures described in the literature, rather than using pre-installed or built-in library functions. This approach was chosen to ensure fair comparison under the same preprocessing conditions and parameter settings. These techniques are commonly used in star sensor image processing due to their balance between computational efficiency and accuracy.

The comparison of the position error or Euclidean distance is visualised in graph from Figure 4.17, 4.19, 4.21 and 4.23. The x-axis refers to the star count, where the count starts from the most left side of the star image until the rightmost side of the image. For reference, the actual star image size for the star count can be observed in Figure 4.3.

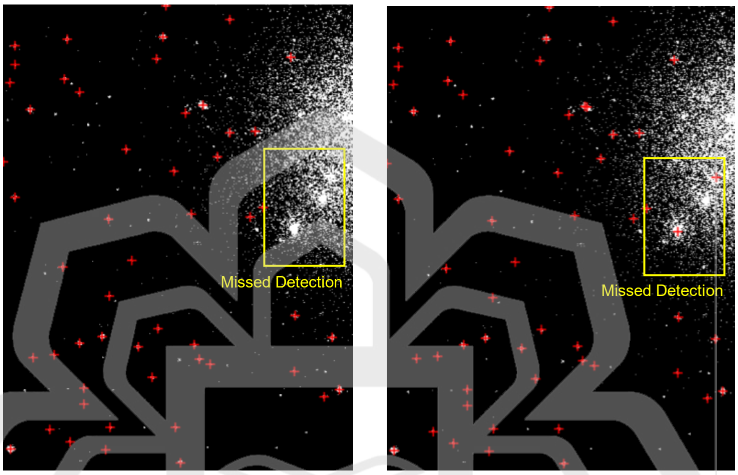

(a) (b)

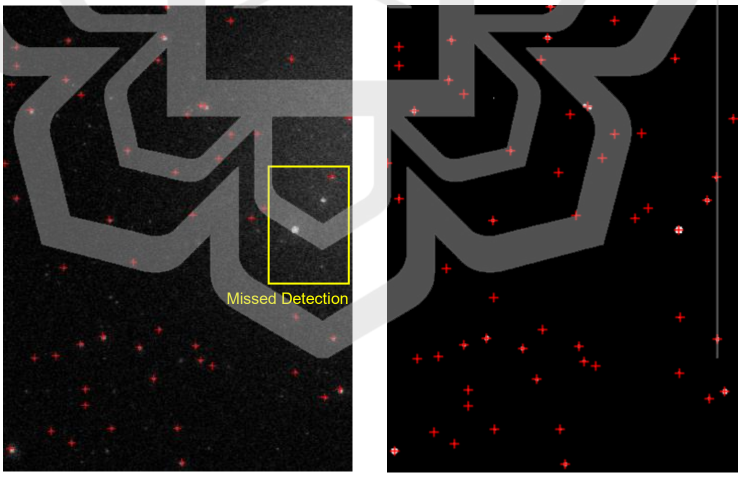

(c) (d)

Figure 4.16: Centroiding results for Image 3-1 under an SNR of -4.71 dB. (a) Centre of Mass (COM) method shows several missed detections in dense star regions due to noise interference within the highlighted area. (b) Gaussian Fitting exhibits slightly improved centroid placement; however, some weak stars are still undetected under low SNR conditions. (c) Sieve Search Algorithm (SSA) demonstrates better noise suppression yet misses several faint stars. (d) Proposed method successfully detects and locates more star centroids within the same region.

Figure 4.17 shows that the SSA produces the highest Euclidean distance values among all methods, indicating greater centroiding errors. Toward the right side of Image 3-1, all methods exhibit increased errors reaching up to nearly 5 pixels and several missing stars. This is likely due to higher noise intensity in that region. In contrast, the proposed algorithm achieves the lowest Euclidean distance, with most centroiding errors maintained below 1 pixel.

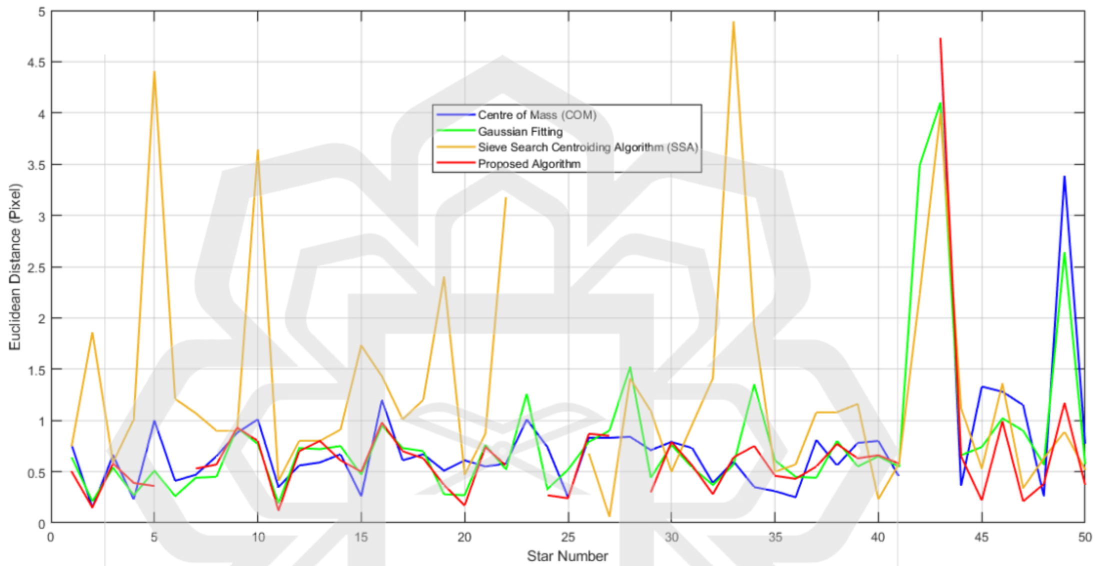

Figure 4.17: Comparison of Euclidean distance for each star in Image 3-1

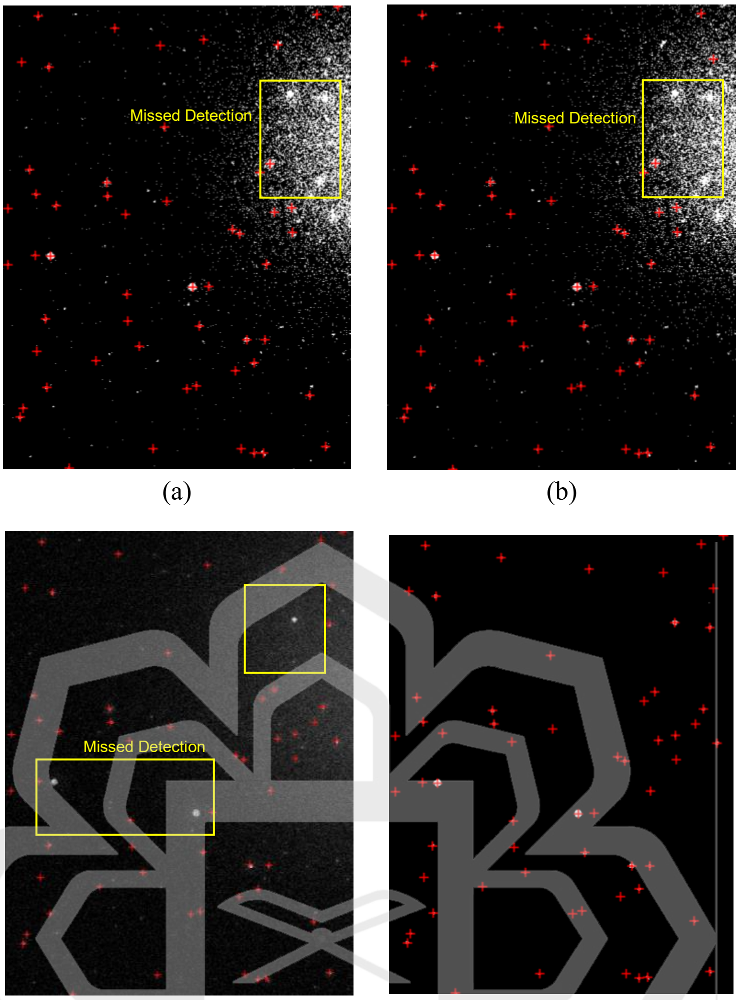

(a) (b) (c) (d)

Figure 4.18: Centroiding results for Image 3-2 under an SNR of -2.09 dB. (a) COM method shows poor detection in high-noise regions, with several missed centroids in the highlighted upper area. (b) Gaussian Fitting provides slightly better accuracy but still fails to detect faint stars affected by noise clustering. (c) SSA improves star localization; however, multiple faint stars in both the upper and middle regions remain undetected. (d) Proposed method achieves the most stable detection, maintaining accurate centroid placement even in low-intensity regions.

Graph in Figure 4.19 shows that SSA again records the highest position error and has the most missing stars. The relatively low SNR in Image 3-2 causes all methods to show higher Euclidean distance values, ranging between 1-2 pixels, along with several undetected stars. Nevertheless, the proposed method shows good performance with minimal missing stars and low position error, comparable to COM and Gaussian Fitting method.

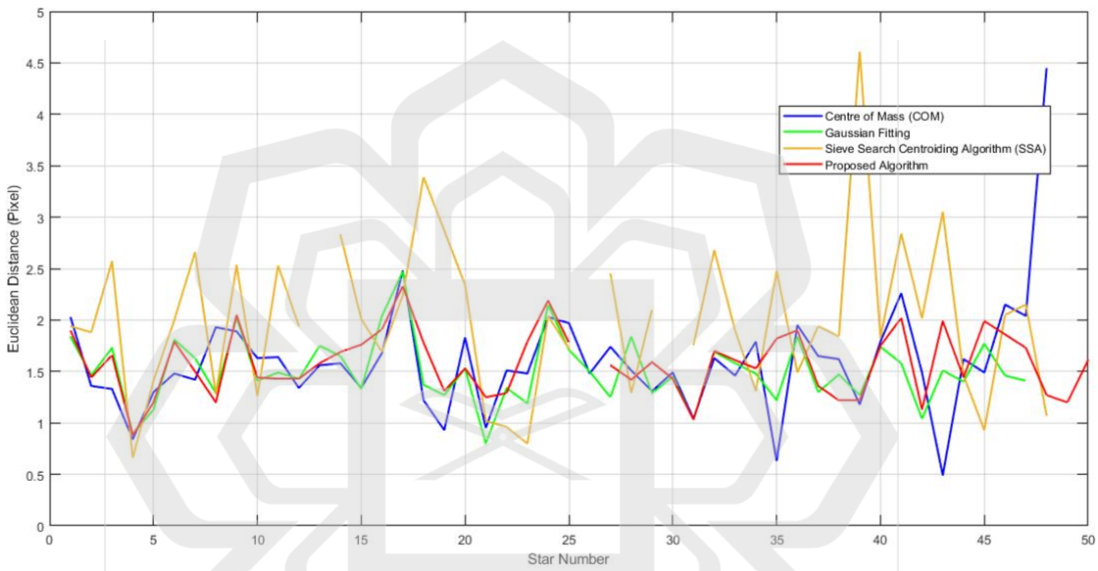

Figure 4.19: Comparison of Euclidean distance for each star in Image 3-2

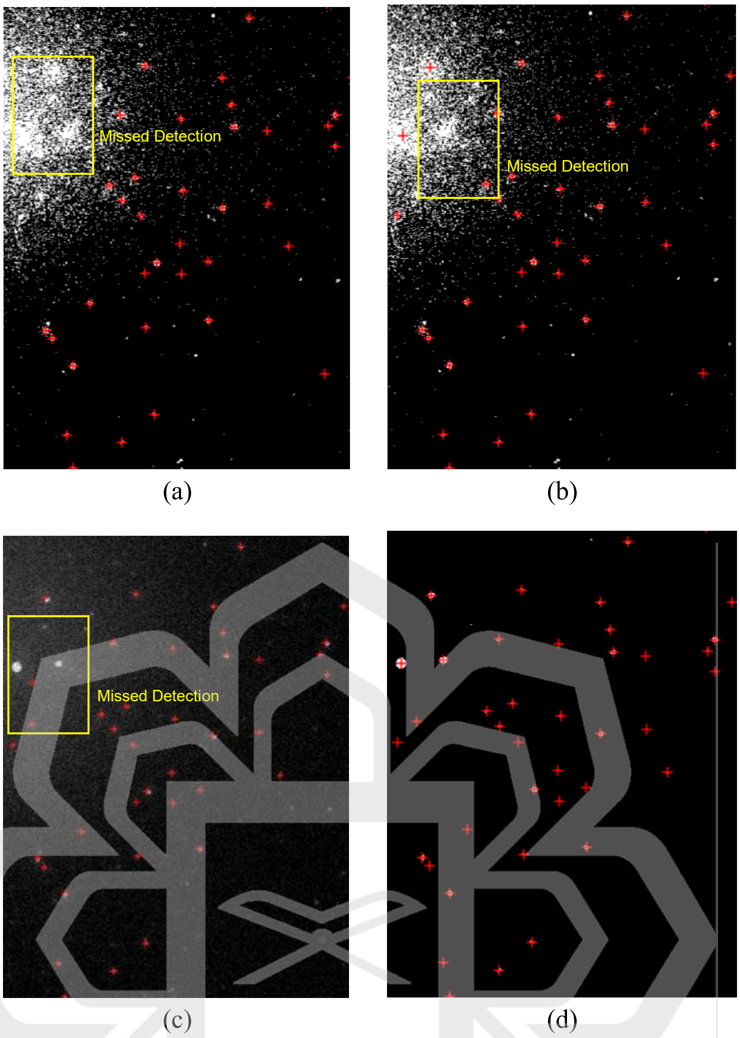

Figure 4.20: Centroiding results for Image 3-3 under an SNR of 0.72 dB. (a) COM method exhibits centroid deviation in the upper left region due to noise contamination, leading to multiple missed detections. (b) Gaussian Fitting provides slightly improved localization but still fails to resolve faint stars affected by glare and background variation. (c) SSA enhances centroid clarity yet misses several dim stars within the highlighted noisy region. (d) Proposed method successfully detects the majority of visible stars with precise centroid placement, outperforming the other methods in maintaining centroid accuracy under moderate noise levels.

As illustrated in Figure 4.21, corresponding to Image 3-3, the noise is concentrated on the left side of the image, resulting in higher error values and several missing stars across all algorithms. As the star number increases toward the right, the error gradually decreases. However, the proposed algorithm maintains most centroiding errors below 2 pixels, outperforming the other methods under the same noisy conditions.

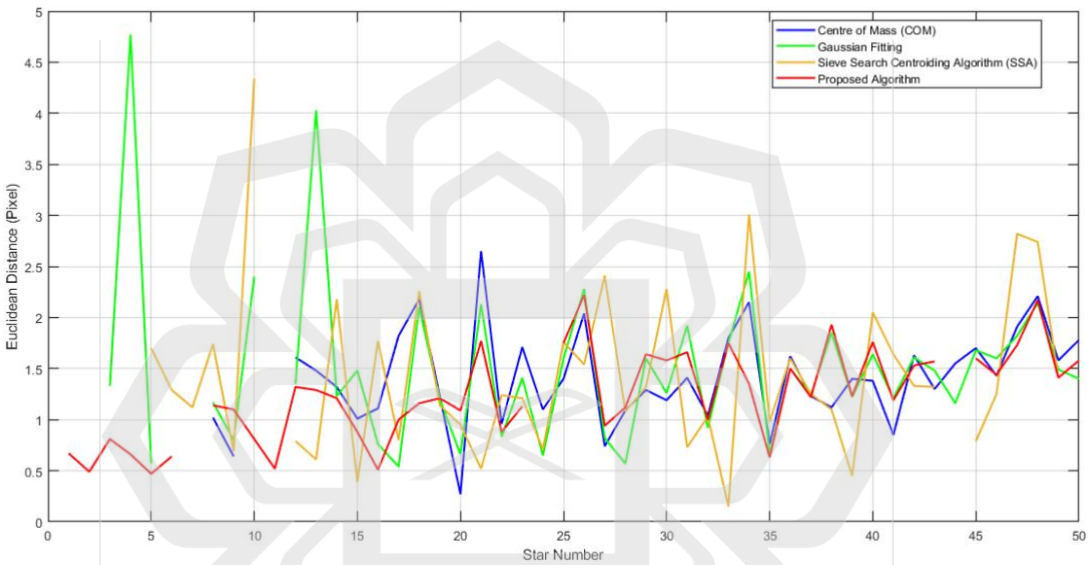

Figure 4.21: Comparison of Euclidean distance for each star in Image 3-3

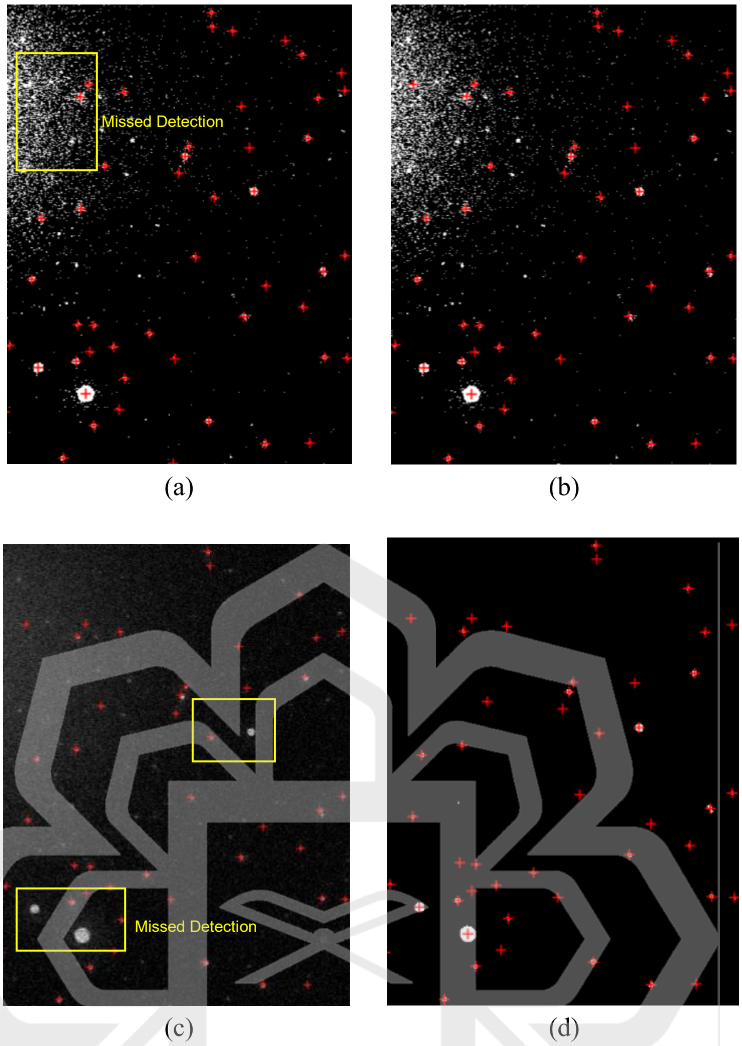

Figure 4.22: Centroiding results for Image 3-4 under an SNR of 0.53 dB. (a) COM method provides good centroid placement with fewer missed detections; however, a few faint stars remain undetected near the noisy region. (b) Gaussian Fitting method produces more stable centroiding compared to COM. (c) SSA exhibits multiple missed detections in few regions especially for faint stars. (d) The proposed algorithm effectively identifies most stars across the frame with minimal missed detections, demonstrating high robustness and accuracy in low-SNR imaging environments.

Figure 4.23 reveals that most methods yield relatively high position errors, approaching 4 pixels. The SSA method shows several missed detections, similar to the results in Figure 4.20(c). Both Gaussian Fitting and COM exhibit significant centroid errors, with most values exceeding those of the proposed method.

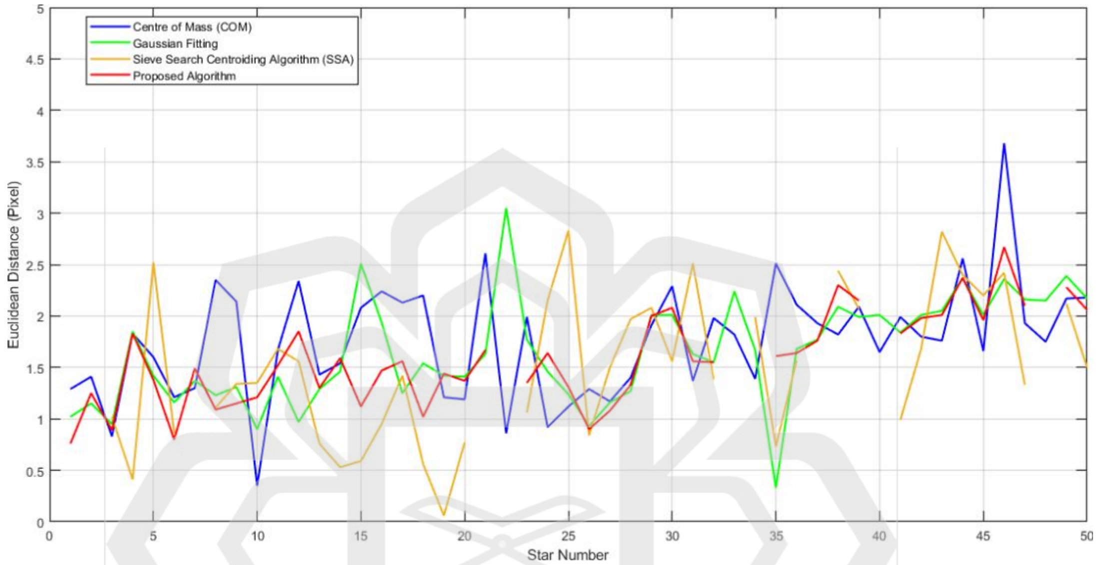

Figure 4.23: Comparison of Euclidean distance for each star in Image 3-4

This experiment is also extended to the remaining 26 star field images to obtain a more comprehensive set of results for evaluation. The star images are attached in Appendix A. The performance result for all methods in each 30 images is shown in Figure 4.24. Both aspects illustrate a similar result. SSA shows the highest position error, followed by Gaussian Fitting and COM. Proposed algorithm shows the lowest values, indicating a better performance in term of accuracy and robustness. Table 4.11 presents the quantitative comparison in average of the centroiding accuracy and reliability among the four tested methods using Dataset 3.

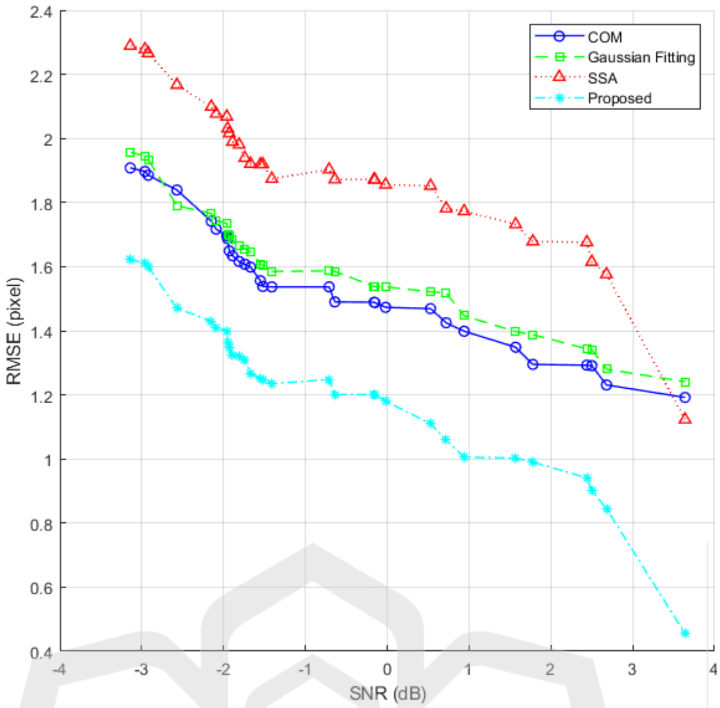

(a)

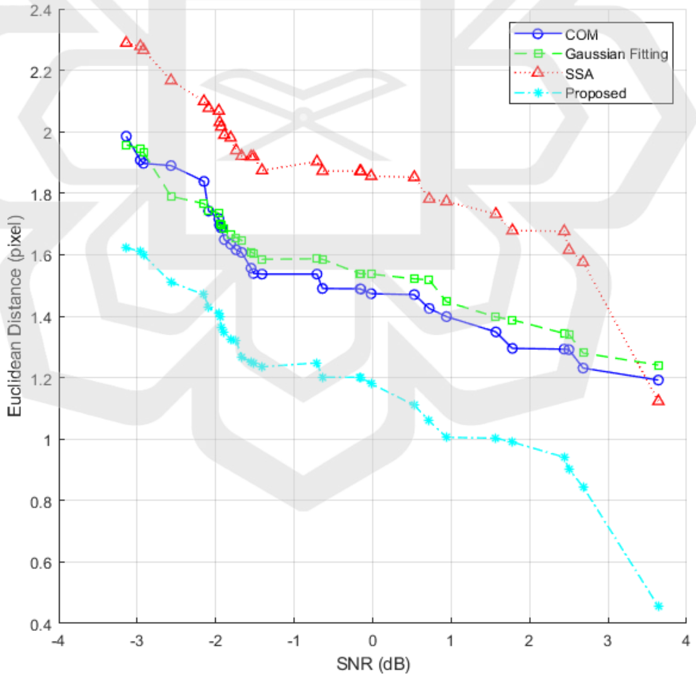

(b)

Figure 4.24: Performance comparison between existing methods and proposed method (a) RMSE (b) Euclidean distance

Table 4.11: Summary of accuracy analysis in average of the proposed method with other methods

Methods	**RMSE**	**Euclidean Distance**	**False Detection Rate (%)**
Centre of Mass (COM)	1.551	1.373	13.949
Gaussian Fitting	1.599	1.368	9.983
Sieve Search Algorithm (SSA)	1.904	1.679	12.637
Proposed Algorithm	**1.218**	**1.143**	**6.716**

From the results, the proposed method consistently achieved the lowest errors, with an average RMSE of 1.218 pixels and an average Euclidean distance of 1.143 pixels, outperforming the other three methods. It also recorded the lowest FDR of 6.716%, indicating a more reliable detection rate and fewer false identifications. In contrast, the COM and SSA methods exhibited higher error values and greater false detections, suggesting greater sensitivity to noise and weaker noise suppression capability. The Gaussian Fitting method performed moderately well, achieving competitive centroid accuracy but with slightly higher detection errors in some images.

Overall, these findings demonstrate that the proposed method provides a more stable and accurate centroiding performance, particularly under challenging low SNR environments, which makes it more suitable for lunar star sensing applications where noise and illumination variation are significant.

4.6 SUMMARY

This chapter presents the experimental evaluation of the proposed algorithm using a hardware setup featuring a Raspberry Pi 5 and an ArduCAM OV2311 monochrome module. Performance was tested across three datasets: Dataset 1 demonstrated that the algorithm maintains stability under noise, with sunlight glare causing the least error (0.967 pixels) and salt and pepper noise the most (2.673 pixels). Dataset 2 confirmed strong identification reliability, keeping overall angular distance errors below 0.05°. Finally, benchmarking in Dataset 3 against existing methods like COM, SSA, and Gaussian Fitting showed that the proposed method achieved the highest accuracy, recording the lowest average RMSE (1.218 pixels) and the lowest False Detection Rate (6.716%).

CHAPTER 5

CONCLUSION AND FUTURE WORKS

5.1 CONCLUSION

This research successfully developed and optimized an enhanced centroiding algorithm specifically designed for lunar surface navigation. By addressing the unique physical and optical challenges of the Moon such as the absence of an atmosphere and intense solar reflections from the regolith, the study provides a reliable alternative to traditional algorithms that often fail in low-SNR environments. The novelty of this work does not solely lie in the individual image processing techniques, since methods such as median filtering and centroiding are already established. Instead, the contribution comes from integrating these techniques into a single low complexity centroiding pipeline and evaluating its robustness under four different noise conditions to simulate lunar environment: Gaussian, Poisson, salt and pepper, and speckle noise. The research objectives were met through the systematic investigation of lunar noise characteristics, the implementation of a robust processing pipeline, and a comprehensive benchmarking against established methods.

5.2 OBJECTIVE ACHIEVEMENTS

The first objective was achieved by investigating the unique lunar environmental factors and noise characteristics that degrade star detection through rigorous mathematical modelling. The research analysed five distinct models (Gaussian, Poisson, salt and pepper, speckle noise, and sunlight glare) to simulate sensor electronics, photon shot noise, and hardware disruptions common in the harsh, low-SNR lunar environment. By focusing on CMOS technology over CCDs for its superior radiation resistance, the study established the necessary parameters to understand how regolith reflectance and extreme lighting impact positional accuracy.

The second objective was met through the development of an enhanced centroiding algorithm featuring a multi-stage processing pipeline specifically tuned for these conditions. This pipeline employs a Gaussian Point Spread Function (PSF) to simulate optical blur and a median filtering method to effectively suppress impulse noise while preserving star blob edges. Furthermore, the implementation of a dynamic threshold (set at 30% of maximum intensity) and an intensity-weighted Centre of Mass (COM) approach ensures that the algorithm can adaptively isolate stars and compute sub-pixel coordinates even under intense glare.

The final objective was fulfilled by validating and benchmarking the algorithm's performance to ensure its reliability for autonomous navigation. Detected centroids were mapped to celestial coordinates using affine transformations and successfully cross-referenced with the Hipparcos star catalogue to confirm identification accuracy. Comparative evaluations against the standard COM, Gaussian Fitting, and Sieve Search Algorithm (SSA) proved the proposed method's superiority, as it recorded the lowest average RMSE (1.218 pixels) and the lowest False Detection Rate (6.716%) across all testing datasets.

5.3 FUTURE WORKS

To further improve the algorithm's applicability for real space missions, several future directions are proposed. Firstly, incorporating additional noise models, such as solar radiation and surface reflection noise, would enhance the algorithm's resilience under harsh lunar conditions. Additionally, integrating real star catalogues with more real star images will further ensure the algorithm's reliability and alignment with actual celestial references. For real mission applicability, adaptations could be made for spaceflight and lunar navigation systems, such as optimizing processing for onboard hardware and ensuring robustness against environmental variations in space. Through these advancements, the proposed algorithm holds promise as a dependable component in onboard star sensors for autonomous navigation in lunar exploration missions.

REFERENCES

Akshita Chugh. (2020, December 8). *MAE, MSE, RMSE, Coefficient of Determination, Adjusted R Squared — Which Metric is Better?* Medium. https://medium.com/analytics-vidhya/mae-mse-rmse-coefficient-of-determination-adjusted-r-squared-which-metric-is-better-cd0326a5697e

Anqi Fan. (2023, November 30). *China-russia lunar base collaboration "A perfect match."* . Global Times.

Azzeh, J., Zahran, B., & Alqadi, Z. (2018). Salt and Pepper Noise: Effects and Removal. *JOIV : International Journal on Informatics Visualization*, *2*(4), 252–256.

Barbu, T. (2013). Variational Image Denoising Approach with Diffusion Porous Media Flow. *Abstract and Applied Analysis*, *2013*, 1–8.

Cai, H., Yang, Z., Cao, X., Xia, W., & Xu, X. (2014). A new iterative triclass thresholding technique in image segmentation. *IEEE Transactions on Image Processing*, *23*(3), 1038–1046.

Ceresoli, M., Maccari, F., Moresi, E., & Lavagna, M. (2025). Design and station-keeping strategies for robust lunar navigation constellations. *Acta Astronautica*, *236*, 20–31.

Chan, R. H., Chung-Wa, & Nikolova, M. (2005). Salt-and-pepper noise removal by median-type noise detectors and detail-preserving regularization. *IEEE Transactions on Image Processing*, *14*(10), 1479–1485.

Chen, C., Chen, Q., Gao, C., Zhang, N., Wang, X., & Zhai, Y. (2018). Method of Blob detection based on radon transform. *2018 Chinese Control And Decision Conference (CCDC)*, 5762–5767.

Chen, T., Yin, J., Hu, P., Zhang, X., Yu, X., Wu, H., & Guo, L. (2025). Autonomous nighttime navigation with lunar polarized light: A 3-D attitude determination approach. *Chinese Journal of Aeronautics*, *38*(11), 103577.

Chen, W.-C., & Jan, S.-S. (2023). Star Tracking Algorithm Based on Local Dynamic Background Reduction for Eliminating Stray Light Interference From Star Spot Data. *IEEE Sensors Journal*, *23*(18), 21534–21543.

Chen, W.-T., Chen, P.-Y., Hsiao, Y.-C., & Lin, S.-H. (2019). A Low-Cost Design of 2D Median Filter. *IEEE Access*, *7*, 150623–150629.

Chen, X., Zheng, Y., Du, L., & Zhang, Z. (2024). The Design and Analysis of a Lunar Navigation SmallSat for Southern Hemisphere Moon Navigation. *IEEE Access*, *12*, 91040–91052.

Chin, G., Brylow, S., Foote, M., Garvin, J., Kasper, J., Keller, J., Litvak, M., Mitrofanov, I., Paige, D., Raney, K., Robinson, M., Sanin, A., Smith, D., Spence, H., Spudis, P., Stern, S. A., & Zuber, M. (2007). Lunar Reconnaissance Orbiter Overview: The Instrument Suite and Mission. *Space Science Reviews*, *129*(4), 391–419.

China Space Record. (2016). *Chang'e 5-T1*. https://chinaspacereport.wordpress.com/spaceflight/change5t1/

China Space Report. (2016). *Change'e 3*. https://chinaspacereport.wordpress.com/spaceflight/change3/

Chukhovskii, F. N., Konarev, P. V., & Volkov, V. V. (2023). Denoising of the Poisson-Noise Statistics 2D Image Patterns in the Computer X-ray Diffraction Tomography. *Crystals*, *13*(4), 561.

Cole, C. L., & Crassidis, J. L. (2006). Fast Star-Pattern Recognition Using Planar Triangles. *Journal of Guidance, Control, and Dynamics*, *29*(1), 64–71.

Dai, S., Su, Y., Xiao, Y., Feng, J. Q., & Xing, S. G. (2014). Lunar regolith structure model and echo simulation for Lunar Penetrating Radar. *Proceedings of the 15th International Conference on Ground Penetrating Radar*, 1042–1045.

Danielsson, P.-E. (1980). Euclidean distance mapping. *Computer Graphics and Image Processing*, *14*(3), 227–248.

Erkan, U., & Kilicman, A. (2016). Two new methods for removing salt-and-pepper noise from digital images. *ScienceAsia*, *42*(1), 28.

Fan, Y., Xiao, H., Cao, W., Zuo, L., & Chen, S. (2019). FPGA Implementation of Real-time Star Centroid Extraction Algorithm. *2019 IEEE 2nd International Conference on Information Communication and Signal Processing (ICICSP)*, 395–399.

Feng, J., Wen, L., Li, Y.-D., He, C.-F., & Guo, Q. (2019). Study the performance of star sensor influenced by space radiation damage of image sensor. *2019 3rd International Conference on Radiation Effects of Electronic Devices (ICREED)*, 1–4.

Fossum, E. R., & Hondongwa, D. B. (2014). A Review of the Pinned Photodiode for CCD and CMOS Image Sensors. *IEEE Journal of the Electron Devices Society*, *2*(3), 33–43.

Frazor, R. A., & Geisler, W. S. (2006). Local luminance and contrast in natural images. *Vision Research*, *46*(10), 1585–1598.

Ghazdali, A., Hadri, A., Laghrib, A., & Nachaoui, M. (2024). Poisson noise and Gaussian noise separation through copula theory. *Multimedia Tools and Applications*, *83*(26), 67927–67952.

Hailong, Z., Liang, B., Zhang, T., & Junpeng, H. (2015). Designing considerations for airborne star tracker during daytime. *The 27th Chinese Control and Decision Conference (2015 CCDC)*, 4279–4283.

Hari Balakrishnan, Christopher Terman, & George Verghese. (2010). Lecture 4: Noise. In *Introduction to EECS II: Digital Communication Systems*. MIT OpenCourseWare.

Heiken, G. H., Vaniman, D. T., & French, B. M. (1991). *Lunar Sourcebook*. Cambridge University Press.

Holst, G. C., & Lomheim, T. S. (2011). *CMOS/CCD Sensors and Camera Systems, Second Edition*. SPIE.

Horányi, M., Szalay, J. R., & Wang, X. (2024). The lunar dust environment: concerns for Moon-based astronomy. *Philosophical Transactions of the Royal Society A: Mathematical, Physical and Engineering Sciences*, *382*(2271).

House, D., & C. Keyser, J. (2020). *Foundations of Physically Based Modeling and Animation* (1st ed.). A K Peters/CRC Press.

Hung, M.-H., Pan, J.-S., & Hsieh, C.-H. (2014). A fast algorithm of temporal median filter for background subtraction. *Journal of Information Hiding and Multimedia Signal Processing*, *5*, 33–40.

İnaltekin, B. B., Yağlioğlu, B., & Ceylan, M. (2023). The First Turkish Lunar Mission Part 2: Overview of Space Segment. *2023 10th International Conference on Recent Advances in Air and Space Technologies (RAST)*, 1–5.

Intajag, S., & Sukkasem, N. (2009). Speckle Filtering by Generalized Gamma Distribution. *2009 Fifth International Joint Conference on INC, IMS and IDC*, 1335–1338.

Janesick, J. R. (2001). *Scientific Charge-Coupled Devices*. SPIE.

Jisha J U, & Sureshkumar V. (2014). Poisson Noise Removal in Biomedical Images using Non-Linear Techniques. *International Journal of Advanced Research in Electrical.*

Karaparambil, V. C., Manjarekar, N. S., & Singru, P. M. (2023). Sieve Search Centroiding Algorithm for Star Sensors. *Sensors*, *23*(6).

Khademi, W., Rao, S., Minnerath, C., Hagen, G., & Ventura, J. (2020). Self-Supervised Poisson-Gaussian Denoising. *Cornell University*.

Khalifa, O. O. (2021). *Digital Image Processing and Computer Vision : Fundamentals and Applications*. IIUM Press.

Kumar, L. A., & Jebarani, M. R. E. (2019). A Comprehensive Review on Speckle Denoising Techniques in Satellite I|mages. *2019 International Conference on Communication and Signal Processing (ICCSP)*, 0245–0248.

Li, C., Zuo, W., Wen, W., Zeng, X., Gao, X., Liu, Y., Fu, Q., Zhang, Z., Su, Y., Ren, X., Wang, F., Liu, J., Yan, W., Tan, X., Liu, D., Liu, B., Zhang, H., & Ouyang, Z. (2021). Overview of the Chang'e-4 Mission: Opening the Frontier of Scientific Exploration of the Lunar Far Side. *Space Science Reviews*, *217*(2), 35.

Li, R., Chen, J., Zhang, J., Chen, D., Zhao, X., Mo, P.-Q., & Zhou, G. (2023). Cone penetration resistance of CUMT-1 lunar regolith simulant under magnetic-similitude lunar gravity condition. *Acta Geotechnica*, *18*(12), 6725–6744.

Li, Y., Li, Z., Wei, K., Xiong, W., Yu, J., & Qi, B. (2019). Noise Estimation for Image Sensor Based on Local Entropy and Median Absolute Deviation. *Sensors*, *19*(2), 339.

Li, Y., Wei, X., Li, J., & Wang, G. (2022). Error Correction of Rolling Shutter Effect for Star Sensor Based on Angular Distance Invariance Using Single Frame Star Image. *IEEE Transactions on Instrumentation and Measurement*, *71*, 1–13.

Liang, H., Jia, H., Xing, Z., Ma, J., & Peng, X. (2019a). Modified grasshopper algorithm-based multilevel thresholding for color image segmentation. *IEEE Access*, *7*, 11258–11295.

Liaudat, T. I., Starck, J.-L., & Kilbinger, M. (2023). Point spread function modelling for astronomical telescopes: a review focused on weak gravitational lensing studies. *Frontiers in Astronomy and Space Sciences*, *10*.

Liebe, C. C. (1993). Pattern recognition of star constellations for spacecraft applications. *IEEE Aerospace and Electronic Systems Magazine*, *8*(1), 31–39.

Liebe, C. C. (2002). Accuracy performance of star trackers - a tutorial. *IEEE Transactions on Aerospace and Electronic Systems*, *38*(2), 587–599.

Liebe, C. C., & Joergensen, J. L. (1996). *Algorithms onboard the Oersted microsatellite stellar compass* (E. K. Casani & M. A. Vander Does, Eds.; pp. 239–251).

Lin, B., Wu, P., Wang, H., Xu, X., Yang, X., & Zhang, X. (2024). A Centroiding Method for Targets in Star Images Based on Local PSF Estimation and Iterative Deconvolution. *IEEE Transactions on Instrumentation and Measurement*, *73*, 1–13.

Lin, H., Yang, Y., Lin, Y., Liu, Y., Wei, Y., Li, S., Hu, S., Yang, W., Wan, W., Xu, R., He, Z., Liu, X., Xing, Y., Yu, C., & Zou, Y. (2020a). Photometric properties of lunar regolith revealed by the Yutu-2 rover. *Astronomy & Astrophysics*, *638*, A35.

Lin, H., Yang, Y., Lin, Y., Liu, Y., Wei, Y., Li, S., Hu, S., Yang, W., Wan, W., Xu, R., He, Z., Liu, X., Xing, Y., Yu, C., & Zou, Y. (2020b). Photometric properties of lunar regolith revealed by the Yutu-2 rover. *Astronomy & Astrophysics*, *638*, A35.

Liu, M., Wei, X., Wen, D., & Wang, H. (2021). Star Identification Based on Multilayer Voting Algorithm for Star Sensors. *Sensors*, *21*(9), 3084.

Ma, Y., Jiang, J., Wang, G., Li, J., & Wang, Z. (2024). Dynamic Star Positioning Accuracy Improving Method Using Coded Exposure for Star Sensor. *IEEE Transactions on Instrumentation and Measurement*, *73*, 1–12.

Mahi, Z., & Karoui, M. S. (2019). A Comparative Study of Star Detection Methods for a Satellite-Onboard Star Tracker. *2019 International Conference on Advanced Electrical Engineering (ICAEE)*, 1–6.

Mahi, Z., Karoui, M. S., & Keche, M. (2022). A new star detection algorithm based on the combination of thresholding and filtering technique. *2022 7th International Conference on Image and Signal Processing and Their Applications (ISPA)*, 1–6.

Mahi, Z., Karoui, M. S., & Keche, M. (2024). A Non-Stellar Big Bright Object Elimination and Star Centroid Extraction Algorithm for Star Tracker. *2024 IEEE Mediterranean and Middle-East Geoscience and Remote Sensing Symposium (M2GARSS)*, 1–5.

Marshal, R. M., Rüsch, O., Wöhler, C., Wohlfarth, K., & Velichko, S. (2023). Photometry of LROC NAC resolved rock-rich regions on the Moon. *Icarus*, *394*, 115419.

Moo K. Chung. (2007). The Gaussian Kernel. In *Medical Image Analysis*. University of Wisconsin-Madison.

Mortari, D., Samaan, M. A., Bruccoleri, C., & Junkins, J. L. (2004). The Pyramid Star Identification Technique. *Navigation*, *51*(3), 171–183.

Nabi, A., Ahmed-Foitih, Z., & Cheriet, M. E.-A. (2021). Improved triangular-based star pattern recognition algorithm for low-cost star trackers. *Journal of King Saud University - Computer and Information Sciences*, *33*(3), 258–267.

NASA. (n.d.-a). *Chapter 2: Reference Systems*. Retrieved November 20, 2025, from https://science.nasa.gov/learn/basics-of-space-flight/chapter2-2/

NASA. (n.d.-b). *The Apollo Lunar Surface Journal and Apollo Flight Journal*. Retrieved November 23, 2025, from https://www.nasa.gov/history/alsj-and-afj/

NASA. (2022). Artemis Reference Guide. In *National Aeronautics and Space Administration*.

NASA. (2025, August 8). *Moon Composition & Structure*. https://science.nasa.gov/moon/composition/

Othman Omran Khalifa. (2021). *Digital Image Processing and Computer Vision Fundamentals and Applications*. IIUM Press.

Paige, D. A., Foote, M. C., Greenhagen, B. T., Schofield, J. T., Calcutt, S., Vasavada, A. R., Preston, D. J., Taylor, F. W., Allen, C. C., Snook, K. J., Jakosky, B. M., Murray, B. C., Soderblom, L. A., Jau, B., Loring, S., Bulharowski, J., Bowles, N. E., Thomas, I. R., Sullivan, M. T., … McCleese, D. J. (2010). The Lunar Reconnaissance Orbiter Diviner Lunar Radiometer Experiment. *Space Science Reviews*, *150*(1–4), 125–160.

Painam, R. K., & Suchetha, M. (2022). Comparative Performance Analysis of Spatial Domain Filters for Removing Speckle Noise in SAR images. *2022 First International Conference on Electrical, Electronics, Information and Communication Technologies (ICEEICT)*, 01–05.

Pan, H., Chen, B., Hong, Z., Zhou, R., Zhang, Y., Han, Y., & Tao, J. (2025). Noise Removal from Images of Lunar Areas in Permanent Shadow Using a Combination of Physical Noise Models and Deep Learning. *IEEE Journal of Selected Topics in Applied Earth Observations and Remote Sensing*, *18*, 10307–10319.

Parhad, S. V., Warhade, K. K., & Shitole, S. S. (2023). Speckle noise reduction in sar images using improved filtering and supervised classification. *Multimedia Tools and Applications*, *83*(18), 54615–54636.

Patrice. (2016). Patrice's Lectures: COMPSCI 373 Image Filtering [Course Presentation]. In *The University of Auckland*. https://www.cs.auckland.ac.nz/courss/compsci373s1c/PatricesLectures/

Paul Money. (2018, December 13). *A Guide to Celestial Coordinates*. BBC Sky at Night Magazine. https://www.skyatnightmagazine.com/advice/skills/a-guide-to-celestial-coordinates

Prabhishek Singh, & Raj Shree. (2016). Speckle Noise: Modelling and Implementation. *International Science Press*, *9*(17), 8717–8727.

Qian, X., Yu, H., & Chen, S. (2016). A Global-Shutter Centroiding Measurement CMOS Image Sensor With Star Region SNR Improvement for Star Trackers. *IEEE Transactions on Circuits and Systems for Video Technology*, *26*(8), 1555–1562.

R. C. Gonzalez, & R. E. Woods. (2018). *Digital Image Processing, 4th ed.* (4th ed.). Pearson.

Rafael Alanis. (2010). *Diviner Global Composition*. NASA Science. https://science.nasa.gov/photojournal/diviner-global-composition/

Raman, R., Kumar, V., Pillai, B. G., Rabadiya, D., Patre, S., & Meenakshi, R. (2024). Brain Image Denoising and Segmentation Using Advanced Mixed Thresholding and Edge Preservation Analysis Technique. *2024 International Conference on Knowledge Engineering and Communication Systems (ICKECS)*, 1–5.

Rayman, M. D., Fraschetti, T. C., Raymond, C. A., & Russell, C. T. (2006). Dawn: A mission in development for exploration of main belt asteroids Vesta and Ceres. *Acta Astronautica*, *58*(11), 605–616.

Rennilson, J. J., & Criswell, D. R. (1974). Surveyor observations of lunar horizon-glow. *The Moon*, *10*(2), 121–142.

Rodrigues, I., Sanches, J., & Bioucas-Dias, J. (2008). Denoising of medical images corrupted by Poisson noise. *2008 15th IEEE International Conference on Image Processing*, 1756–1759.

S, S., R, M., D, M., & A, M. (2024). Performance Evaluation of Blob Detection Techniques Using Image Processing. *2024 4th International Conference on Sustainable Expert Systems (ICSES)*, 1101–1106.

Samaan, M. A. (2003). *Toward Faster and More Accurate Star Sensors using Recursive Centroiding and Star Identification*. Texas A&M University.

SATNow. (2023). *Top Satellite Star Trackers in 2023*. https://www.satnow.com/news/details/1457-top-satellite-star-trackers-in-2023

The Hipparcos and Tycho Catalogues. (2008). In *Astronomical Applications of Astrometry* (pp. 1–53). Cambridge University Press.

Trageser, M. B., & Hoag, D. G. (1965). Apollo Spacecraft Guidance System. *IFAC Proceedings Volumes*, *2*(1), 435–463.

Velichko, S., Korokhin, V., Shkuratov, Y., Kaydash, V., Surkov, Y., & Videen, G. (2022). Photometric analysis of the Luna spacecraft landing sites. *Planetary and Space Science*, *216*, 105475.

Wan, X., Wang, G., Wei, X., Li, J., & Zhang, G. (2018). Star Centroiding Based on Fast Gaussian Fitting for Star Sensors. *Sensors*, *18*(9), 2836.

Wang, B., Wang, H., & Jin, Z. (2021). An Efficient and Robust Star Identification Algorithm Based on Neural Networks. *Sensors*, *21*(22), 7686.

Wang, M., Zhang, H., & Zhou, N. (2024). Star Map Recognition and Matching Based on Deep Triangle Model. *Journal of Information, Technology and Policy*, 1–18.

Wang, Q., & Liu, J. (2016). A Chang'e-4 mission concept and vision of future Chinese lunar exploration activities. *Acta Astronautica*, *127*, 678–683.

Wang, R., He, N., Wang, Y., & Lu, K. (2020). Adaptively weighted nonlocal means and TV minimization for speckle reduction in SAR images. *Multimedia Tools and Applications*, *79*(11–12), 7633–7647.

Wang, W., Du, W., Li, Y., & Jia, Z. (2025). Advanced Adaptive Median Filter for Reducing Salt-and-Pepper Noise in GPR Data. *IEEE Geoscience and Remote Sensing Letters*, *22*, 1–5.

Wilhelms, D. E., McCauley, J. F., & Trask, N. J. (1987). *The geologic history of the Moon*.

Wong, U.-H., Wu, Y., Wong, H.-C., Liang, Y., & Tang, Z. (2014). Modeling the Reflectance of the Lunar Regolith by a New Method Combining Monte Carlo Ray Tracing and Hapke's Model with Application to Chang'E-1 IIM Data. *The Scientific World Journal*, *2014*, 1–14.

Wu, F., Xu, Q., Xiang, R., Wu, Q., Wu, X., Zhu, X., Wang, C., & Sun, R. (2023). Anti-noise Star Image Extraction Algorithm for Star Trackers Based on YOLOv5. *2023 Intelligent Methods, Systems, and Applications (IMSA)*, 149–154.

Xiang, J., Xiang, H., & Wang, L. (2023). Poisson noise image restoration method based on variational regularization. *Signal, Image and Video Processing*, *17*(4), 1555–1562.

Xing, F., Dong, Y., You, Z., & Zhou, Q. (2006). APS star tracker and attitude estimation. *2006 1st International Symposium on Systems and Control in Aerospace and Astronautics*, 5 pp. – 38.

Xu, W., Liang, Y., Chen, W., & Wang, F. (2020). Recent advances of stretched Gaussian distribution underlying Hausdorff fractal distance and its applications in fitting stretched Gaussian noise. *Physica A: Statistical Mechanics and Its Applications*, *539*.

Yağlioğlu, B., İnaltekin, B. B., & Gökten, M. (2023). The First Turkish Lunar Mission Part 1: Programmatic, Mission and System Aspects. *2023 10th International Conference on Recent Advances in Air and Space Technologies (RAST)*, 1–6.

Yuan, J., Wu, J., & Kang, G. (2025). High-Precision Centroid Localization Algorithm for Star Sensor Under Strong Straylight Condition. *Remote Sensing*, *17*(7), 1108.

Zhang, Y., Liu, B., Di, K., Liu, S., Yue, Z., Han, S., Wang, J., Wan, W., & Xie, B. (2023). Analysis of Illumination Conditions in the Lunar South Polar Region Using Multi-Temporal High-Resolution Orbital Images. *Remote Sensing*, *15*(24), 5691.

Zou, Y.-L., Liu, J.-Z., Liu, J.-J., & Xu, T. (2004). Reflectance Spectral Characteristics of Lunar Surface Materials. *Chinese Journal of Astronomy and Astrophysics*, *4*(1), 97–104.

APPENDIX A: DATASET 3

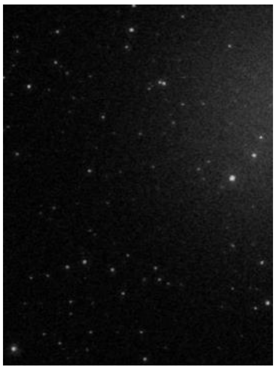
Image 3-1

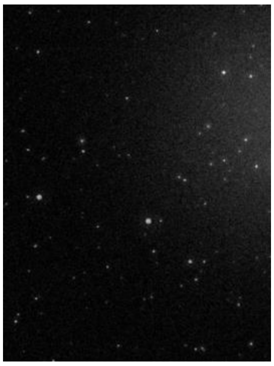
Image 3-2

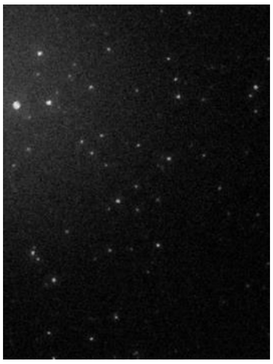
Image 3-3

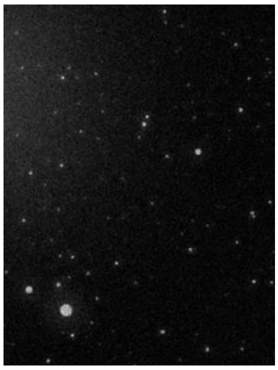
Image 3-4


Image 3-5


Image 3-6


Image 3-7


Image 3-8

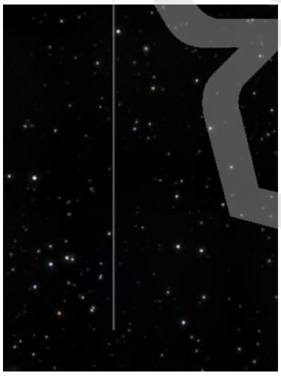
Image 3-9


Image 3-10


Image 3-11


Image 3-12


Image 3-13


Image 3-14


Image 3-15


Image 3-16


Image 3-17


Image 3-18


Image 3-19


Image 3-20


Image 3-21


Image 3-22


Image 3-23


Image 3-24


Image 3-25


Image 3-26


Image 3-27


Image 3-28


Image 3-29


Image 3-30